Hydrodynamic Selection of Particulate Matter Using Pinched-flow Fractionation

by

John F. Ashley

B.A., University of Colorado, 2003

B.S., University of Colorado, 2003

M.S., University of Colorado, 2005

A thesis submitted to the

Faculty of the Graduate School of the

University of Colorado in partial fulfillment

of the requirement for the degree of

Doctor of Philosophy

Department of Chemical Engineering

2012

This thesis entitled:
Hydrodynamic Selection of Particulate Matter using
Pinched-flow Fractionation
written by John F. Ashley
has been approved for the Department of Chemical Engineering

_____

(Robert H. Davis)

_____

(Christopher N. Bowman)

Date_____

Ashley, John F. (Ph.D., Chemical Engineering)

Hydrodynamic Selection of Particulate Matter using Pinched-Flow Fractionation

Thesis directed by Prof. Robert H. Davis and Prof. Christopher N. Bowman

Microfluidic devices have significant potential for use in the separation and isolation of particulates, based on their chemical or physical properties. Implementation of microfluidic devices in the separation of biological components has dramatic potential advantages; however, those advantages are accompanied by equally difficult challenges relating to fabrication, consistency, robustness, and reliability of the device. One technique used to achieve particulate separations employing a microfluidic device based on the size of the particles is pinched-flow fractionation (PFF). PFF provides a simple, efficient methodology for size-based particle separation using fluid mechanics principles.

We developed techniques for constructing microfluidic devices having high-aspect-ratio features, quality and fidelity. In this work, a modified, confocal-microscopy technique was developed to quantitatively determine feature quality. Microfluidic devices and independent, photolithographically-defined features were constructed using thiol-ene resins by means of a soft-lithography technique; contact liquid photolithographic polymerization (CLiPP). Resin cure times and initiator-to-inhibitor ratio were found to have a strong impact on feature quality. A correlation between aspect ratio and feature thickness for thiol-enes was established, as well. Combining the optimization technique with thiol-ene materials led to the formulation of a photopolymerizable resin capable of fabricating high quality, high-aspect-ratio microfluidic channels that were used to fabricate a PFF device.

The final aim of this dissertation was to utilize moving-frame boundary-Integral method (MFBIM) developed in this work to assist in the design of a microfluidic

device with enhanced separation efficiency. Previous studies of PFF devices have shown that channel geometry, flow rate and particle size all affect particle trajectories, and hence, separation efficiency. To study the effects of channel geometry, particle size, and fluid flow on the PFF device's separation performance, a microfluidic channel using the PFF geometry was fabricated. Simulations using the MFBIM were conducted to predict the effects of channel geometry, flow rates, and particle sizes on separation efficiency. The MFBIM simulations provided a method used to predict particle trajectories while varying the flow ratio, particle size and channel geometry. Data from the simulations were used to design a PFF device with optimal separation attributes by modifying the channel geometry and flow ratio.

Dedication

This work is dedicated to my children; Julia, Benjamin and Jacob. They have provided inspiration for my work by always asking the question, 'Why?'.

Acknowledgements

History has shown us that creation of some of the most remarkable inventions arrives after following a twisted and convoluted path. My efforts put forth while performing research seems to have taken such journey. As Ralph Waldo Emerson once remarked, 'Life is a journey, not a destination'. The same can be said of graduate research, in that the journey itself is the purpose.

I would like to thank my co-advisors, Robert Davis and Christopher Bowman. Both have guided and encouraged me to go beyond what I'd hoped or believed I could accomplish. My pursuit of graduate studies and research has been a learning experience for us all. I'm happy that we have concluded this segment of our collaborative efforts and look forward to new challenges.

After completing my undergraduate studies, Professor Bowman provided support and inspiration for me to pursue graduate studies. Chris Bowman helped me to prepare and make presentations and to keep on task. Though my skills in these areas are not stellar, Chris was patient and had a steady hand in helping me to improve.

Professor Davis provided invaluable direction for my project. He had a strong role in guiding and structuring what had been a concept into a comprehensive graduate research project. Rob's high standards have provided an insight into the methods required when conducting research.

My greatest appreciation towards Professor Davis and Bowman lies in their compassion and efforts that have provided me the opportunity to remain a father while performing research. I will forever be indebted to them for their support.

My research mentors, Dr. Neil Cramer and Dr. Christopher Brotherton helped me to navigate through many of the intricacies associated with research and graduate school. Interaction with Neil and Christopher helped to define and direct my research.

My thanks go to Dr. Alexander Zinchenko for his patience and guidance. Dr. Zinchenko's pursuit of novel and unique solutions to challenges in the area of fluids has been inspirational, and I am honored to have had the opportunity to work with and learn from him.

My committee members, Dr. Christine Hrenya, Dr. Kamran Mohseni, Dr. Patrick Weidman and Dr. Alexander Zinchenko have been helpful in providing guidance during the course of my research.

Other graduate students have provided invaluable support and assistance. Dr. Andrew Griggs, Dr. Helen Simms, Dr. Michelle Staben, Dr. Jeffrey Knutsen, Dr. Tommy Haraldsson, and Dr. Bobby Sebra have all provided support and assistance over the years.

Finally, I would like to thank my children, Julia, Benjamin and Jacob. I would have never attempted this work without them. They have provided clarity and direction to my life and work. Their wonderment and fascination with nature, science and mathematics continue to be an inspiration for me.

Contents

Chapter

Figures

Figure

Tables

Table

Chapter 1

Introduction

1.1 Introduction

Lab-on-chip technology provides a powerful methodology that is suitable for miniaturization of a wide range of laboratory and clinically relevant processes.[1] The advent of micro and nano-chip technology reduces the power utilization, chemical reagents, cost, and space requirements while aiding in portability for many critical laboratory-based applications. In particular, implementation of microfluidic devices in the separation of biological components has dramatic potential advantages; however, those advantages are accompanied by equally difficult challenges relating to fabrication, continuous-flow operation, consistency, robustness, and reliability of the device.[2]

Microfluidic devices have significant potential for use in separation and isolation of particulates, based on the chemical or physical properties of the particulate matter. One mechanism of achieving particulate separations on microfluidic devices based on the size of the particles is pinched-flow fractionation (PFF), which provides a simple, efficient methodology for size-based particle separation using fluid mechanics principles.[3] Separation of particles by size is useful in several applications, including isolation of cellular components from cellular matter and in the separation of non-aggregated particles from environmental or medical samples, both of which represent ideal applications for implementation of microfluidic separations.

Incorporation of PFF methods on a microchip provides a facile method for separation of particulate matter. Here, separation of particles using PFF makes use of a microchannel with two inlet channels entering at opposing angles that merge to form a narrow ‘pinch’ region that is larger than but on the order of the particle diameter, which is followed by an expansion area. Of

the two inlet streams, one carries a mixture of neutrally-buoyant particles immersed in a fluid, with the second containing only fluid. The second inlet channel, containing only fluid, generally has a significantly higher volumetric flow rate, which ultimately forces the particles from the first inlet channel to move close to the top wall of the microchannel pinch area. If the particles are forced to approach the top wall in a manner that depends on their size, with smaller particles being closer to the top wall, then as the particles exit the pinch area and enter the expansion area, they follow different, size-dependent trajectories, as shown in Figure 1. In particular, the large particles exit with lower trajectories because size exclusion keeps the particle centers a minimum of one radius away from the upper wall of the pinch area.

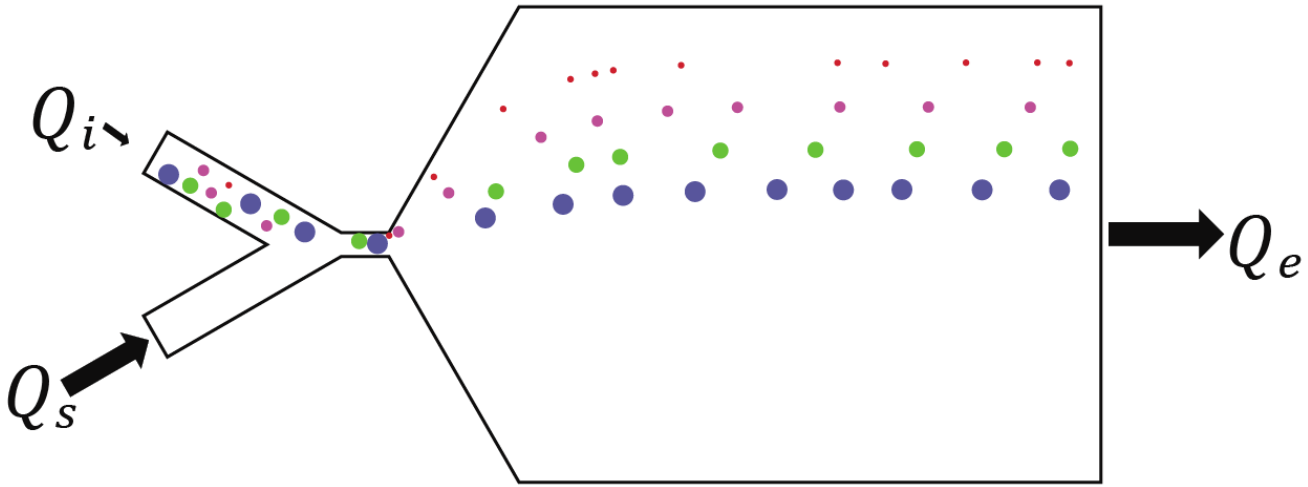

Figure 1.1 Pinched-flow fractionation device showing inlet channels, pinch, exit area and particles of different sizes during operation. Inlet flow rates (Q_i , Q_s) and exit flow rate ($Q_e = Q_i + Q_s$) are shown with relative flow rates represented by arrow size.

Despite the vast potential of PFF, there has been little in the way of theoretical analysis or design of these devices. Thus, the goal of this dissertation is a predictive understanding of the effects that channel geometry, particle size and distribution, and fluid-flow characteristics have on the function of the PFF device performance, so that a device with the desired separation characteristics can be well-designed and easily implemented. Experimentally, to fabricate a device with the qualities necessary for efficient operation, properties such as high-aspect-ratio channels, facile fabrication methods, and control of physical characteristics of the channel walls are needed. Development of the materials and methods necessary for building a PFF with features necessary for efficient operation is also examined in this work, as is a comparison between experimental results and the theoretical predictions.

1.2 Prior State of Knowledge

1.2.1 Device Materials and Fabrication

Microfluidic devices fabricated using polymeric materials are particularly advantageous for applications such as micro-scale mixing, environmental detection, and chemical and biological analyses. The effectiveness of micro-electro mechanical systems (MEMS) and microfluidic devices depends, in part, upon the device application and specific requirements related to the surface chemical and mechanical characteristics. Presently, many soft lithography and rigid photomasking methods utilize poly(dimethylsiloxane) (PDMS) to fabricate microfluidic devices.[4] PDMS is a rubbery, loosely crosslinked permeable polymer prone to significant mass transfer and uptake when exposed to certain gases.[5] Though advantageous for many applications, the mechanical, chemical and physical surface properties such as surface hardness, solvent resistance and high gas permeability that are exhibited by PDMS present a challenge to fabricating microfluidic devices, particularly for PFF applications.[6]

Recently, acrylic monomers have been used to create polymeric microfluidic devices using photolithographic techniques. The use of acrylic monomers in the fabrication of microfluidic channels affords significant advantages with respect to the wide variability in material properties that can be achieved; however, it presents challenges in the design of microfluidic devices where requirements of high aspect ratios of features, solvent resistance, and low shrinkage exist.

For silicon-based microfluidic devices using traditional lithographic patterning techniques, mask-based fabrication of features smaller than 30 μm requires lithographic masks that are time consuming and costly to prepare.[7] Turnaround time and costs are reduced using soft lithography production methods, and soft lithographic fabrication techniques using polymeric materials offer flexibility in achieving the desired mechanical and chemical performance.

One particularly promising soft-lithographic technique is contact liquid photolithographic polymerization (CLiPP) technology,[8] where the mask is used in direct contact with a photopolymerizable resin that facilitates the formation of multilayer devices. For features >30 μm in size, inexpensive masks that can be produced rapidly facilitate the production of these microfluidic devices.

1.2.2 Simulation Methods

Particle transport at low Reynolds numbers occurs in a variety of engineering, industrial and biological applications, and the importance of such applications has motivated an extensive body of both theoretical and experimental research. In particular, flow-driven particle transport in channels has many applications and consequently has been studied using a variety of techniques. The study of particle transport in complex channels has advanced incrementally through the evaluation and analysis of idealized, relatively simple configurations. Initially, studies of particle interaction near a single wall were followed by investigation of particle transport in

channels. Two channel configurations commonly used to simulate particle transport in straight channels include a cylindrical tube and a slit between two infinite, parallel walls.

Analysis of the transport of a single sphere in an unbounded fluid environment provides a simple model of the desired behavior, which was subsequently followed by modeling particle motion near a single wall. Lorentz[9] provided one of the initial studies of particle movement near a single wall using bispherical coordinates, while Dean and O'Neill[10-12] followed with a study of the rotational velocity of a sphere near a single wall at low Reynolds numbers.

The method of reflections, used by Ho and Leal,[13] and described by Happel and Brenner,[14] has been used to determine forces on a sphere transported between two straight walls in Poiseuille and Couette flows. However, such an approach is limited to smaller particles (relative to channel width) far away from channel walls. For the case where the particle size is large (relative to channel width), and the fit of such particles is, therefore, tight, the method of reflections becomes numerically restrictive. The collocation method, through use of Green's functions introduced by Ganatos *et al*.[15-17] to study particle motion perpendicular and parallel to walls, provides a method for calculating the force and torque upon the sphere in motion. Work by Staben[18-20] extended this approach to yield a viable alternative using boundary-integral method for calculating particle transport between two infinite, parallel plates. Recent studies using mixed Cartesian-multipole representation were able to include effects of particle-particle interactions on this behavior.[21-24]

The problems posed by complex channel geometries[25] of the type studied by Hopf[26] and Ladyzhenskaya were addressed using Green's function. For more complex channel geometries, the free-space Green's function is used, requiring discretization of both the channel walls and particle surface area utilizing a completed-double-layer, boundary-integral method (CDL-BIM)

approach, since the domain Green's functions for complex geometries are not generally known.[27] The free-space Green's function is represented by the velocity field due to a point force in an infinite fluid, without boundaries.

The work by Staben *et al.*[14] has shown that the effects of channel surfaces distant from particles in straight-channel flow are minimal when compared to channel surfaces close to the particle surface. Since there is relatively minimal effect caused by the sidewalls distant from the particle surface, the model formulation is reduced by using a 2D Green's function to represent the channel environment enclosing a 3D particle.

Recently, studies with channels having sharp corners, curvature and single or multiple bifurcations have addressed challenges in simulating particle transport in microfluidic channels with such complex geometries where particle transport through these types of channels is of particular interest in understanding the transport of cellular matter through blood vessels.[28-30] Experimental studies by Roberts and Olbricht[31] demonstrate transport of particles in a variety of bifurcated configurations, while a corresponding model to describe particle motion through such channel configurations was described by Audet and Olbricht[32] by implementing 2D boundary-integral simulations with smoothed corners and cylindrical particles in a plane-parallel geometry.

The channel geometry used in a PFF device consists of a bifurcation inlet channel and has a number of sharp corners in the device. Channel geometry, particle size, fluid transport and the volumetric flow rate ratio of input-channel fluids all are known to affect the particle trajectories through the device. Andersen *et al.*[33] recently developed a model based on the laminar velocity profile in a rectangular channel[34] assuming that particles leave the top corner of the pinch and follow the fluid flow into different exit or drain channels depending on particle size, without consideration of particle-wall or particle-corner hydrodynamic interactions. Systematic studies

of the hydrodynamic, particle-wall and particle-corner interactions that produce the PFF effects have only recently been developed as part of this dissertation study, using a moving-frame, boundary-integral method (MFBIM) to describe the particle trajectories.[35]

1.2.3 PFF Experiments

The effectiveness of PFF in the separation of particles has been demonstrated experimentally by Nakashima *et al.*[3] Applications utilizing PFF include filtration,[36] droplet separation,[37] and flow cytometry,[38] and the method has been used for detection of single nucleotide polymorphisms and provides a method for simulating the trajectory of particles through the channel.[39] The effects of channel geometry on particle separation efficiency have been studied based on experimental data.[40] Studies have attributed variance in particle separation to imperfections in channel fabrication and inaccuracies in optical measurements.[41]

1.3 Motivation

The motivation for this work lies in the need to produce application-specific, customizable high-fidelity microfluidic devices in a cost-efficient and timely manner. Specifically, we wish to use a systematic approach in the design and testing of a PFF device that would separate particles by size using hydrodynamic focusing.

The applications of PFF technology include uses in various areas of research such as in biological, industrial, and medical procedures. Interestingly, the technology can be adapted for a wide distribution of particle sizes and is scalable for micro- and nano-scale applications. Limitations of existing particle separation technology include portability, required sample volume, separation sensitivity and the necessity of batch operation.

To construct these high-performance devices, novel approaches are needed to address the physical and chemical behavior of the materials used in the PFF device fabrication. Since

materials and methods currently used in the fabrication of application-specific microfluidic devices often do not provide adequate solutions, alternative approaches should be studied and tested. Polymeric materials and soft lithography offer flexibility and control in the design and selection of material and surface properties.

To design a microfluidic device, each component of the overall operation must be understood so that its function may be improved and optimized, and computer simulation is one tool that has proven useful in the design and testing of fluid and particle behavior in microfluidic systems. Accurate computational modeling that accurately describes the near-wall particle transport in complex microchannels is an area where much study is needed, As previous work has assumed that particles follow fluid streamlines in the exit, starting at one radius from the wall, without considering particle- to wall hydrodynamic interactions or even the conditions required for the particles to reach the wall within the pinch region. Computer modeling based on accurate mathematical models provides predictive information about function and aids in the optimization of lab-on-a-chip design in a timely, economical fashion.

The capacity to integrate multiple technology platforms systematically is challenging and motivates us to explore new and novel methodologies. The systematic methods we use to study and analyze systems are as important as the solutions they provide. The constant change and variability of application-specific solutions prompts us to constantly re-evaluate our approach to addressing design challenges in PFF device fabrication and performance.

1.4 Fabrication of Microfluidic Channels

In this work, a PFF microchannel device is fabricated using the channel geometry predicted to have appropriate separation characteristics as modeled by MFBIM simulations.[35] Application-specific features unique to the PFF microchannel include that geometric device features must

have high-fidelity and high-aspect ratios. The feature fidelity as well as various aspects of the feature shape and quality were assessed as functions of various resin attributes, particularly the polymerization mechanism and also including exposure conditions, the initiator concentration and the inhibitor-to-initiator ratio. An optical technique using confocal microscopy was utilized to evaluate the feature fidelity as well as feature shape and quality. These results were used to create a thiol-ene resin formulation able to produce high-fidelity, high-aspect-ratio features without significant reductions in feature quality. Fabrication of the PFF device was accomplished using the previously developed soft-lithography method known as contact liquid photolithographic polymerization (CLiPP), though it was coupled here with the unique thiol-ene click reaction mechanism.[42]

The CLiPP method was modified to fabricate the PFF device. Since only a single layer of resin was needed for the device, a single-step method was introduced to facilitate the fabrication process. The thiol-ene-based resin was placed between a mask bound to a cover slide and a glass substrate, followed by exposure to 365 nm UV radiation as shown in Figure 2.

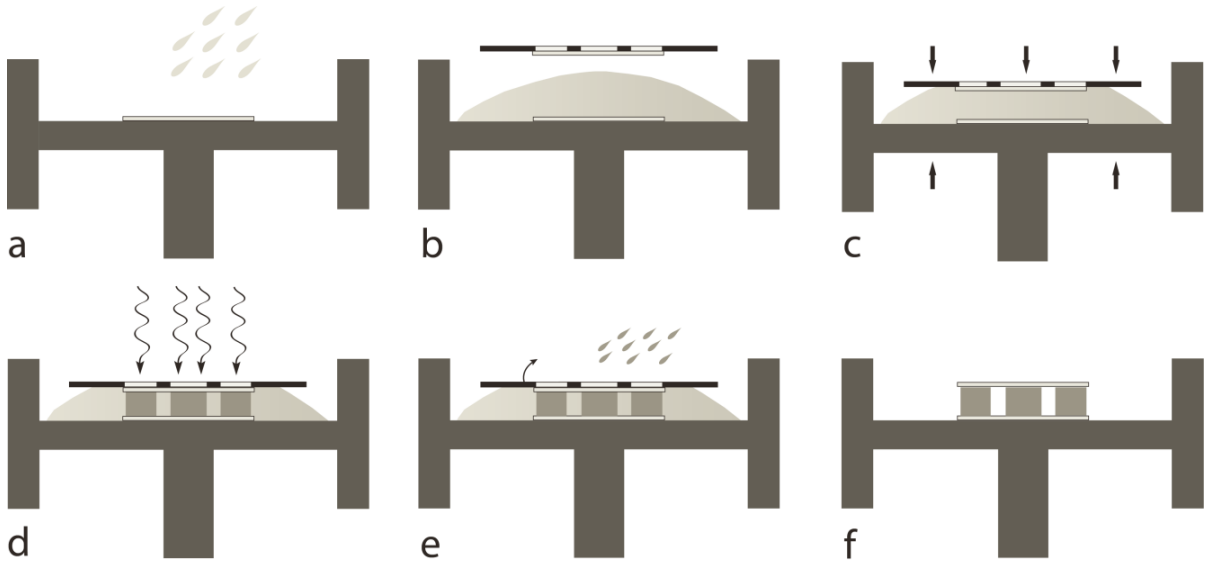

Figure 1.2 Schematic of the CLiPP process. Step a: The siloxane-treated glass slide is secured to the chamber base and a monomer mixture fills the chamber. Step b: After filling the chamber with monomer, an aligned mask (top) is joined with a siloxane-treated glass slide and placed over the monomer. Step c: The siloxane-treated glass slide is brought in contact with the monomer and lowered to the desired feature height. Step d: The monomer mixture is exposed to collimated 365 nm UV radiation through the aligned mask. Step e: The mask is removed from the glass slide. Step f: Excess, uncured monomer is removed by washing with solvent. After washing, only the substrate, top glass slide and PFF device remain.

1.5 Simulation of Particle Trajectories in Complex Channels

Separation of particles using PFF makes use of a microchannel, where modifications to channel geometry, inlet flow rate, particle shape, channel width, and feature aspect ratio have a notable effect on separation characteristics. To date, empirical observation provides general relationships relating inlet flow rate and channel geometry to particle trajectories, but no systematic modeling using computational fluid dynamics exists. Development of an accurate, predictive numerical approach would aid in the design of the device and process optimization necessary to achieve the desired particle separation.

The MFBIM as described by Zinchenko *et al*. [35] is used in this work to study the effects of various device and particle attributes on size segregation. First, a 2D model of the fluid transport through the channel with no particles was determined using BIM. For the fluid-only domain, no-slip conditions at the channel wall, with Poiseuille flow for channel inlet(s) and outlet, were assumed.

A discretized sphere was then placed within the fluid-only, 2D flow field. Around the sphere, a computational cell was constructed, several times the radius of the sphere. Construction of the computational cell provides a computationally manageable domain where the instantaneous locations as well as the translational and rotational velocities of the sphere were all calculated. The trajectory of each sphere was determined by sequential calculation of the forces at the sphere's surface and its velocity using a series of computational cells.

1.6 Experiments

A PFF device was fabricated with channel geometries that were predicted to provide the desired separation characteristics, based on the simulations. Two polystyrene sphere sizes of small and intermediate size (relative to pinch width) were selected for the experiments to track

particle movement. A fluid of equal density to the polystyrene particles was used to maintain neutral-buoyancy, and syringe-drive pump systems were used to control the volumetric flow rates of the fluid-only and particle-fluid mixtures.

Flow rate ratios above and below the 'critical' values as determined by simulations were used and regulated by a pump-control device. Here, the critical flow-rate ratio represents the flow-rate ratio (of the two inlet streams) above which ideal, complete separation of the two particle sizes is predicted to occur. Digital images of the polystyrene particles being transported through the channel were captured and analyzed to establish the experimental particle trajectories. The particle trajectories at fixed flow-rate ratios were compared to simulation results. At subcritical flow ratios, lateral exit positions are dependent upon lateral entry positions, resulting in a range of lateral exit positions for same-sized particles, Hence, for sub-critical flow rate ratios, the impact of the lateral entry positions on the lateral exit positions was compared to simulation results for both particle sizes.

1.7 Dissertation Overview

The results of this work addresses several important requirements related to the design, fabrication and function of microfluidic devices. Numerical simulation and computer-aided design are resources for the optimization of lab-on-a-chip design in a timely, economical fashion. Construction of microchips utilizing microfluidics requires significant capital expenditure for fabrication and design for testing. Valid predictive capabilities are needed to aid in the development of an optimal experimental design while reducing time and material expenditures required for such testing.

Many microfluidic devices are fabricated using photolithographic fabrication techniques. However, traditional resin systems exhibit limited aspect ratios and partial channel fill that limit

device applications. Feature quality is critical for the design of many features present in microfluidic devices, but the ability to quantify feature quality systematically for the purposes of optimizing resin composition is lacking, and new approaches are needed.

In Chapter 2, the application-specific needs of microfluidic devices and methods of fabrication are discussed. Since fabrication of microfluidic devices shares a number of application-specific shortcomings, we explored the use of novel resins, polymerization mechanisms and methods to fabricate a microfluidic device. A thiol-ene-based photopolymerizable resin that exhibited desirable characteristics, such as low cure time and the ability to overcome oxygen inhibition, was used to fabricate the microfluidic device. A novel optical technique was used to evaluate feature fidelity, shape and quality, and this ability to quantify feature attributes provided results used to create a greatly improved thiol-ene resin formulation and curing process. The optimized resin formulation and photopolymerization process were used to fabricate a microfluidic PFF device, and the results are described by (Ashley *et al.*, 2011).[43]

The use of the MFBIM to predict the transport of particles in complex microchannels is described in Chapter 3, where a 3D algorithm is developed that simulates flow-driven motion of neutrally-buoyant particles through complex microchannels at low Reynolds number. The MFBIM is used to accurately predict fluid flow and particle motion in several geometric configurations. The 3D algorithm is compared to numerical solutions proposed in the existing literature for other problems, with favorable results. Having validated the model by thorough comparisons with existing numerical solutions and experimental results, the algorithm was used to predict particle movement through a microfluidic device with complex channels. A PFF device is examined as one test model, and a T-junction is examined as a second test model. This

work has been published by Zinchenko, Ashley and Davis (2011), and simple modifications to channel geometry, flow ratio, and particle size and their effects on particle trajectory are presented.[35]

Chapter 4 uses the MFBIM to simulate the trajectories of spheres through a PFF device. Various changes to channel geometry, flow ratio, and particle sizes are made to understand further their effects on particle separation and PFF performance. Using data provided from simulations, we proposed a PFF device geometry that would provide the greatest particle separation at the lowest flow rate ratio. Experiments are also presented in the chapter using the optimized geometry design that is suggested by the MFBIM simulations. Here, a PFF device was fabricated using the methods presented in Chapter 2, and experiments were performed that track the movement and trajectories of polystyrene spheres through the device. Results of experiments were then compared to simulations presented earlier in the chapter. This work has been submitted by Ashley *et al.* (2012).[44] Conclusions, possible areas of future research, and suggestions for improvement in the present work are made in Chapter 5.

1.8 References

[1] T. Chován and A. Guttman, Microfabricated devices in biotechnology and biochemical processing, *Trends in Biotechnology* **20**,116-122 (2002).

[2] A. Guber, M. Heckele, D. Herrmann, A. Muslija, V. Saile, L. Eichhorn, T. Gietzelt, W. Hoffmann, P. Hauser, J. Tanyanyiwa, Microfluidic lab-on-a-chip systems based on polymers—fabrication and application, *J. Chem. Eng*. **101**, 447-453 (2004).

[3] M. Nakashima, M. Yamada, and M. Seki, Pinched flow fractionation (PFF) for continuous particle separation in microfluidic device, *17th IEEE International Conference on Micro-Electro Mechanical Systems* 33-36 (2004).

[4] Y. Xi, G. Whitesides, Soft lithography, *Ann. Rev. Mater. Sci.* **28,** 153 (1998).

[5] D. Duffy, J. McDonald, J. Schueller, G. Whitesides, Rapid prototyping of microfluidic systems in poly(dimethylsiloxane), *Anal Chem.***70,** 4974-4984 (1998).

[6] G. Whitesides and A. Stroock, Flexible methods for microfluidics, *Physics Today* **54**, 42-48 (2001).

[7] G. Whitesides, M. Martyn, P. Coates, Micromoulding: process characteristics and product properties, *Plastics, Rubber and Composites* **32**, 231–239 (2003).

[8] K. Haraldsson, J. Hutchison, K. Anseth, C. Bowman, 3D Polymeric microfluidic device fabrication via contact liquid photolithographic polymerization (CLiPP), *Sens. Actuators B, Chemical* **113**, 454-460 (2006).

[9] H. Lorentz, A general theorem concerning the motion of a viscous fluid and a few consequences derived from it, *Zittingsverslag* Koninkl. Akad. van Wetensch. Amsterdam **5**, 168-175 (1896).

[10] W. Dean and M. O'Neill, A slow motion of viscous liquid caused by the rotation of a solid sphere, *Mathematika* **10**, 13-24 (1963).

[11] M. O'Neill, A slow motion of viscous liquid caused by a slowly moving solid sphere, *Mathematika* **11**, 67-74 (1964).

[12] M. E. O'Neill, A slow motion of viscous liquid caused by a slowly moving solid sphere: An addendum, *Mathematika* **14**, 170-172 (1967).

[13] B. Ho and L. Leal, Inertial migration of rigid spheres in 2-dimensional unidirectional flows, *J. Fluid Mech.* **65,** 365-400 (1974).

[14] J. Happel and H. Brenner, *Low Reynolds Number Hydrodynamics*, 5th ed. Martinus Nijhoff, Dordrecht (1986).

[15] P. Ganatos, R. Pfeffer and S. Weinbaum, A strong interaction theory for the creeping motion of a sphere between plane parallel boundaries, 2. Parallel motion, *J. Fluid Mech.* **99**, 755-783 (1980).

[16] P. Ganatos, S. Weinbaum and R. Pfeffer, A strong interaction theory for the creeping motion of a sphere between plane parallel boundaries. 1. Perpendicular motion, *J. Fluid Mech.* **99**, 739-753 (1980).

[17] P. Ganatos, S. Weinbaum and R. Pfeffer, Gravitational and zero-drag motion of a sphere of arbitrary size in an inclined channel at low reynolds-number, *J. Fluid Mech.* **124**, 27-43 (1982).

[18] M. Staben, A. Zinchenko, and R. Davis, Motion of a particle between two parallel walls in low-Reynolds-number Poiseuille flow, *Phys. Fluids* **15**, 1711-1733 (2003).

[19] M. Staben, A. Zinchenko, and R. Davis, Dynamic simulation of spheroid motion between two parallel plane walls in low-Reynolds-number Poiseuille flow, *J. Fluid Mech.* **553**, 187-226 (2006).

[20] M. Staben, A. Zinchenko, and R. Davis, Erratum: Motion of particle between two parallel plane walls in low-Reynolds-number Poiseuille flow, *Phys. Fluids* **15**, 1711-1733 (2003). *Phys. Fluids* **16**, 4204-4206 (2004).

[21] S. Bhattacharya, J. Blawzdziewicz, and E. Wajnryb, Many-particle hydrodynamic interactions in parallel-wall geometry: Cartesian-representation method, *Physica A* **356**, 294-340 (2005a).

[22] S. Bhattacharya, J. Blawzdziewicz, and E. Wajnryb, Hydrodynamic interactions of spherical particles in suspensions confined between two planar walls, *J. Fluid Mech.* **541**, 263-292 (2005b).

[23] S. Bhattacharya, J. Blawzdziewicz, and E. Wajnryb, Far-field approximation for hydrodynamic interactions in parallel-wall geometry, *J. Comp. Physics* **212**, 718-738 (2006a).

[24] S. Bhattacharya, J. Blawdziewicz, and E. Wajnryb, Hydrodynamic interactions of spherical particles in Poiseuille flow between two parallel walls, *Phys. Fluids* **18**, 053301 (2006b).

[25] O. Ladyzhenskaya, *The Mathematical Theory of Viscous Incompressible Flow*, Revised Second Edition, Gordon and Breach Science Publishers NY, NY, 1969.

[26] E. Hopf, Über die Anfangswertaufgabe für die hydrodynamischen Grundgleichungen, *Mach. Nachrichten* **4**, 213-231 (1950-1951).

[27] S. Kim, S. Karilla, *Microhydrodynamics – Principles and Selected Applications*, Dover, Mineola, New York, (2005).

[28] S. Chien, C. Tvetenstrand, M. Farrel Epstien, and G. Schmid-Schnbien, Model studies on distributions of blood cells at microvascular bifurcations, *Amer. J. Physiol.* **248**, H568-H576 (1985).

[29] R. Ditchfield and W. Olbricht, Effects of particle concentration on partitioning of suspensions at small divergent bifurcations, *J. Biomech. Eng.* **118**, 287-294 (1996).

[30] M. Kelmanson, Modified integral equation solution of viscous flows near sharp corners, *Computers & Fluids* **11**, 307-324 (1983).

[31] B. Roberts and W. Olbricht, "The distribution of freely suspended particles at microfluidic bifurcations," *AIChE J.* **52**, 199-206 (2006).

[32] D.M. Audet and W.L. Olbricht, The motion of model cells at capillary bifurcations, *Microvasd. Res.* **33**, 377-396 (1987).

[33] K. Andersen, S. Levinsen, W. Svendsen, F. Okkels, A generalized theoretical model for continuous particle separation in a microchannel having asymmetrically arranged multiple branches, *Lab Chip* **9**, 1638-1639 (2009).

[34] H. Bruus, *Theoretical Microfluidics*, Oxford University Press, 1st ed., (2007).

[35] A. Zinchenko, J. Ashley,R. Davis, A moving-frame, boundary-integral method for particle transport in microchannels of complex shape, *Phys Fluids* **24**, 043302 (2011).

[36] M. Yamada, M. Seki, Microfluidic particle sorter employing flow splitting and recombining, *Anal. Chem.* **78**, 1357-1362 (2006).

[37] H. Maenaka, M. Yamada, M. Yasuda, and M. Seki, Continuous and size-dependent sorting of emulsion droplets using hydrodynamics in pinched microchannels, *Langmuir* **24**, 4405-4410 (2008).

[38] D. Inglis, J. Davis, T. Zieziulewicz, D. Lawrence, R. Austin, and J. Sturm, Determining blood cell size using microfluidic hydrodynamics, *J. of Immun. Meth.* **329**,151-156 (2008).

[39] A. Larsen, L. Poulsen, H. Birgens, M. Dufva and A. Kristensen, Pinched flow fractionation devices for detection of single nucleotide polymorphisms, *Lab Chip* **5**, 818-821 (2008).

[40] X. Zhang, J. Cooper, P. Monaghan, S. Haswell, Continuous flow separation of particles within an asymmetric microfluidic device, *Lab Chip* **6,** 561–566 (2006).

[41] A. Jain A, J. Posner, Particle dispersion and separation resolution of pinched flow fractionation, *Anal. Chem.* **80**, 1641–1648 (2008).

[42] J. Hutchison, K. Haraldsson, B. Good, R. Sebra, N. Luo, K. Anseth, and C. Bowman, Robust polymer microfluidic device fabrication via contact liquid photolithographic polymerization (CLIPP), *Lab Chip* **4**, 758-662 (2004).

[43] J. Ashley, N. Cramer, R. Davis, and C. Bowman, Soft-lithography fabrication of microfluidic features using thiol-ene formulations, *Lab Chip* **11**, 2772-2778 (2011).

[44] J. Ashley, C. Bowman, R. Davis, Hydrodynamic selection of particulate matter using pinched-flow fractionation, *Langmuir* (2012, submitted).

Chapter 2

Soft-lithography fabrication of microfluidic features using thiol-ene formulations

(Ashley, Cramer, Davis and Bowman (2011), *Lab Chip* **11**, 2772-2778)

In this work, a novel thiol-ene based photopolymerizable resin formulation was shown to exhibit highly desirable characteristics, such as low cure time and the ability to overcome oxygen inhibition, for the photolithographic fabrication of microfluidic devices. The feature fidelity, as well as various aspects of the feature shape and quality, were assessed as functions of various resin attributes, particularly the exposure conditions, initiator concentration and inhibitor to initiator ratio. An optical technique was utilized to evaluate the feature fidelity as well as the feature shape and quality. These results were used to optimize the thiol-ene resin formulation to produce high fidelity, high aspect ratio features without significant reductions in feature quality. For structures with aspect ratios below 2, little difference (<3%) in feature quality was observed between thiol-ene and acrylate based formulations. However, at higher aspect ratios, the thiol-ene resin exhibited significantly improved feature quality. At an aspect ratio of 8, raised feature quality for the thiol-ene resin was dramatically better than that achieved by using the acrylate resin. The use of the thiol-ene based resin enabled fabrication of a pinched-flow microfluidic device that has complex channel geometry, small (50 mm) channel dimensions, and high aspect ratio (14) features.

2.1 Introduction

Micro-electro mechanical systems (MEMS) and microfluidic devices enable portability, low energy consumption, and reductions in sample and reagent quantities for a range of laboratory procedures. However, when these micro devices are formed through conventional fabrication

methods, such as micro-machining, injection molding, or embossing, they require significant investment in labor and are limited in the type and characteristics of device features that can be fabricated. For silicon based microfluidic devices using traditional lithography techniques, mask fabrication for features smaller than 8–10 mm requires masks that are costly to prepare. Turnaround time and costs are reduced significantly when soft lithographic production methods are employed. Further, soft lithography using polymeric materials offers flexibility and tunability in the design and selection of material and surface properties. The effectiveness of MEMS and microfluidic devices depends upon the device application and specific requirements related to the surface chemistry and mechanical characteristics.

Presently, many soft lithographic and rigid photomasking methods utilize poly(dimethylsiloxane) (PDMS) to fabricate microfluidic devices.[1] PDMS consists of a siloxane backbone that is frequently coupled to (meth)acrylate functional groups to yield a photopolymerizable material that is both liquid and photopatternable.[2] Traditional organic based (meth)acrylate photo-polymer formulations have also been utilized in the fabrication of microfluidic devices.[3,4] When employing (meth)acrylate based formulations, the wide variety of available monomers with varying functionality, molecular weight, and chemistry enables the design of polymers with properties tailored to specific application requirements. Various (meth)acrylic formulations optimized to suit application-specific features, such as optical coatings, are used for the fabrication of microfluidic devices.[5] For both PDMS and (meth)acrylic formulations, the diversity of design possibilities is also associated with tradeoffs between resin viscosity, mechanical properties, volume shrinkage, and poly-merization-induced shrinkage stress.[6–8] Monomers with lower molecular weight per functional group result in resins with low viscosity and polymer networks with higher crosslink density, which enhances solvent

resistance, but also results in higher polymerization shrinkage and shrinkage stress. High shrinkage and stress results in channels with fracture lines (an aspect of shrinkage strain), constrictions and/or enlargements that diminish device utility. Increasing the molecular weight per functional group reduces polymerization shrinkage and stress, but also increases monomer viscosity, which limits the fabrication of narrow channels.[9,10] Higher molecular weight monomers also typically exhibit reduced crosslinking that leads to increased swelling when in contact with solvents. Additionally, PDMS formulations with low crosslink density are highly permeable to gases, which affect the physical characteristics and functionality of devices that are sensitive to oxygen-such as those designed for use with blood.[2] Hence, photopolymerizable (meth) acrylate based formulations have numerous desirable characteristics, but they are limited in their ability to form devices where it is necessary to have a combination of high aspect ratio features, good solvent resistance, low swelling, low volume shrinkage and high fidelity features.

Here, we investigate the use of a unique polymerization system for fabrication of microfluidic devices. Thiol-ene resins photo-polymerize via a radical-mediated, step-growth mechanism that affords these systems a number of unique polymerization attributes and polymer properties that are not achievable in acrylic systems. These attributes include rapid polymerization kinetics, low shrinkage, limited susceptibility to oxygen inhibition and delayed gelation that further reduces the polymerization-induced shrinkage stress.[6–8,10–12] The thiol-ene polymerization reaction results from the alternating addition of a thiyl radical across a carbon-carbon double bond to generate a carbon-centered radical (Step 1), followed by chain transfer to a thiol functional group that regenerates the thiyl radical (Step 2). These alternating addition and chain transfer reaction steps form the basis for the step-growth mechanism and the unique polymerization behavior.

Addition

$RS\bullet + R'CH{=}CH_2 \rightarrow RSCH_2\text{-}C\bullet HR'$ Step 1

Chain Transfer

$R'C\bullet H\text{-}CH_2SR + RSH \rightarrow R'CH_2\text{-}CH_2SR + RS\bullet$ Step 2

Reduced oxygen inhibition in thiol-ene polymerizations facilitates the use of reduced initiator concentrations, while still achieving rapid polymerization and excellent surface cure. Decreased photoinitiator concentration reduces light attenuation, allowing for the creation of thicker, more uniformly polymerized features. Delayed gelation is also a feature of the step-growth, network-evolution process in thiol-ene reactions and results in resins that remain in the liquid state until relatively high conversion is attained. This behavior results in reduced stress in the polymer and a more distinct boundary between gelled and non-gelled polymer regions. This combination of advantages facilitates the fabrication of features with higher fidelity and at higher aspect ratios (>3) as compared to those achievable by using acrylate resins.

In addition to fabricating microfluidic devices and channel features, this work also utilized an optical technique that quantifies feature quality. Various methods have previously been used to define or characterize feature reproduction quality.[6–8,13] In particular, the feature aspect ratio is characterized by the ratio of the feature width to its height. Microfluidic devices with irregular channels, raised features and non-linear pathways are difficult to characterize quantitatively, particularly the 'deep' channels of devices with high aspect ratio features. Sensors used in contact profilometry and atomic force microscopy (AFM) either do not measure on the appropriate length scale or use angled stylus tips, and thus these techniques do not provide high-resolution characterization for deep channels intended to have abrupt, right angle transitions. Here, conventional feature evaluation techniques were eschewed in favor of a novel, confocal microscopy technique that proved more appropriate for the characterization and quantification of

numerous feature reproduction attributes. Channel features for deep, narrow channels have previously been examined and measured using confocal microscopy.[14] Confocal microscopy provides the ability to focus on the feature area at desired feature heights, thus providing more accurate measurements for 'thick' or 'deep' features. The enhanced accuracy provided by confocal microscopy yields increased resolution in describing the entire topology of a feature. Here, we have quantified the optical data provided by confocal microscopy to determine an accurate, quantitative metric to describe the feature quality for any given feature type.

Ultimately, this work demonstrates the unique capability of thiol-ene photopolymerizations to enable the fabrication of complex, 3D microfluidic devices with improved feature fidelity and manufacturing capabilities, as exemplified in general features and in the specific production of a pinched-flow fractionation (PFF) device. Optimization of various aspects of the thiol-ene photopolymerization formulation and irradiation conditions is performed and comparisons to (meth)acrylate based formulations are incorporated.

2.2 Experimental

2.2.1 Materials

The aromatic urethane diacrylate (Ebecryl 4827) was donated by Cytec Surface Specialties (Smyrna, GA), and pentaerythritol tetra(3-mercaptoproprionate (PETMP) was donated by Evans Chemetics (Waterloo, NY). Triallyl-1,3,5-triazine 2,4,6 trione (TATATO), acrylic acid, and the iniferter precursor tetraethyl thiuram disulfide (TED) were purchased from Sigma-Aldrich (Milwaukee, WI). The inhibitor, N-nitrosophenyl-hydroxylamine (Q1301), was donated by Wako Pure Chemicals (Osaka, Japan). The initiators, Irgacure 651 and Irgacure 184, were donated by Ciba Specialty Chemicals (Tarrytown, NY). All materials were used as received without additional purification.

2.2.2 Methods

2.2.1 Fabrication

To fabricate microfluidic devices, the previously developed soft-lithography method known as contact liquid photolithographic polymerization (CLiPP) was used (Figure 2.1).[3,4] A modified one-step 'sandwich' methodology was used to fabricate channels with narrow channel features (<100 mm width). Glass cover slides were cleaned by etching with a solution consisting of 1 part hydrogen peroxide and 3 parts sulfuric acid for 3 h. The slides were then washed with deionized water and acetone. After cleaning, the slides were coated with methacryloxypropyl-trimethoxysilane (MPS), (Gelest, Morrisville, Pa.) by surface layer deposition, which involved placing the cleaned cover slides with 3 ml of MPS inside a sealed Teflon container. The Teflon container was placed inside an oven and heated to 70°C for 4 h. Subsequently, the monomer formulation was injected between the two treated glass cover slides, with a photolithographic mask attached to the surface. Masks were created with feature resolution of 50 mm (printed masks) or 1 mm (chrome masks), where the masks were used to fabricate wells, columns and bars that are either curved or straight. The monomer was exposed to a collimated light source from an optical mask alignment system (Optical Associates, Inc. San Jose, Ca) using a 5 x5 cm area collimated flood exposure source with irradiation intensity of 37.5 mW cm^{-2} with principal output at 365 nm. Irradiation intensities were measured using an International Light, model IL1400A radiometer (Newburyport, Ma.). Following the cure process, uncured monomer was removed by flushing the channels with methanol followed by removal of excess solvent and monomer, leaving only the patterned crosslinked polymer.

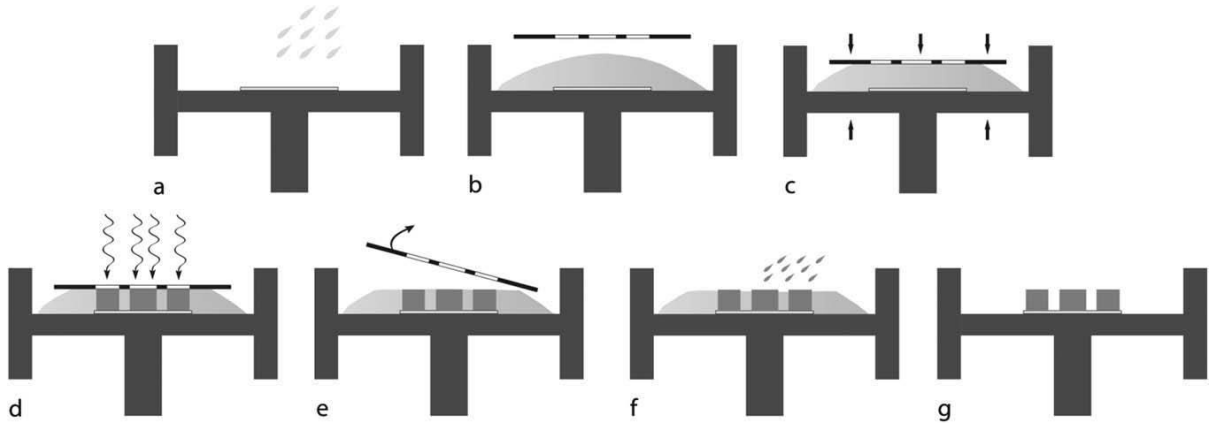

Figure 2.1 Schematic of the CLiPP process. Step a: The siloxane-treated glass slide is secured to the chamber base, a monomer mixture fills the chamber. Step b: After filling the chamber with monomer, an aligned mask is placed on top of the monomer resin. Step c: The mask is brought in contact with the monomer and lowered to the desired feature height. Step d: The monomer mixture is exposed to collimated 365 nm UV radiation through the aligned mask. Step e: The mask is removed from the cured monomer and discarded. Step f: Excess, uncured monomer is removed by washing with solvent. Step g: After washing, only the features attached to the substrate remain. Though not used here, the process can be repeated to create multilayer structures if desired.

2.2.2.2 Confocal microscopy analysis of polymeric features

Polymeric features were examined using confocal microscopy with an Axioplan upright microscope, Pascal software and a 4x air objective (Zeiss Achroplan 4x). Feature analysis was performed using the Zeiss LSM Image Examiner software program (Carl Zeiss Company). The polymer weakly auto fluoresces at excitation and emission wavelengths of 543 and 633 nm, which was subsequently used to detect the polymer structure and measure feature fidelity. Three-dimensional feature perimeters were measured for each scanned image, utilizing the area of each scanned layer to determine the feature volume by integrating over the feature depth.

2.2.2.3 Low vacuum scanning microscope (LVSEM) use.

High-resolution imagery of the PFF device was provided by LVSEM at 10 kV and low magnification (~75x). Charging is stabilized by a small amount (~30 Pa) of weakly ionized gas in the specimen chamber.

2.3 Results and discussion

2.3.1 Use of confocal microscopy for feature characterization

Confocal microscopy was utilized to provide data necessary to construct a 3D image used to quantify the actual feature volume and topology. Figure 2 shows a series of square recessed features and a 3D image of the corresponding feature generated from the confocal microscopy data. Characteristics of the features are calculated by relating the microscopy images to the desired feature shape as described in equation (1) for the channel fill. Feature quality, which increases as the channel fill decreases, is calculated using equation (2). For a channel with 0% fill (Feature quality = 1.0), there is no excess polymer in the channel, while a channel with 100% fill (Feature quality = 0.0), would represent a channel that is completely blocked by excess polymer formed from the undesired polymerization in what is intended to be the dark regions. In some

instances, such as when insufficient curing occurs, the channel void exceeds that of the ideal volume. For such cases of under cure, a negative value for channel fill is obtained and the feature quality value can become negative as well. Surface contour maps of channel features reveal curvature, roughness or irregularities, all of which impact feature quality. Using confocal microscopy results, acrylate and thiol-ene formulations were compared and optimized for the fabrication of both raised and recessed features.

$$\text{Channel Fill} = \frac{\left(\begin{matrix}\text{Ideal Volume}\\ \text{of Feature}\end{matrix}\right) - \left(\begin{matrix}\text{Volume of}\\ \text{Feature (measured)}\end{matrix}\right)}{\left(\begin{matrix}\text{Volume of}\\ \text{Ideal Feature}\end{matrix}\right)} \tag{2.1}$$

$$\text{Feature Quality} = 1 - |\,\text{Channel Fill}\,| \tag{2.2}$$

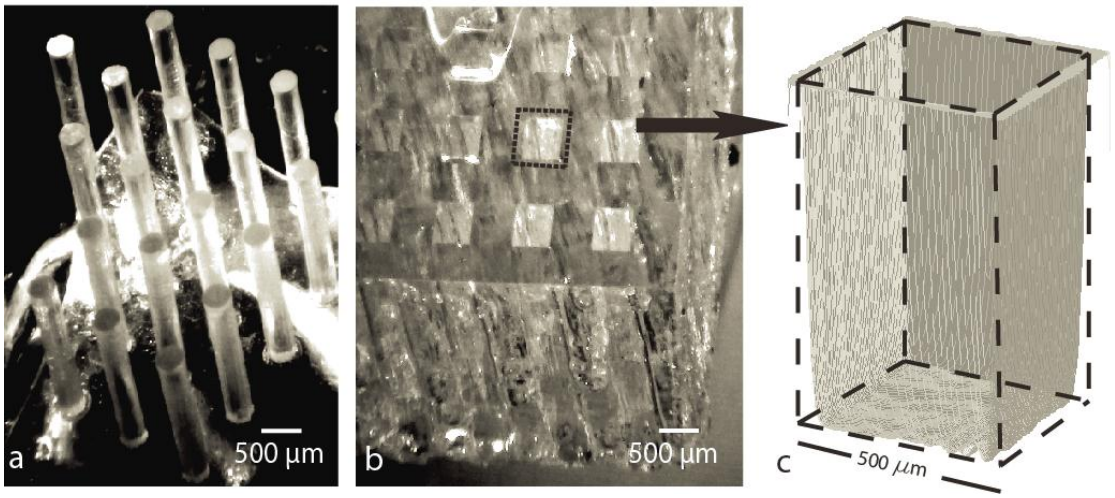

Figure 2.2 Photographs showing raised cylinders with an aspect ratio of 4.2 (a), recessed columns with an aspect ratio of 4.2 (b), and a 3D graphic representation of a portion of the highlighted recessed area (c). The graphic in (c) shows the feature topology compared to an 'ideal' volume (shown with dotted lines) that would be produced if the mask features were replicated perfectly throughout the feature volume. Here, the feature shown in (c) has a feature quality of 0.81. Features are fabricated using a thiol-ene resin containing PETMP and TATATO with a 1 : 1 stoichiometric thiol : ene ratio, 0.25 wt% Irgacure 651 and 0.25 wt% inhibitor (Q1301) with a cure time of 40 s. Fabrication of the feature uses a 5 x 5cm^2 area collimated flood exposure source having an irradiation intensity of 37.5 mW cm^{-2} and principal output at 365 nm.

2.3.2 Fabrication of high quality features

A stoichiometric thiol-ene (PETMP-TATATO) formulation was evaluated with varying ratios of initiator to inhibitor. It has been previously demonstrated that improved definition of feature boundaries and increased shelf-life result from increased inhibitor concentrations.[15] To evaluate feature quality, we fabricated square columns (500 x 500 mm) and cylinders (300 mm diameter) that are both raised and recessed, with varying feature height or depth to form structures having a range of aspect ratios. No significant differences in feature quality were found for cylinders versus square columns; therefore, data for cylinders and columns are presented together. Channel fill was measured while varying cure time with initiator concentrations of 0.05, 0.1, 0.25 and 0.5 wt% and inhibitor to initiator ratios of 0.5, 1.0 and 1.5. Feature quality was found to be the greatest for inhibitor : initiator ratios that were greater than unity, as shown in Figure 3, with cure time of 15 s. and an aspect ratio of 8. The use of increased amounts of inhibitor increases the cure dose necessary to overcome the inhibitor and initiate the polymerization. Using an inhibitor : initiator ratio of 1.0, feature quality versus initiator concentration and cure time were determined and are presented in Figure 4. The results demonstrate that the feature quality is dependent on the polymerization conditions, with higher initiator concentrations and higher exposure times leading to excess cure in undesired regions, and resulting in lower feature quality. The optimal thiol-ene resin polymerization conditions appear to be near the minimum cure time required for gelation, inhibitor to initiator ratios of 1 : 1 and 1.5 : 1 and at low initiator concentrations (0.05 wt%). Essentially, the maximum feature quality arises when minimal but sufficient polymerization occurs and a large amount of inhibitor is present to limit undesired polymer formation in unexposed regions.

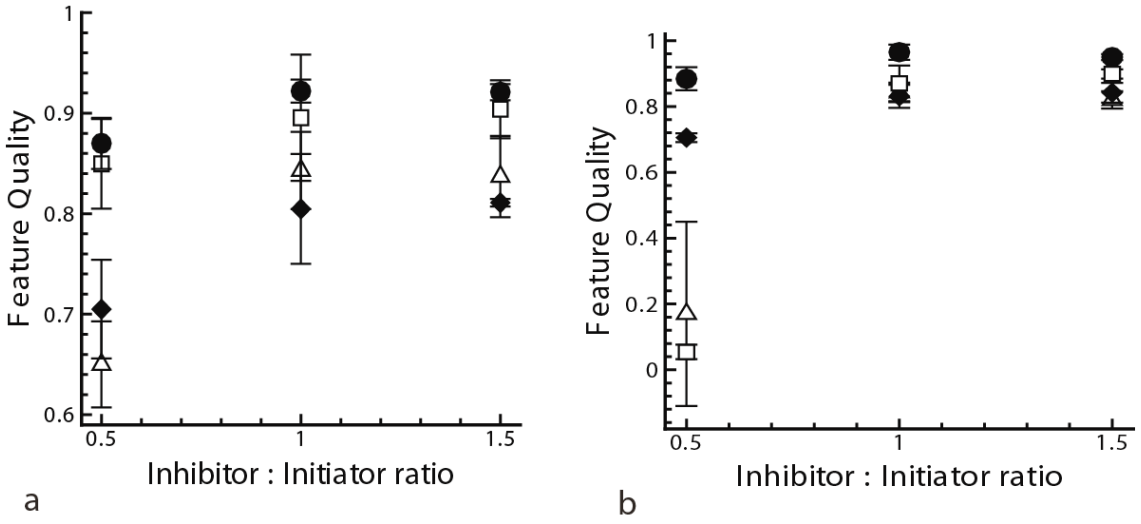

Figure 2.3 Feature quality for recessed (a) and raised (b) features versus Inhibitor:Initiator ratio ranges from 0.5 to 1.5, with 0.05 (●), 0.1 (□), 0.25 (◆) and 0.5 (△) wt% initiator with cure times of 15 seconds and an aspect ratio of 8. Fabrication of the features use a 5 x 5 cm^2 area collimated flood exposure source having an irradiation intensity of 37.5 mW/cm^2 and principal output at 365 nm.

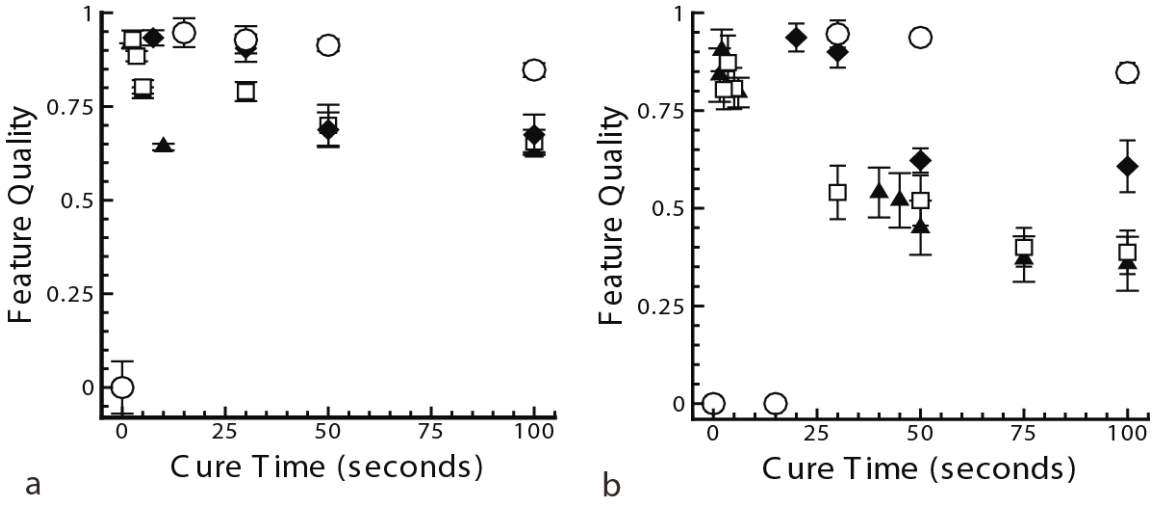

Figure 2.4 Feature quality for (a) raised and (b) recessed features versus cure time and initiator weight percent at an aspect ratio of 8, with 0.05 (○), 0.1 (◆), 0.25 (▲) and 0.5 (□) wt% initiator. Fabrication of the features uses a 5 x 5 cm^2 area collimated flood exposure source having an irradiation intensity of 37.5 mW/cm^2 and principal output at 365 nm.

2.3.3 Aspect ratio vs. feature quality for thiol-enes and acrylates

The acrylate formulation utilized here for comparison to the thiol-ene formulation was previously developed to fabricate microfluidic devices, and the formulation was not altered further for use in this work.[3,4] The distinct optimum curing times for the acrylate and thiol-ene resins were determined for aspect ratios varying from 1.5 to 11.0. The optimal cure times determined for each formulation are presented in Figure 5.

Using the optimized curing conditions for both the thiol-ene and acrylate formulations, feature quality versus aspect ratio is shown in Figure 6 for both raised and recessed features. Feature quality remains consistent for the optimized thiol-ene formulation for both raised and recessed features with aspect ratios ranging from 1.5– 13. Acrylate feature quality is comparable to that for thiol-enes for aspect ratios less than 3. However, the acrylate resin displayed a marked reduction in feature quality with increasing aspect ratio. For recessed features, the feature quality is 0.92 ± 0.04 for square depressions at an aspect ratio of 1.6 and steadily decreases to less than zero, i.e., highly under cured structures, for aspect ratios greater than 5. For raised features, feature quality is about 0.9 for aspect ratios up to 3 for circular columns. For square columns, the feature quality begins to decrease at aspect ratios greater than 3 and the feature quality is approximately 0.6 for both circular and square columns at an aspect ratio of 5.25. Degradation in feature quality for acrylate resins results from excess polymer formed in unwanted areas and/or under cure resulting from light attenuation and oxygen inhibition, depending on the reaction conditions. The long exposure times that are optimal for the acrylate system, in combination with the very small amount of conversion required to form a gel from this classical chain-growth polymer system, make it very difficult to form high quality, high aspect ratio structures from a conventional (meth)acrylate formulation. In contrast, the thiol-ene formulations require minimal

exposure times due to their rapid kinetics and resistance to oxygen inhibition. Further, because of the high gel-point conversion associated with the step-growth nature of the thiol-ene reaction and small degrees of polymerization resulting from undesired, non-specific initiation lead to the formation of only low-molecular-weight, soluble oligomers rather than gelled polymers. Both of these distinctions in the thiol-ene reaction behavior enable the formation of improved features and micro devices.

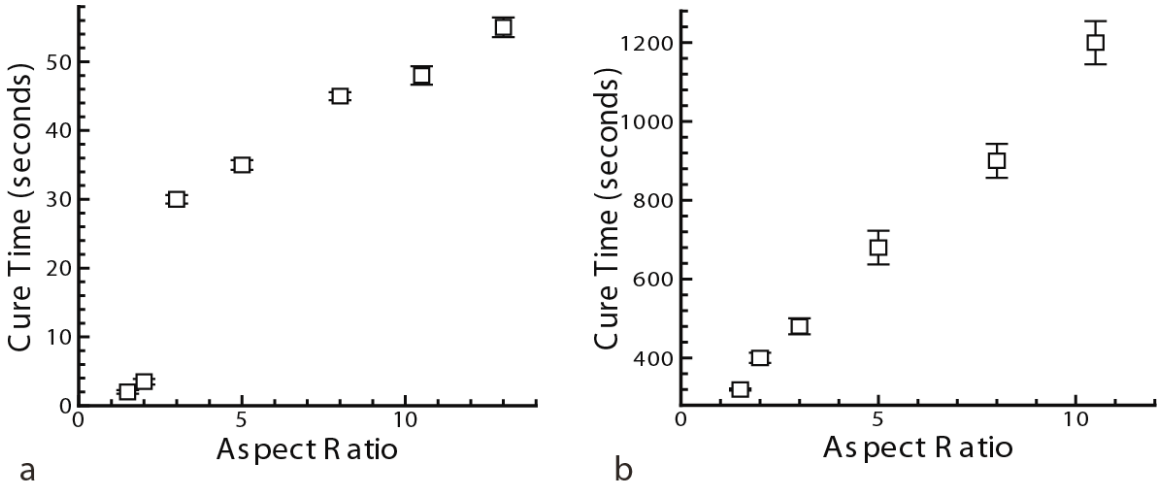

Figure 2.5 Optimum cure time for varying aspect ratios for raised thiol-ene features (a) (PETMP:TATATO, 1:1 stoichiometric, 0.25 wt% Irgacure 651 and 0.25 wt% Q-1301) and raised acrylate features (b) (48.8 wt% urethane diacrylate, 48.8 wt% TEGDA, 1.4 wt% Irgacure 184 and 1.0 wt% acrylic acid). Fabrication of the feature uses a 5 x 5 cm^2 area collimated flood exposure source having an irradiation intensity of 37.5 mW/cm^2 and principal output at 365 nm.

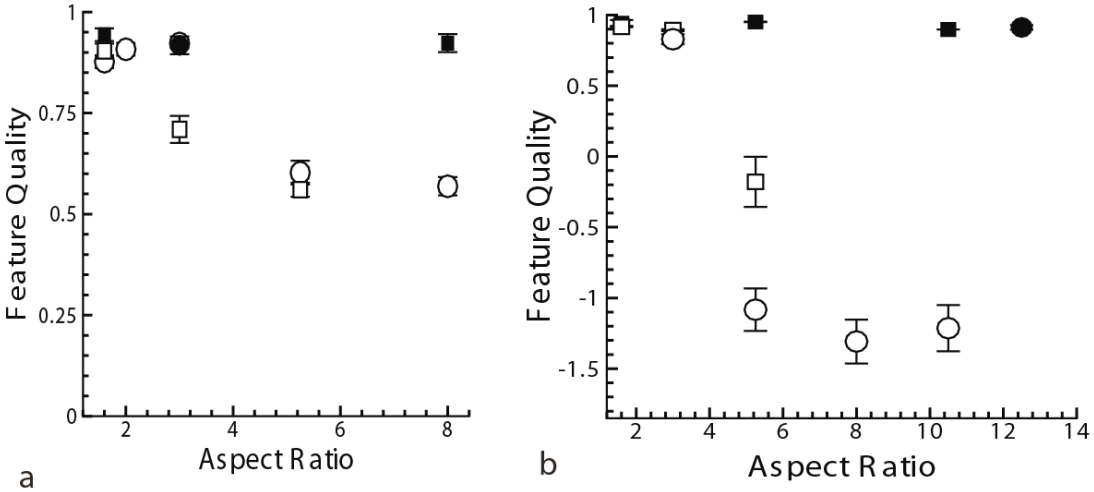

Figure 2.6 Feature quality versus aspect ratio for thiol-ene and acrylate resins. (a) Raised circular (●) and square (■) features for thiol-ene resins and raised circular (○) and square (□) features for acrylate resins. (b) Recessed circular (●) and square (■) features for thiol-ene resins and recessed circular (○) and square (□) features for acrylate resins. Circular features are 300 μm in diameter and square features are 500 μm on each side. Thiol-ene resins contained PETMP:TATATO with a 1:1 stoichiometric thiol-ene ratio, 0.10 wt% Irgacure 651 and 0.10 wt% inhibitor (Q1301). Acrylate resins contained 48.8 wt% urethane diacrylate, 48.8 wt% TEGDA, 1.4 wt% Irgacure 184 and 1.0 wt% acrylic acid. A 5 x 5 cm^2 area collimated flood exposure source was utilized with irradiation intensity of 37.5 mW/cm^2 and principal output at 365 nm for both thiol-ene and acrylate features.

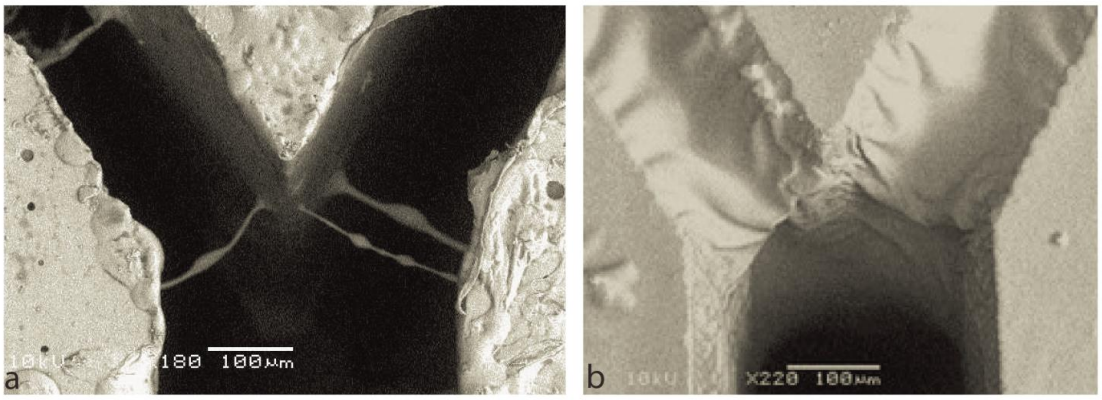

Figure 2.7 SEM images of the pinch area of the pinched-flow fractionation device. The images show the topology of the pinch area of the device fabricated from the thiol-ene (a) and acrylic (b) resins. The thiol-ene device was fabricated using resin containing PETMP and TATATO with a 1:1 stoichiometric thiol:ene ratio, 0.25 wt% Irgacure 651 and 0.25 wt% inhibitor (Q1301) with a cure time of 12 seconds. The acrylate formulation contains 48.8 wt% urethane diacrylate, 48.8 wt% TEGDA, 1.4 wt% Irgacure 184 and 1.0 wt% acrylic acid. The acrylate was photopolymerized for 400 seconds. A 5 x 5 cm^2 area collimated flood exposure source was utilized with irradiation intensity of 37.5 mW/cm^2 and principal output at 365 nm.

2.4.4 Fabrication of pinched-flow fractionation device

As a demonstration of the overall device-production capabilities of the thiol-ene formulations, optimized resin formulations and conditions were utilized to fabricate pinched-flow fractionation (PFF) microfluidic devices. PFF devices contain two inlet channels that combine in a pinch area, yielding a method for separating small particles based on fluid mechanics and steric effects.[16,17] The size and fidelity of the channel features strongly affect the ability of the device to effectively separate particles. The PFF devices fabricated here have channel width of 50 mm and depth of 500 mm, i.e., an aspect ratio of 10. For optimal particle separation, a PFF device requires non-deformable, glassy structures that are tolerant to solvents and exhibit low swelling. A 50 mm wide channel enables the pinch to be capable of separating cells or other particles ranging from 2 to 18 mm in diameter, such as those found in whole blood samples.[17] Such a pinched-flow fractionation device would enable the facile separation of platelets and erythrocytes by size from plasma in whole blood samples.

PFF devices fabricated from both the acrylate and thiol-ene resins are illustrated in Figure 7. SEM images of the pinch area of the device are shown at a 15° raised angle. The SEM images show that the higher aspect ratio entrance area of the device fabricated using the acrylate material is completely filled in (Figure 7b), rendering the channel unusable. By contrast, the channels of the thiol-ene device are clear and functional.

2.4 Conclusions

Microfluidic device features with a range of shapes and aspect ratios were fabricated via soft lithography using both thiol-ene and acrylate resins. Confocal microscopy was used to quantitatively determine feature quality and fidelity for a wide range of monomer formulations and conditions. Feature quality was used to ascertain optimum cure times, initiator to inhibitor ratio

and initiator concentrations for fabrication of microfluidic devices with high-definition features. For the thiol-ene formulations, optimal feature quality and aspect ratio were achieved for the lowest initiator concentrations and for inhibitor to initiator ratios ranging of 1 : 1 to 1.5 : 1. As aspect ratios increased, quality remained consistent and high (>0.85) using the optimized thiol-ene formulation. In contrast, significant decreases in feature quality were observed for features fabricated using the optimized acrylate resin, when the aspect ratios exceed 3. Thiol-ene formulations allow for the fabrication of a pinched-flow fractionation device with high-definition features. The characteristics of the thiol-ene reaction enable the fabrication of many varieties of high-quality features critical to microfluidic device performance.

2.5 Acknowledgements

The authors thank the Ashley/McCormick Research Institute 06204591 and the National Science Foundation CBET 0626023 for funding.

2.6 References

1 D. C. Duffy, J. C. McDonald, J. A. Schueller, G. M. Whitesides, Rapid Prototyping of Microfluidic Systems in Poly(dimethylsiloxane), *Anal. Chem.* **70**, 4974-4984 (1998).

2 B. R. Whiteside, M. T. Martyn, P. D. Coates, Micromoulding: process characteristics and product properties, *Plastics, Rubber, and Composites* **32**, 231-239 (2003).

3 K. T. Haraldsson, J. B. Hutchison, K. S. Anseth, C. N. Bowman, 3D polymeric microfluidic device fabrication via contact liquid photolithographic polymerization (CLiPP), *Sens. Actuators B, Chemical* **113**, 454-460 (2006).

4 J. B. Hutchison, K. T. Haraldsson, B. Good, R. Sebra, N. Luo, K. S. Anseth, C. N. Bowman, Robust polymer microfluidic device fabrication via contact liquid photolithographic polymerization (CLIPP), *Lab Chip* **4**, 658-662 (2004).

5 J. G. Kloosterboer, Network formation by chain crosslinking photopolymerization and its applications in electronics, *Adv. Polym. Sci.* **84**. 1-61 (2001).

6 C. E. Hoyle, T. Y. Lee, T. Roper, Thiol-Enes: Chemistry of the past with promise for the future, *Part A: Polym. Chem.* **42**, 5301-5338 (2004).

7 C. E. Hoyle, A. B. Lowe, C. N. Bowman, Thiol-click chemistry: a multifaceted toolbox for small molecule and polymer synthesis, *Chem. Soc. Rev.* **39**, 1355-1387 (2010).

8 C. E. Hoyle, A. B. Lowe, C. N. Bowman, Thiol-Ene click chemistry, *Angewandte Chemie* **49** , 1540-1573 (2010).

9 M. H. Bland, N.A. Peppas, Photopolymerized multifunctional (meth)acrylates as model polymers for dental applications, *Biomaterials* **17**, 1109-1114 (1996).

10 C. N. Bowman, C. J. Kloxin, Toward an enhanced understanding and implementation of photopolymerization reactions, *AlChE J.* **54** (2008) 2775-2795.

11 N. B. Cramer, C. N. Bowman, Kinetics of thiol-ene and thiol-acrylate photopolymerizations with real-time fourier transform infrared, *J. Polym. Sci., Part A: Polym. Chem*. **40**, 3311-3319 (2001).

12 S. K. Reddy, N. B. Cramer, C. N. Bowman, Thiol-vinyl mechanisms II: kinetic modeling of ternary Thiol-Vinyl Photopolymerizations, *Macromolecules* **39**, 3681-3687 (2006).

13 R. J. Whiteside, Noncontact optical profilometer, *App. Optics* **14**, 2480-2485 (1975).

14 T. Ode, A new technique for optical 3D measurements with a confocal scanning laser microscope, *IEEE Instrumentation and Measurement Technology* **2**, 672-676 (1994).

15 D. M. Glaser, Stabilization of thiolene compositions, *European Patent EP19920300934* filed 02/04/1992 and published 04/26/1995.

16 M. Nakashima, Pinched-flow fractionation (PFF) for continuous particle separation in a microfluidic device, *IEEE* 33-36 (2004).

17 J. Takagi, M. Yamada, M. Yasuda, M. Seki, Continuous particle separation in a microchannel having asymmetrically arranged multiple branches, *Lab Chip* **5**, 778-784 (2005).

Chapter 3

A Moving-Frame Boundary-integral Method for Particle Transport in Microchannels of Complex Shape

(Zinchenko, Ashley, and Davis (2012), *Phys Fluids* 24, 043302)

A new, three-dimensional algorithm is developed to accurately simulate low-Reynolds number, flow-driven motion of a neutrally buoyant spherical particle in plane-parallel microchannels of complex shape. The channel profile may consist of an arbitrary number of straight line segments with sharp corners in an arbitrary configuration. This geometry provides a suitable model for particle transport in many microfluidic devices with multiple branch bifurcations. The particle may be comparable with the narrowest channel dimensions, but is typically much smaller than the overall channel domain, which creates difficulties with a standard boundary-integral approach. To make simulations feasible, the 3D problem is solved locally in a computational cell that is smaller than the full domain and is dynamically constructed around the particle as it moves through the channel; the outer boundary conditions are provided by the 2D flow that would exist in the channel in the absence of the particle. Difficulties with particle-corner close interactions are alleviated using special iterative techniques, (near-) singularity subtractions and corner-fitted, gap-adaptive discretizations of the cell boundary. The algorithm is applied to simulate "pinched-flow fractionation" and predict how particle interactions with a narrow pinch region and sharp corners result in particle focusing and separation in the outlet according to their size. As another application, the particle motion through a T-bifurcation with sharp corners is simulated, with calculation of the particle flux partition ratio for a broad range of parameters. It is demonstrated how the particle-corner

interactions can make the side branch inaccessible to particles, even for relatively strong fluid suction through this branch.

3.1 Introduction

Flow-driven, low-Reynolds number motion of a solid particle in microchannels with solid walls is directly relevant to microfluidic devices, and can also serve as a useful model to clarify some salient features of cell motion in blood capillaries. For straight channels, two models have been most popular in theoretical studies, an infinite circular tube and a slit between two infinite parallel walls. When the particle is appreciably smaller than the tube diameter or slit width, and is away from the walls, the method of reflections can be used; for a spherical particle shape, the analytical solutions by this approach are discussed by Happel and Brenner.[1] For a tightly-fitting particle and/or particle close to the channel walls, however, necessary multiple reflections would require a formidable algebraic effort, and an alternative, numerical approach based on boundary-integral equations is more attractive. For a tube, early boundary-integral solutions exploited the domain Green function to reduce the problem to a boundary-integral equation on the particle surface only; however, an enormous cost of calculating and tabulating the Green function (even after subtraction of the singular part) has limited the results to small particles only, away from the walls.[2] The slit geometry is more amenable for the domain Green function approach, owing to efficient desingularization and tabulation,[3] and a comprehensive boundary-integral solution has been obtained for a particle tightly fitting the space between two parallel walls in Poiseuille flow. The results of Staben *et al.*[3] significantly extend prior calculations for a sphere by Ganatos *et al.*[4] (who used a collocation method), allowing for close particle-wall interaction, and also include spheroidal shapes (see also Staben *et al.*[5]). More recently, the slit geometry was extensively studied by a mixed Cartesian-multipole representation including interparticle

interactions;[6-9] the method of these authors allows simulations for closer particle-wall contact, although it is highly specific for the geometry and spherical shapes. For a single sphere, the results[9] are in agreement with those of Staben *et al.*[3]

Much less is known theoretically about particle motion in microchannels of complex shape, namely, with one or multiple branch bifurcations, although such geometries are of great relevance to particle transport in microfluidic devices. One example is "pinched-flow fractionation"[10-13] where particles, fed into one of the input sleeves, are pressed by a buffer liquid (entering another sleeve, with a higher flow rate) to the wall of the pinched area, interact with the corner of the pinch, then depart to the widening section and eventually exit through the outlet. This device was found to be efficient for particle separation in the outlet according to their sizes (ibid.), but rigorous CFD simulations of this process are still lacking.

Particle motion through even a single bifurcation displays a rich variety of different types of behavior, compared to the case of straight channels (where lateral migration requires particle non-sphericity or inertial effects, Ho and Leal[14]). Such models (with "Y," "T" or oblique bifurcations), although idealistic, have been of great interest to physiologists because of their relevance to blood circulation in capillaries and red-cell hematocritis (e.g., Chen *et al.*;[15] Ditchfield and Olbricht[16]). It is known that the particle partitioning between the two daughter branches does not necessarily follow the partitioning of the fluid volume, but, instead, the particles typically favor the high-flow-rate branch (the Zweifach-Fung effect[17,18]). While the assumed particle rigidity and geometry idealizations for the channel can grossly oversimplify the reality of red-cell motion in bifurcating blood capillaries, these theoretical models are more relevant to solid particle transport in microfluidic devices, where the particle shape and channel geometry can be controlled. From this perspective, motion of isolated solid spheres in model

bifurcations has been extensively studied. Roberts and Olbricht[19] performed experiments on "Y," "T" and oblique bifurcations formed by circular pipes, measured the particle flux partition ratios and suggested how the results for particle motion at a single bifurcation can be combined to design a practical microfluidic device with multiple bifurcations to separate particles. In the experiments of Roberts and Olbricht,[20] "Y" and oblique bifurcations were studied, with branching tubes of a square or rectangular cross-section. It was shown, in particular, that, for the channel depth twice the width of the tubes, the model of a plane-parallel channel becomes adequate. Again, a combination of multiple bifurcations was offered to enhance particle separation, and tested by experiments. A numerical study of Audet and Olbricht,[21] of particular relevance to the present work, clarified many qualitative features of a flow-driven, particle motion through single "Y" and "T"-shaped bifurcations, with calculation of the particle flux partition in a broad range of parameters. However, to arrive at a feasible solution with computer resources available at that time, these authors considered model, cylindrical particles in a plane-parallel geometry by 2D boundary-integral simulations; besides, to avoid numerical difficulties with sharp corners, the bifurcation joints were significantly smoothed. From a modern perspective, the model of cylindrical particles is an oversimplification; to date, however, we are not aware of any related simulations for realistic 3D particles.

The present work offers a three-dimensional, boundary-integral algorithm to accurately simulate flow-driven motion of a spherical particle in plane-parallel microchannels of complex shape. Possible alternative approaches are discussed in Section 3.2 (it was not possible, however, to make detailed comparisons, since we are not aware of alternative solutions of the 3D problems considered herein). The channel profile may consist of an arbitrary number of straight line segments with sharp corners in an arbitrary configuration. Geometries that can be simulated

include, in particular, the pinched-flow-fractionation (PFF) device of Nakashima *et al.*[10] and multiple bifurcation systems described in Roberts and Olbricht.[20] The particle may be comparable in size with the narrowest channel dimensions (and closely interacting with the walls/corners), but is often much smaller than the overall channel domain. This difference in length scales would make the boundary-integral solution for the entire domain prohibitively expensive. We describe instead in Section 3.3 how to solve the 3D boundary-problem in a local computational cell ("moving frame") dynamically constructed around the particle; the outer boundary conditions are provided by the 2D flow that would exist in the entire channel without the particle. Due to generality of the channel and cell shapes, a domain Green function approach must be abandoned in this problem; our 2D and 3D algorithms are based instead on the free-space Green functions. Section 3.3.1 contains the problem formulation and the general solution scheme. In Section 3.3.2, we outline the suitable 2D boundary-integral algorithm for the flow without the particle; despite the simplicity, this algorithm contains some special features to make calculations robust for channels of extreme shape with sharp corners. In Section 3.3.3, we discuss the details of the 3D algorithm, including the computational-cell construction, corner-fitted, gap-adaptive discretization of the cell boundary, the particle surface triangulations (with optional gap adaptivity–to better handle close particle-wall interactions), special (near) singularity subtractions in the boundary integrals suitable for the cell geometry with sharp corners, and a choice of a suitable iterative method. Due to a weak lubrication, the particle contact with a sharp corner can be reached with relatively little resistance (and in a finite time). Section 3.3.4 provides details on the strategy of our calculations once such contact is reached; the most natural assumption is that the contact can only be maintained under a compressive load. Note that no models of surface roughness are required for particle-corner interactions. As an

alternative, it would seem natural to smooth sharp corners in the simulations. Within the present algorithm, the straightforward way to do it would be to use a large number of straight line segments for the channel profile in the corner regions. However (unless the smoothing radius is excessively large), the 3D particle would still be able to come extremely close to the corner, creating uncertainties and even more difficulties. For this reason, we do not favor artificial smoothing and prefer sharp corners. We note finally that the spherical particle shape was chosen herein mostly for computational efficiency. The approach and the bulk of the algorithm can be readily extended for particles of more general shapes; such generality, however, would not be justified in the present work focused on the channel-shape complexity.

Section 3.4 contains numerical tests. In Section 3.4.1, our simple 2D algorithm, used for the flow without a particle, is shown to be robust and accurate in different geometries with sharp corners. Section 3.4.2 contains more limited testing of our 3D algorithm with a particle, and comparisons are made with domain-Green-function, boundary-integral solutions for a particle near one wall, and in a slit between two walls. In Section 3.5, novel dynamical simulations for a 3D particle in microchannels of complex shape are presented. The PFF device considered in Section 3.5.1 is an example of a geometry where the idea of the moving-frame solution is particularly advantageous. Likewise, one could expect this solution technique to be very advantageous for simulation of particle transport through a channel with multiple bifurcations (and short pipe segments in between, so that different bifurcations could not be treated as independent). However, in Section 3.5.2, we apply our algorithm to a simpler problem of flow-induced particle motion through a single, "T"-shaped bifurcation, since this important case has not been simulated in prior work for realistic, 3D particles. It was not possible, unfortunately, to quantitatively compare our results with the experimental work of Roberts and Olbricht,[20] since

the latter does not include "T" shapes. However, the comparison with 2D simulations of Audet and Olbricht[21] in Section 3.5.2 shows that the particle three-dimensionality and/or sharp corners of the bifurcation have significant effect on the particle-flux partition ratio.

All the results in this paper were generated by single-core calculations on a PC, with Intel Core i7 965/975 CPU (3.2/3.33 GHz).

3.2 Other Numerical Approaches

Among the alternative methods, potentially suitable for simulating solid particle transport in microchannels of complex shape, are the Immersed Boundary (IB), the fictitious-domain distributed Lagrange multiplier (DLM) and the extended finite-element (X-FEM) methods. The popular IB method was originally developed[22] for viscous flows near deformable elastic solids. The basic idea is to extend the Navier Stokes solution to the interior of the solids, and to enforce the no-slip boundary condition through a distributed body force. The finite-difference mesh does not have to body-fit the solid boundaries, and fast Navier-Stokes solvers for the whole domain (typically cubical) can be often used. In the original form, IB suffered from severe stability limitations (making it hard to approach the limit of absolutely rigid boundaries) and was only first-order accurate; these drawbacks were overcome in later versions[23,24] (and references therein). The DLM[25-37] also extends the solution to the interior of rigid boundaries, but the no-slip boundary condition is enforced through the use of distributed Lagrange multipliers. In the available implementations, DLM is only first-order accurate and was observed to require very fine meshing to reach good results in relatively-simple, Stokes-flow problems as tests[27]. The advantages of IB and DLM include their ability to simulate finite Reynolds number flow and easy meshing. The main drawback is that embedding a channel of complex shape (e.g., with multiple bifurcations) into a simple, cubic-like domain (with typically a uniform mesh

throughout) can add too many fictitious nodes, which is viewed as uneconomical[23]. Besides, we are not aware of any comprehensive testing of 3D IB codes in the creeping flow limit $\mathrm{Re} \to 0$, and this limit may be difficult for time-marching, Navier-Stokes solvers. The present solution by the proposed moving-frame boundary-integral method is for $\mathrm{Re} = 0$ only, but it is based on special discretization in the essential region only, and allows for systematic dynamical simulations with much higher resolutions than would be practical by IB or DLM. The Stokes flow approximation, relevant to most microfluidics applications, has one other, very significant advantage in the systematic analysis of the problems considered herein. Namely, efficient classification of the trajectories in the pinch-flow problem (Section 3.5.1) and calculation of the particle flux partition ratio in the "T"-channel problem (Section 3.5.2) are based on backward integration of selected trajectories from a sharp corner. This feature exploiting reversibility of the Stokes flow would be lost altogether for finite Reynolds numbers, and one would have to resort instead to much more expensive forward trajectory integrations by many trials and errors.

In the X-FEM developed for bounded 2D Stokes flows with circular particles[28,29], the finite element mesh is extended throughout the particles and need not conform to the particle surfaces. The FE base is enriched by local analytical solutions for a single particle to facilitate no-slip boundary conditions. In Ref. [29], the base is also enriched by local 2D lubrication solutions for particle-particle and particle-wall interactions. Despite these lubrication corrections (much stronger than they would be in the realistic 3D case), it was still necessary to add artificial repulsion to prevent surface overlapping in simulations with several suspended particles. In 3D, there are several general schemes in the literature for lubrication corrections; their analysis, however, is outside the scope of the present paper. It will suffice to mention that we have been unable so far to find a scheme beneficial for the problems considered herein. Since we focus on

particle trajectories, not on temporal dynamics, the overall accuracy and particle-corner interactions are far more important than fully resolving particle-wall interactions.

3.3 Moving-Frame, Boundary-Integral Method

3.3.1 Formulation of the Problem

Consider transport of a three-dimensional, neutrally-buoyant solid particle S_p in a plane-parallel microchannel of complex shape. A typical cross-section of the channel by the plane $x_3 = 0$, which is of interest in the pinched-flow fractionation, is shown in Figure 3.1. The third dimension of the channel is assumed to be large, and the channel in Figure 3.1 extends infinitely from $x_3 = -\infty$ to $x_3 = \infty$ along the x_3-axis perpendicular to the plane of the drawing (not shown); x_1, x_2, x_3 form a right coordinate system in space. The channel profile consists of an arbitrary number of successive straight line segments $\mathcal{L}_1$, $\mathcal{L}_2$,…$\mathcal{L}_M$ (M =13 for Figure 3.1) in arbitrary configuration. The corresponding portions of the 3D channel boundary are strips S_1, S_2,…S_M ("panels") infinitely extended along the x_3-axis from $x_3 = -\infty$ to $x_3 = \infty$. In typical microfluidics applications, the Reynolds number is small, and creeping flow (Stokes) equations are assumed to apply. On each of the inlet/outlet panels (S_1, S_4, and S_9, respectively, for the channel in Figure 3.1), the fluid velocity $\boldsymbol{u}$ is prescribed, e.g., by a plane Poiseuille flow $\boldsymbol{u}_P$ (normal to the panel) with a given flux (and the sum of all inlet/outlet fluxes being zero). Such a choice is justified, since, for most of the simulation, the particle is away from the inlet/outlet channel sections. On the other panels (channel walls), $\boldsymbol{u} = \mathbf{0}$ due to the no-slip boundary condition. Gravitational effects are neglected, so the particle is force-free and torque-free.

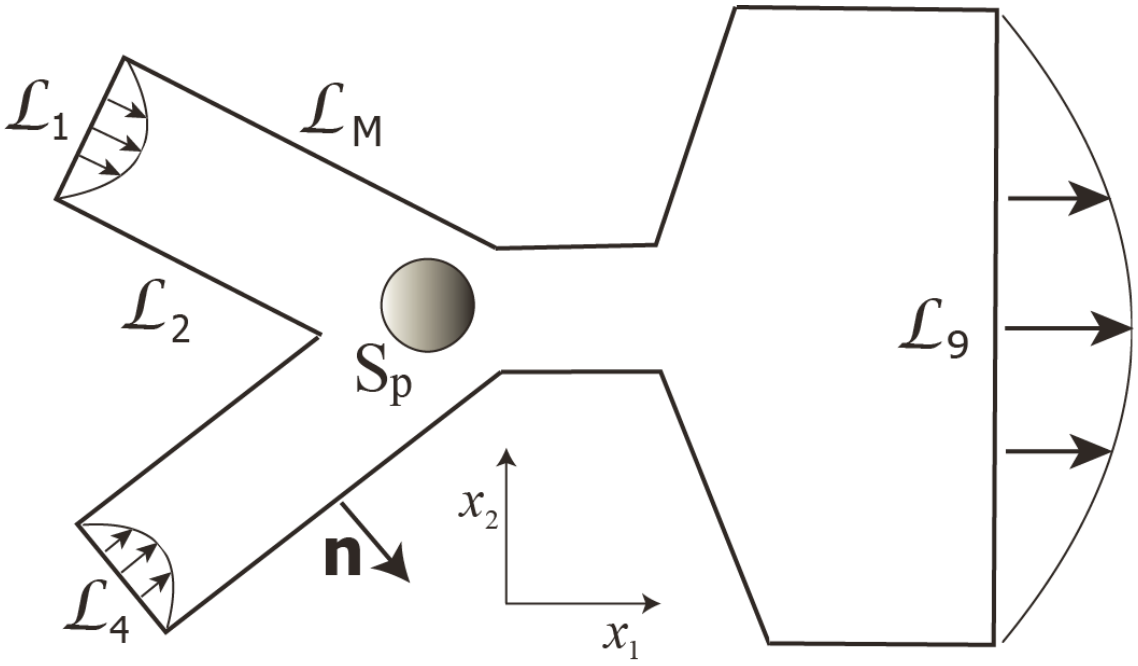

Figure 3.1 A schematic for particle transport in a plane-parallel microchannel of complex shape (not to scale).

In principle, this quasi-static problem could be reduced, at each time step, to solving 3D boundary-integral equations simultaneously on the particle surface S_p and the entire channel boundary $S_1 \cup S_2 \cup \ldots S_M$ (with additional domain truncations in the x_3-direction), to determine the instantaneous particle velocities (translational and rotational) and advance its position to the next time step. Such a numerical solution, though, by standard boundary-integral techniques, can hardly be efficient for the channels of the type shown in Figure 3.1. In simulations of interest, the particle size is comparable with the width of the narrow channel portions, but much smaller than the overall channel domain size. As the particle advances through different portions of the channel from inlet to outlet, accurate resolution of close particle-wall interactions requires surface mesh elements much smaller than the particle size. This limitation makes the total number of elements on the entire channel boundary too large, and numerical solution at each time step prohibitively expensive. Such calculations could likely be expedited by different kinds of multipole acceleration techniques. From our experience in other problems (e.g., Zinchenko and Davis[30-32]), however, efficient implementation of multipole acceleration in 3D makes programming quite involved.

In the present paper, we offer a much-simpler, yet efficient, new approach ("moving-frame boundary-integral method"), to simulating a single particle transport in complex geometries with accuracy sufficient for practical applications, based on the separation of scales. First, we calculate the velocity $\boldsymbol{u}_\infty$ for the fluid flow in the entire channel without the particle, from the solution of a 2D boundary-integral problem with the same (prescribed) inlet and outlet boundary conditions, and no slip on the channel walls. If the inlet/outlet conditions are stationary (as is the case for our simulations in Section 3.5), this 2D solution needs to be obtained only once. The velocity $\boldsymbol{u}_\infty$ is then used as the outer boundary condition to solve a 3D problem in a

computational cell dynamically constructed around the particle, as it moves through the channel; it is essential that this computational cell, being much larger than the particle size, is still much smaller than the overall channel dimension, with manyfold savings in the CPU time (compared to a 3D boundary-integral method for the entire domain) and feasible solution. We refer to this approach as a "moving frame," because the computational cell on which the quasi-static Stokes equations are solved at each time step moves along with the particle. The implementation details of our algorithm are described below.

3.3.2 A Boundary-integral Algorithm for a 2D Flow without a Particle

Let $\boldsymbol{u}^b$ be the prescribed values of the fluid velocity $\boldsymbol{u}_\infty$ on the channel boundary ($\boldsymbol{u}^b = \mathbf{0}$ on the walls and $\boldsymbol{u}^b$ given, for example, by Poiseuille flows in the inlet/outlet sections). Inside the channel, the fluid velocity $\boldsymbol{u}_\infty(\boldsymbol{y})$ is sought in a standard way as a double-layer contribution from the entire channel contour $\mathcal{L} = \mathcal{L}_1 \cup \mathcal{L}_2 \cup \ldots \mathcal{L}_M$:

$$\boldsymbol{u}_\infty(\boldsymbol{y}) = \sum_{i=1}^{M} 2\int_{\mathcal{L}_i} \boldsymbol{q}_\infty(\boldsymbol{x}) \cdot \boldsymbol{\tau}^{2\mathrm{D}}(\boldsymbol{r}) \cdot \boldsymbol{n}(\boldsymbol{x})\, ds_{\boldsymbol{x}} \quad , \tag{3.1}$$

where $\boldsymbol{r} = \boldsymbol{x} - \boldsymbol{y}$, ds is the length element, $\boldsymbol{\tau}^{2\mathrm{D}}$ is the fundamental stresslet in two dimensions:[33]

$$\boldsymbol{\tau}^{2\mathrm{D}}(\boldsymbol{r}) = \frac{1}{\pi}\frac{\boldsymbol{rrr}}{r^4} \quad , \quad r = |\boldsymbol{r}| \tag{3.2}$$

$\boldsymbol{n}(\boldsymbol{x})$ is the outward unit normal to contour $\mathcal{L}$, and $\boldsymbol{q}_\infty(\boldsymbol{x})$ is a yet-unknown potential density. "Wielandt's deflation for a container"[33-35] produces an integral equation with unique solution amenable for iterative methods. First, a transformation $\boldsymbol{q}_\infty(\boldsymbol{x}) = \tilde{\boldsymbol{q}}_\infty(\boldsymbol{x}) - \frac{1}{2}\tilde{\boldsymbol{q}}'_\infty(\boldsymbol{x})$ to a new unknown $\tilde{\boldsymbol{q}}_\infty(\boldsymbol{x})$ is made, where the prime denotes the projection of a vector field on the space of rigid-body motions. In 2D, this "rigid-body projection" is simply calculated as

$$\tilde{\boldsymbol{q}}'_\infty(\boldsymbol{x}) = \boldsymbol{A} + \boldsymbol{B} \times (\boldsymbol{x} - \boldsymbol{x}_0) \quad , \tag{3.3}$$

where

$$\boldsymbol{x}_0 = \frac{1}{L}\int_{\mathcal{L}} \boldsymbol{x}\, ds \quad , \tag{3.4}$$

is the contour centroid (L being the total contour length),

$$\boldsymbol{A} = \frac{1}{\mathcal{L}}\int_{\mathcal{L}} \tilde{\boldsymbol{q}}_\infty(\boldsymbol{x})\, ds \quad , \tag{3.5}$$

and

$$\boldsymbol{B} = (0,0,B) \quad , \quad B = \frac{\int_L \left[\hat{x}_1 (q_\infty)_2 - \hat{x}_2 (q_\infty)_1\right] ds}{\int_{\mathcal{L}} \hat{\boldsymbol{x}}^2 ds} \quad , \tag{3.6}$$

with $\hat{\boldsymbol{x}} = \boldsymbol{x} - \boldsymbol{x}_0$.

Taking the limit $\boldsymbol{y} \to \mathcal{L}$ (from inside the contour $\mathcal{L}$) gives the desired integral equation

$$\tilde{\boldsymbol{q}}_\infty(\boldsymbol{y}) = \boldsymbol{u}^b(\boldsymbol{y}) - 2\int_{\mathcal{L}} \tilde{\boldsymbol{q}}_\infty(\boldsymbol{x}) \cdot \boldsymbol{\tau}^{2D}(\boldsymbol{r}) \cdot \boldsymbol{n}(\boldsymbol{x})\, ds_x + \tilde{\boldsymbol{q}}'_\infty(\boldsymbol{y}) - \frac{\boldsymbol{n}(\boldsymbol{y})}{L}\int_{\mathcal{L}} \tilde{\boldsymbol{q}}_\infty(\boldsymbol{x}) \cdot \boldsymbol{n}(\boldsymbol{x})\, ds_x \tag{3.7}$$

for $\tilde{\boldsymbol{q}}_\infty(\boldsymbol{y})$ on the entire channel contour. We divide each line segment $\mathcal{L}_i$ into $N_i \gg 1$ equal intervals and collocate equation (3.7) in midpoints $\boldsymbol{x}_j$ of the intervals. Due to sharp corners in the geometries of interest (Figure 3.1), the singular, double-layer integral in (3.7) is treated in a special way. Let $\boldsymbol{x}^* = \boldsymbol{x}^*(\boldsymbol{y}, i)$ be the mesh node $\boldsymbol{x}_j$ on the line segment $\mathcal{L}_i$ which is closest to $\boldsymbol{y}$. The double-layer contribution of segment $\mathcal{L}_i$ is calculated as

$$\int_{\mathcal{L}_i} \tilde{\boldsymbol{q}}_\infty(\boldsymbol{x}) \cdot \boldsymbol{\tau}^{2D}(\boldsymbol{r}) \cdot \boldsymbol{n}(\boldsymbol{x})\, ds_x = \int_{\mathcal{L}_i} \left[\tilde{\boldsymbol{q}}_\infty(\boldsymbol{x}) - \tilde{\boldsymbol{q}}(\boldsymbol{x}^*)\right] \cdot \boldsymbol{\tau}^{2D}(\boldsymbol{r}) \cdot \boldsymbol{n}(\boldsymbol{x})\, ds_x + \tilde{\boldsymbol{q}}(\boldsymbol{x}^*) \cdot \int_{\mathcal{L}_i} \boldsymbol{\tau}^{2D}(\boldsymbol{r}) \cdot \boldsymbol{n}(\boldsymbol{x})\, ds_x . \tag{3.8}$$

The first, non-singular integral in the RHS of equation (3.8) (as well as other non-singular integrals in (4)-(7)) is calculated with second-order accuracy by the simplest midpoint integration

rule on the mesh of $\{\boldsymbol{x}_j\}$; the last integral in equation (3.8) is handled analytically (Appendix 3.A). The contribution to (3.8) from segment $\mathcal{L}_i$ containing the node $\boldsymbol{y}$ is zero and omitted.

It would be simpler, and more in line with traditional singularity subtraction techniques, to use a unified choice $\boldsymbol{x}^* = \boldsymbol{y}$ for all line segments $\mathcal{L}_i$ in equation (3.8) (that way, only the sum of all added-back integrals in (3.8), which is $\boldsymbol{I}/2$, would be required). Such an approach proves to be inferior, however, as we found it to have much slower convergence when the discretization is increased, obviously due to sharp corners in the geometry.

Theoretically, a fully deflated equation (3.7) has a spectral radius less than one,[33-35] allowing for solution by "simple iterations" (successive substitutions of the previous iterate into the RHS of (3.7)). Such a procedure, indeed, works for many geometries of interest with sharp corners, but not for extreme cases where the overall size of the channel domain is much larger than the width of narrow portions, and the input sleeves are long enough. In these extreme cases, using a more-powerful, minimal-residual method and manyfold increase in resolution still could not provide convergent iterations. In our tests for different geometries, a universal remedy was found by using the biconjugate-gradient method to solve equation (3.7), with always convergent iterations, although it makes the solution more complex, requiring an adjoint to the discretized equation (3.7). Note that alternative, non-iterative solutions based on the first-kind integral equation for surface tractions have been popular and successful (e.g., Ref. [36]). However, we do not favor such an approach for extreme geometries (see above), where it may require a large total number of boundary elements, and suffer from ill-conditioning and computational cost.

Once the potential $\boldsymbol{q}_\infty(\boldsymbol{x})$ from the solution is tabulated (prior to dynamical simulations with the particle), the form (3.1) together with regularization (3.8) are used for fast calculation of $\boldsymbol{u}_\infty(\boldsymbol{y})$ inside the channel. The solution for $\boldsymbol{q}_\infty(\boldsymbol{x})$ with up to several hundred nodes per line

segment $\mathcal{L}_i$ (and N_i roughly proportional to the length of $\mathcal{L}_i$) provided high accuracy and required less than a minute of CPU time on a PC and 50-80 biconjugate-gradient iterations. The potential $\boldsymbol{q}_\infty(\boldsymbol{x})$ was found to be non-singular and continuous over the entire contour $\mathcal{L}$, with finite, but generally discontinuous one-sided derivatives along $\mathcal{L}_i$ at the corner points; it would not make sense, for such distributions, to use meshes adaptive to the corners in the boundary-integral solution.

Kelmanson[37] offered an improvement of 2D boundary-integral solutions in the vicinity of shape irregularities (sharp corners) by taking into account an asymptotic solution near the corner, subtracting off its contribution and solving a modified boundary-integral equation. While this more sophisticated approach is meaningful for the flow in a rectangular cavity with a moving wall,[37] or the "stick-slip" problem in Kelmanson,[38] the improvement through this procedure is less than obvious for flows with continuous boundary conditions for the velocity, like in a flow around a sharp corner. In fact, example B (flow past a step constriction) in Kelmanson[37] shows (Tables 3.4 and 3.6 therein) that the modification can noticeably reduce global accuracy away from corners. In the present calculations with more complex geometries (Figure 3.1), we have found it unnecessary to incorporate local analytical solutions near sharp corners. Numerical tests validating our 2D algorithm are discussed in Section 3.4.1.

3.3.3 Solution of a 3D Problem for the Particle in a Moving Frame

The instantaneous particle velocities, translational ($\boldsymbol{V}$) and rotational ($\boldsymbol{\Omega}$), are found from the solution of a 3D boundary-integral problem in a computational cell surrounding the particle, with the outer boundary conditions provided by the 2D solution (without the particle) described in the previous subsection. The 2D contour $\mathcal{C}$ of the cell in the plane $x_3 = 0$ is first constructed from an

intersection of a square centered at the particle center (with square sides parallel to the coordinate axes x_1, x_2) and the $x_3 = 0$ cross-section of the channel domain. The length 2A of the square side is chosen to be much larger than the particle diameter $2a$ (roughly 4-10 times) and, when possible, much smaller than the overall channel domain size. Figure 2 illustrates just several possible shapes of contour $\mathcal{C}$ for a fairly large particle, when the square intersects opposite channel walls; for smaller particles, the square is also smaller, and the contour shapes simplify accordingly. With a fixed value of A, as the particle moves through the channel, the shape and the number N of sides of contour $\mathcal{C}$ can change significantly. For a channel with an arbitrary geometry of straight line segments $\mathcal{L}_1,\ldots\mathcal{L}_M$ (e.g., Figure 3.1) and an arbitrary particle location, an automatic generation of contour $\mathcal{C}$ is not simple; some details of programming and restrictions are highlighted in the Appendix.

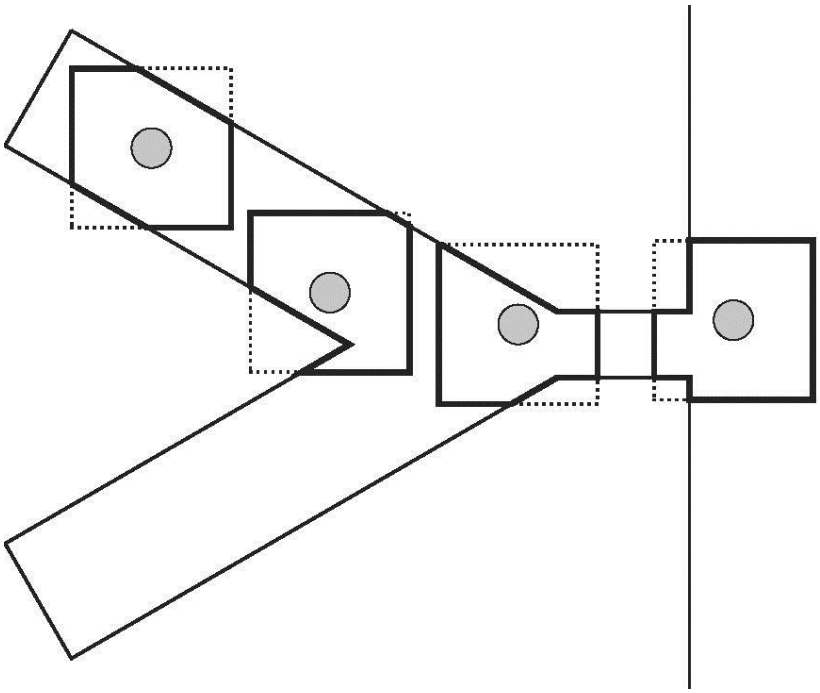

Figure 3.2 Dynamical construction of the computation cell contour (bold) around the particle, as it moves through different parts of the channel in pinched-flow fractionation simulations. Only a portion of the entire channel is shown.

Each of the line segments $\mathcal{L}_1^\infty,\ldots\mathcal{L}_N^\infty$ constituting contour C generates a corresponding rectangular panel $S_1^\infty,\ldots S_N^\infty$, respectively, by adding the third dimension in the range $|x_3| \le A$. These panels form the side surface $S_\infty = S_1^\infty \cup \ldots S_N^\infty$ of the computational cell. Finally, the top S_{top}^∞ and bottom S_{bottom}^∞ portions, obtained by translating the interior of $\mathcal{C}$ along the x_3-axis to $x_3 = A$ and $x_3 = -A$, respectively, are added to S_∞ to form a closed surface S_c of the computational cell around the particle. With the outer boundary condition $\boldsymbol{u}(\boldsymbol{y}) = \boldsymbol{u}_\infty(\boldsymbol{y})$ on S_c, the fluid velocity $\boldsymbol{u}(\boldsymbol{y})$ inside the cell is sought in terms of double-layer contributions from the cell and the particle (S_p) surfaces:

$$\boldsymbol{u}(\boldsymbol{y}) = \boldsymbol{u}_\infty(\boldsymbol{y}) + 2\int_{S_c+S_p} \boldsymbol{q}(\boldsymbol{x})\cdot\boldsymbol{\tau}(\boldsymbol{r})\cdot\boldsymbol{n}(\boldsymbol{x})\,dS_{\boldsymbol{x}} \quad , \tag{3.9}$$

where $\boldsymbol{r} = \boldsymbol{x} - \boldsymbol{y}$, $\boldsymbol{n}(\boldsymbol{x})$ is the outward unit normal (to S_c or S_p), and

$$\boldsymbol{\tau}(\boldsymbol{r}) = \frac{3}{4\pi}\frac{\boldsymbol{rrr}}{r^5} \tag{3.10}$$

is the fundamental stresslet in three dimensions (e.g., Ladyzhenskaya[39], and $\boldsymbol{q}(\boldsymbol{x})$ is a potential density to be determined. It is well-known that the form (3.9) automatically provides force- and torque-free conditions for the particle.[33-35,39-41] The boundary conditions yield a system of standard integral equations[33-35] for $\boldsymbol{q}(\boldsymbol{x})$ with yet unknown particle velocities $\boldsymbol{V}$ and $\boldsymbol{\Omega}$. The solution is not unique, since an arbitrary "rigid-body" motion (RBM) can be added to $\boldsymbol{q}(\boldsymbol{x})$ on S_p. Besides, there is a one-parameter family of eigensolutions on the cell boundary S_c; an arbitrary eigensolution can be added to $\boldsymbol{q}(\boldsymbol{x})$ on S_c, without affecting the flow inside S_c defined by (3.9). We follow the procedure of partial "Wielandt's deflation" for a container and a particle[33-35] to transform the boundary-integral equations to a form with unique solution. First, $\boldsymbol{q}(\boldsymbol{x})$ on S_p is constrained by

$$\boldsymbol{V}+\boldsymbol{\Omega}\times\left(\boldsymbol{y}-\boldsymbol{x}_c\right)=\boldsymbol{q}'\left(\boldsymbol{y}\right) \quad , \tag{3.11}$$

where the prime denotes the projection of the vector field on the space of rigid-body motions (see below), and

$$\boldsymbol{x}_c=\frac{1}{S_p\int_{S_p}\boldsymbol{x}\,dS} \tag{3.12}$$

is the particle surface centroid. On the cell boundary S_c, an appropriate eigensolution (see above) can be added to $\boldsymbol{q}(\boldsymbol{x})$ to make the total flux of $\boldsymbol{q}(\boldsymbol{x})$ through S_c equal to zero. Another observation (confirmed by the analysis and numerical tests in Section 3.4.2) is that, for a large cell ($A\gg a$), the contributions of the top S_{top} and bottom S_{bottom} portions of the cell boundary S_c to the boundary integrals with $\boldsymbol{q}(\boldsymbol{x})$ can be neglected; a likely explanation is that $\boldsymbol{q}(\boldsymbol{x})$ vanishes away from the particle. So, we arrive at the following well-behaved partially-deflated system of second-kind integral equations:

$$\boldsymbol{q}\left(\boldsymbol{y}\right)=-2\int_{S_\infty+S_p}\boldsymbol{q}\left(\boldsymbol{x}\right)\cdot\boldsymbol{\tau}\left(\boldsymbol{r}\right)\cdot\boldsymbol{n}\left(\boldsymbol{x}\right)dS_{\boldsymbol{x}}-\frac{\boldsymbol{n}\left(\boldsymbol{y}\right)}{S_c}\int_{S_\infty}\boldsymbol{q}\cdot\boldsymbol{n}\,dS \tag{3.13}$$

for $\boldsymbol{y}\in S_p$, and

$$\boldsymbol{q}\left(\boldsymbol{y}\right)=\boldsymbol{u}_\infty\left(\boldsymbol{y}\right)+2\int_{S_\infty+S_p}\boldsymbol{q}\left(\boldsymbol{x}\right)\cdot\boldsymbol{\tau}\left(\boldsymbol{r}\right)\cdot\boldsymbol{n}\left(\boldsymbol{x}\right)dS_{\boldsymbol{x}}-\boldsymbol{q}'\left(\boldsymbol{y}\right) \tag{3.14}$$

for $\boldsymbol{y}\in S_p$. Equation (3.11) is implemented simply as (Zinchenko *et al.*[42])

$$\boldsymbol{V}=\frac{1}{S_p}\int_{S_p}\boldsymbol{q}\left(\boldsymbol{x}\right)dS \quad , \quad \boldsymbol{\Omega}=\boldsymbol{D}^{-1}\int_{S_p}\hat{\boldsymbol{x}}\times\boldsymbol{q}\,dS \quad , \tag{3.15}$$

where the positive definite matrix $\boldsymbol{D}$ is

$$\boldsymbol{D}=\int_{S_p}\left[|\,\hat{\boldsymbol{x}}\,|^2\,\boldsymbol{I}-\hat{\boldsymbol{x}}\hat{\boldsymbol{x}}\right]dS \quad , \quad \hat{\boldsymbol{x}}=\boldsymbol{x}-\boldsymbol{x}_c \quad . \tag{3.16}$$

It would be tempting to make the outer integration surface even more open and exclude the panels that do not belong to the solid walls from S_∞ (cf. Figure 3.2). Such simplification,

however, was found unsatisfactory, since it greatly increases the sensitivity of the results to the size 2A of the computational cell. At the same time, the numerical factor S_c in equation (3.13) is unimportant and can be conveniently replaced, for example, by S_∞ without any appreciable effect on the solution for $A \gg a$ (since the only purpose of this term is to make the solution flux-free and, hence, unique).

Except for extreme cases (see below), the solution of (3.13)-(3.14) is successfully found by minimal-residual iterations (GMRES(k)) with k = 2-4, the same version as used in emulsion flow simulations[31]). Adding terms to (3.13)-(3.14) for full deflation, we have attempted simple iterations, but those were uncompetitively slow even for moderately small particle-wall spacings; these terms did not accelerate GMRES either. For a particle in very close contact with a sharp corner, even GMRES was not powerful enough, resulting in thousands of iterations. Alternative, biconjugate-gradient iterations perform much better in these, most-difficult cases and were systematically used in our algorithm, although they make programming far more complex, since the exact adjoint to the discretized form of (3.13)-(3.14) must be also calculated.

Although most of our approach is applicable for an arbitrary-shaped particle, in what follows we assume the spherical shape and the motion of particle center in the $x_3 = 0$ plane only (plane of drawing for Figure 3.1), to simplify surface meshing and make calculations faster. The motion symmetry implies the symmetry in the solution of (3.13)-(3.14):

$$\begin{aligned} &q_1\left(x_1, x_2, -x_3\right) = q_1\left(x_1, x_2, x_3\right) \quad , \quad q_2\left(x_1, x_x, -x_3\right) = q_2\left(x_1, x_2, x_3\right) \quad , \\ &q_3\left(x_1, x_2, -x_3\right) = -q_3\left(x_1, x_2, x_3\right) \quad . \end{aligned} \tag{3.17}$$

To discretize the cell side surface S_∞, we first discretize the entire frame contour $\mathcal{C}$ into a large N_c number of small successive subsegments $\Delta\ell_{1,0,}\Delta\ell_{2,0,\ldots}$ starting from a corner. To better

resolve lubrication between the particle and (possibly close) channel walls, the lengths $\Delta\ell_{i,0}$ are calculated from an adaptive rule

$$\Delta\ell_{ij} = c_{\Delta\ell}\left(\varepsilon_{i,j}\right)^{\alpha} \tag{3.18}$$

with $j = 0$. Here, the parameter $c_{\Delta\ell}$ sets the resolution, ε is the distance from a contour point to the particle surface (particularly easy to calculate for a spherical shape), $\varepsilon_{\mathrm{I},0}$ is the local value of ε at the start point of interval $\Delta\ell_{i,0}$, and α (typically 0.5-0.75) is the adaptivity parameter. For accuracy, it is essential that this discretization fits all corners of the frame contour $\mathcal{C}$. If the end point of the next interval $\Delta\ell_{i+1,0}$ would be outside a line segment $\mathcal{L}_k^{\infty}$, it is not accepted; instead, the whole distribution on $\mathcal{L}_k^{\infty}$ is slightly, and uniformly, scaled about the start point of $\mathcal{L}_k^{\infty}$ to make the end point of $\Delta\ell_{i,0}$ fit the corner, and discretization proceeds to the next line segment $\mathcal{L}_{k+1}^{\infty}$.. In the calculations, $c_{\Delta\ell}$ was chosen to have typically N_c = 200-300 for particle-wall close contact (although good results are often obtained for much smaller N_c).

This moderately adaptive contour discretization (Figure 3.3a) is then extended in the positive x_3-direction to obtain adaptive discretizations of all the rectangular panels $S_1^{\infty}, S_2^{\infty}, \ldots S_M^{\infty}$ (Figure 3.3b). For each line element $\Delta\ell_{i,0}$ of the contour, we successively construct rectangular elements $\Delta\ell_{i,0}\times\Delta\ell_{i,1}$, $\Delta\ell_{i,0}\times\Delta\ell_{i,2}$, etc., with the lengths $\Delta\ell_{i,0}$ and $\Delta\ell_{i,j}\,(j\geq 1)$ along the contour and in the x_3-direction, respectively. The lengths $\Delta\ell_{i,j}\,(j\geq 1)$ are calculated from (3.18), where $\varepsilon_{i,j}$ is now the 3D distance from the midpoint of the "top" (already constructed) edge of the element $\Delta\ell_{i,0}\times\Delta\ell_{i,j}$ to the particle surface. Again, it is easy to exactly fit the bottom edges of the rectangular elements to the $x_3 = A$ boundary of the panels by slight rescaling in the x_3-direction. Although not a "mesh" in the usual sense (Figure 3.3b), the result is an adaptive,

boundary-fitted coverage of the $x_3 \geq 0$ half of each panel $S_1^\infty, \ldots S_N^\infty$ by a number of rectangular elements controlled by $c_{\Delta\ell}$ and α only; each vertical strip in Figure 3.3b has, in general, its own number of elements. This coverage can be extended to the other half of each panel by symmetry. Midpoints of the rectangular elements on all panels serve to collocate the integral equations (3.13)-(3.14) and calculate all the integrals over S_∞ (after regularizations when necessary, see below) with second-order accuracy in the simplest manner. The grid step along the contour may be too small without necessity in some areas away from lubrication (Figure 3.3b), but this drawback of our simple gridding algorithm appears minor and did not cause any difficulties.

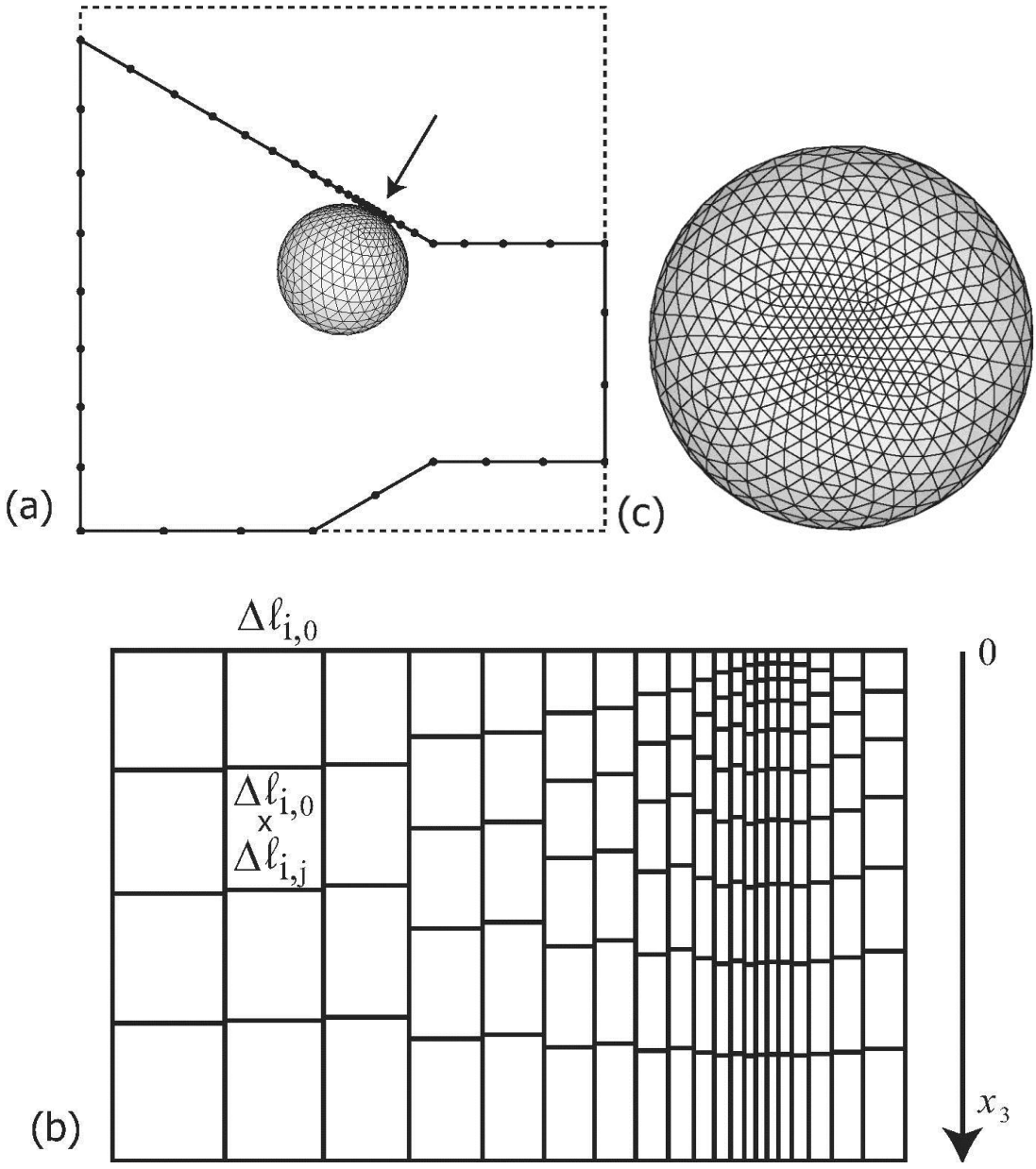

Figure 3.3 Gap-adaptive surface discretizations in the 3D algorithm: (a) discretization of the frame contour and the sphere triangulation (side view, along the x_3-axis); (b) for the panel denoted by the arrow in (a), the contour discretization is extended to the entire $x_3 > 0$ half of the panel; (c) view of the sphere triangulation along the direction denoted by arrow in (a). In calculations, much higher resolutions and larger computational cells around the particle are typically used.

The particle surface S_p is discretized by an unstructured mesh of N_Δ triangular elements, with N_Δ typically being several thousand. Initial, highly-uniform triangulation is prepared from a regular icosaedron[34] or dodecaedron[42] by a series of refinements,[34,42,43] which includes the possibilities N_Δ = 1280, 1500, 2160, 2880, 3840, 5120, 6000, 8640, etc. The number N_Δ of elements may vary slightly during the simulation (Appendix). Our algorithm includes optional mesh adaptivity on the sphere to particle-channel surface clearance to increase resolution in lubrication areas. This is achieved, at each configuration, by redistributing mesh nodes on S_p to minimize the mesh "potential energy." The energy form, although specific for the present problem, was inspired by earlier boundary-integral work on deformable drops;[44,32] in particular, a part of the energy designed to prevent mesh-triangle collapse[32] drastically improves mesh quality and allows us to avoid topological mesh transformations, resulting in a simple algorithm. Details are given in the Appendix. Figures 3.3a and 3.3c show an example of moderately-adaptive meshing with N_Δ = 1280. This adaptivity greatly improves accuracy of the normal velocity for the particle in close contact with a smooth part of the channel, away from sharp corners, so adaptive triangulations are preferred when accurate temporal dynamics of such interactions are of most interest. On the contrary, for very close particle-corner interactions, the mesh adaptivity on S_p was found to be detrimental, resulting in extremely slow convergence of boundary-integral iterations. In the present applications (Section 3.5), where particle-corner interactions play a major role, non-adaptive surface triangulations were employed. In contrast, mesh adaptivity on the cell boundary S_∞ (see above) was found to be always advantageous.

For a smooth function integration over the particle surface, the second-order trapezoidal rule is the simplest, which can be recast as

$$\int_{S_p} f(\boldsymbol{x})\, dS \approx \sum_i f(\boldsymbol{x}_i)\, \Delta S_i \quad , \tag{3.19}$$

where ΔS_i is one third of the sum of the flat triangle areas sharing the vertex $\boldsymbol{x}_i$, and the summation in (3.19) is over all triangle vertices on S_p. Following Rallison,[45] the economical rule (3.19) was used in much of our prior boundary-integral work with drops and particles (e.g., Zinchenko and Davis[32,46]). In the present calculations, however, we used a slight improvement of this integration rule specific for a spherical surface. Namely, within each spherical mesh triangle Δ, $f(\boldsymbol{x})$ is approximated as a linear function of intrinsic Cartesian variables x', y' in the tangential plane, and the resulting integrals over Δ are calculated exactly by spherical trigonometry. This integration scheme can still be written in the economical form (3.19) with modified ΔS_i. Higher-order integrations were found not advantageous in the present applications.

Leading-order singularity and near-singularity subtractions (similar to those in Loewenberg and Hinch[43] are applied to double-layer boundary-integrals (3.13)-(3.14) over S_p to make them more amenable for numerical calculations by the quadrature (3.19). This approach, based on subtracting from $\boldsymbol{q}(\boldsymbol{x})$ the value of $\boldsymbol{q}(\boldsymbol{x}^*)$ at the mesh node on S_p, which is nearest to the observation point $\boldsymbol{y}$, does not completely eliminate unbounded behavior of the integrand for the particle-wall interaction (cf. Zinchenko and Davis[46]), but it was found to be sufficient. Due to sharp corners in the geometry of the surrounding cell S_∞, though, the contributions of rectangular panels S_1^∞, S_2^∞,… to the integrals (13)-(14) are handled differently and individually:

$$\int_{S_j^\infty} \boldsymbol{q}(\boldsymbol{x})\cdot\boldsymbol{\tau}(\boldsymbol{r})\cdot\boldsymbol{n}(\boldsymbol{x})\,dS_x = \frac{3}{4\pi}\int_{S_j^\infty} \frac{\left\{\left[\boldsymbol{q}(\boldsymbol{x})-\boldsymbol{q}(\boldsymbol{x}^*)\right]\cdot\boldsymbol{r}\right\}\left[\boldsymbol{r}\cdot\boldsymbol{n}(\boldsymbol{x})\right]\boldsymbol{r}}{r^5}\,dS_{\boldsymbol{x}} + \frac{3}{4\pi}\boldsymbol{q}(\boldsymbol{x}^*)\cdot\int_{S_j^\infty}\frac{\left[\boldsymbol{r}\cdot\boldsymbol{n}(\boldsymbol{x})\right]\boldsymbol{r}\boldsymbol{r}}{r^5}\,dS_{\boldsymbol{x}} \quad , \tag{3.20}$$

where $\boldsymbol{x}^* = \boldsymbol{x}^*(\boldsymbol{y},j)$ is the collocation node on the rectangular panel S_j^∞ that is closest to the observation point $\boldsymbol{y}$. Similar to the 2D solution (cf. equation (3.8)), the panel containing $\boldsymbol{y}$ does not contribute to (3.20). The first integral in the RHS of (3.20) is handled numerically on the mesh of rectangles (Figure 3.3b); the added-back term allows for analytical treatment (Appendix), based on the contour integration technique from Bazhlekov *et al.*[47]

Finally, several beneficial features of our 3D boundary-integral solution for a particle in a complex-shape channel merit additional discussion. The neglect of contributions from the top (S_{top}) and bottom (S_{bottom}) portions of the cell boundary serve versatility of the method, making it suitable for *any* planar channel with a profile consisting of straight line segments. Otherwise, the task of meshing S_{top} and S_{bottom} could be unwieldy. Second, the flow representation (3.9), where the 2D solution $\boldsymbol{u}_\infty(\boldsymbol{y})$ has been singled out, is beneficial in that $\boldsymbol{u}_\infty(\boldsymbol{y})$ for 3D boundary integral equations (3.13)-(3.14) needs to be calculated on the particle surface only, at a relatively small cost. Thus, much more expensive calculations of $\boldsymbol{u}_\infty(\boldsymbol{y})$ on the cell boundary S_∞, or unwieldy pretabulation of $\boldsymbol{u}_\infty(\boldsymbol{y})$ in the whole flow domain, are avoided altogether. Finally, for rectangular panels S_j^∞, $\boldsymbol{r}\cdot\boldsymbol{n}(\boldsymbol{x})$ is taken out of integrations (3.20), and contributions from both halves x_3 and $x_3 > 0$ of each panel S_j^∞ are combined due to symmetry (3.17), which makes 3D boundary-integral iterations quite fast, even for large problems with high resolution.

The variable time step Δt in dynamical simulations was chosen as

$$\Delta t = c_{\Delta t}\left[h_{\min}\left(h_{\min}+a\right)\right]^{1/2}\Big/|\boldsymbol{U}| \tag{4.21}$$

based on the particle radius a, instantaneous particle-channel surface spacing h_{min}, and particle translational speed $|\boldsymbol{U}|$; the non-dimensional coefficient $c_{\Delta t}$ is the range 0.05-0.2. In an empirical manner, the particle position $\boldsymbol{x}_c$ is advanced from t to $t+\Delta t$ by a fourth-order Runge-Kutta (RK)

step when $h_{min}/a > 0.2$, by a second-order RK step when $0.05 < h_{min}/a < 0.2$, and by the simplest Euler step when $h_{min}/a < 0.05$. The algorithm employs optimal construction of the initial approximation to boundary-integral solution $\boldsymbol{q}(\boldsymbol{x})$ by linear extrapolation from the preceding (fractional) time steps; this element also includes spatial interpolations, because of the variable number of boundary elements on the cell boundary S_∞ and the sphere.

3.3.4 Particle Interaction with a Sharp Corner

The situation when the particle approaches a sharp corner in the microchannel (in Figure 3.1, there are five such corners) requires a special treatment. For a particle near a smooth part of the channel, the rate-of-change of the particle-wall surface clearance, dh_{min}/dt, has a usual scaling $\sim h_{min}$, with strong lubrication. For a particle near a sharp corner, we currently do not see a way to study analytically the scaling for the approach velocity, dh_{min}/dt. Our calculations are reasonably well described by $dh_{min}/dt \sim h_{min}^{1/3}$, although this fit to numerical data was tested in a limited range $0.01a < h_{min} < 0.04a$ of particle-to-corner spacings, and the exponent $p \approx 0.2$-0.3 was found to be slightly sensitive to the mutual orientation of the particle and the corner. In any case, in contrast to particle-wall interactions, a contact with the corner can be reached with little additional hydrodynamic resistance and in a finite time. Since the ultimate approach appears to be with zero velocity, inelastic collision can be assumed, so the particle does not bounce after impact, but rolls instead around the corner until it is separated by the flow. Note that the corner exerts a compressive force on the particle when in contact and that this force is relieved when the particle rolls around the corner to a critical location. Logically, the simplest way to simulate the contact motion is by using the same code, but with a small threshold Δ_c (typically, ~ 0.01). Whenever the particle-to-corner surface spacing h_{min} is less than $a\delta_c$, the transverse velocity $\boldsymbol{U} - (\boldsymbol{U}\cdot\boldsymbol{e})\boldsymbol{e}$ of the particle center, instead of the full velocity $\boldsymbol{U}$, is used in the trajectory integration,

where $\boldsymbol{e} = \boldsymbol{r}_c/|\boldsymbol{r}_c|$ is the unit director of the radius-vector $\boldsymbol{r}_c$ drawn from the corner to the particle center. This kinematic constraint makes h_{min} fluctuate slightly around $a\delta_c$ thus preventing further approach, until the flow separates the particle from the corner, and the simulation is then resumed in a usual manner.

This simple remedy, though, is generally very expensive, since many time steps may be required before the particle is separated by the flow, and, for the particle in apparent contact with a corner, the number of boundary-integral iterations per time step was observed to reach $O(10^2\text{-}10^3)$. If particle *trajectories*, rather than temporal dynamics, are of primary interest, a more economical way is to first interrupt the simulation when an apparent contact with the corner is reached ($h_{min} \approx a\delta_c$). Then, multiple 3D boundary-integral solutions are obtained at $h_{min} = a\delta_c$ and different orientations of the radius-vector $\boldsymbol{r}_c$ to find, by trial-and-error, the critical orientation $\boldsymbol{r}_c^{crit}$, for which $dh_{min}/dt = \boldsymbol{U}\cdot\boldsymbol{r}_c/|r_c| = 0$ and the particle is subsequently separated from the corner by the flow. It usually makes sense to apply this procedure first with the 2D velocity $\boldsymbol{u}_\infty$ (Section 3.3.2) calculated at the particle center (instead of $\boldsymbol{U}$) for a quick rough estimation of the critical orientation $\boldsymbol{r}_c^{crit}$, and then refine the result by 3D boundary-integral solutions. A combination of this initial approximation with the bisection/secant method for finding $\boldsymbol{r}_c^{crit}$ is used as a new initial condition to resume the dynamical simulation, with the particle now separating from the corner. The exact choice of artificial proximity criterion δ_c, when in the range $\leq 0.005\text{-}0.01$, was found to have a negligible effect on global trajectories.

3.4 Numerical Tests

3.4.1 Tests for the 2D Algorithm

The purpose of the tests in this subsection is to demonstrate the validity and accuracy of the simple 2D boundary-integral algorithm from Section 3.3.2 for flows in a channel without a particle, in the presence of sharp corners between the walls.

a. *Flow in a rectangular cavity with a moving wall.* The first example is for the Stokes flow in a rectangular cavity [0,~1.5] × [0,~1] (Figure 3.4). The boundary conditions for the velocity are no-slip $\boldsymbol{u} = \mathbf{0}$, except for the upper wall where $u_1 = 10x_1\,(1.5 - x_1)^2$, $u_2 = 0$. The classical formulation of the cavity problem[48-51] would assume a constant velocity on the top wall, with strong boundary conditions discontinuity. Such discontinuity, however (which may require Kelmanson's[37-38] regularizations for an accurate boundary-integral solution), is not characteristic for flows in microchannels considered herein. So, to avoid complications, we modify the formulation to make $\boldsymbol{u} = \mathbf{0}$ in all corners. A boundary-integral solution was obtained with N = 100 and 400 node points per line segment. An alternative, finite-difference solution was generated on a 400 × 400 mesh, by standard Zeidel iterations in the stream function-vorticity formulation with Woods' boundary condition for the vorticity. For ten random points on the finite-difference mesh (marked 1-10 in Figure 3.4), Table 3.1 shows the velocity components u_1, u_2 from both solutions; excellent agreement between the two methods is observed.

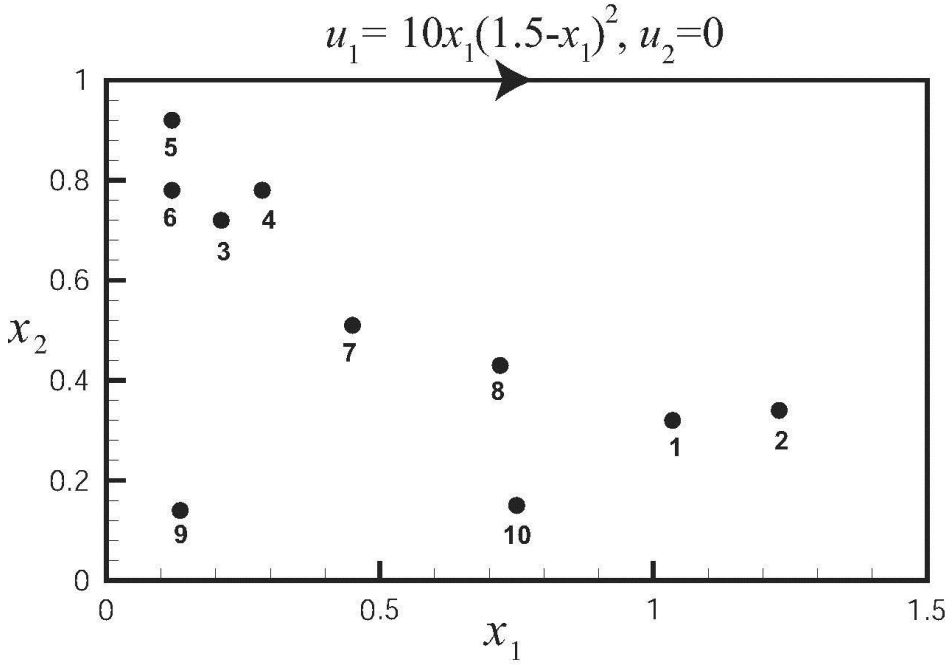

Figure 3.4 A test of the 2D algorithm for the flow in a rectangular cavity with a moving wall.

Point No.	x_1	x_2	BI solution u_1	BI solution u_2	FD solution u_1	FD solution u_2
1	1.035	0.32	–0.6574	–0.3819	–0.6574	–0.3820
2	1.230	0.34	– 0.3018	–0.3972	–0.3018	–0.3972
3	0.210	0.72	–0.3246	1.5100	–0.3244	1.5097
4	0.285	0.78	0.0053	1.2701	0.0056	1.2700
5	0.120	0.92	0.5028	1.0409	0.5036	1.0403
6	0.120	0.78	–0.1479	1.4436	–0.1477	1.4431
7	0.450	0.51	–0.9632	0.6459	–0.9631	0.6459
8	0.720	0.43	–1.0768	–0.1427	–1.0768	–0.1427
9	0.135	0.14	–0.0801	0.0809	–0.0802	0.0809
10	0.750	0.15	–0.7007	–0.0312	–0.7008	–0.0312

Table 3.1 Comparison of the boundary-integral (BI) and finite-difference (FD) solutions for flow in a rectangular cavity with a moving wall.

b. *Flow in a 120° corner between two walls.* An exact solution for the antisymmetric Stokes flow in a sharp corner of infinite extent between two solid plane walls meeting at an angle 2α is described by the stream function[52,53]

$$\psi = r^{\lambda}\left(A\cos\lambda\theta + C\cos(\lambda-2)\theta\right) \quad . \tag{3.22}$$

In (3.22), r and θ are polar coordinates ($x_1 = r\cos\theta$, $x_2 = r\sin\theta$), with the origin in the corner and $\theta = 0$ along the angle bisector. The constants A and C are constrained by

$$A\cos\lambda\alpha + C\cos(\lambda-2)\alpha = 0 \quad . \tag{3.23}$$

The eigenvalue λ is real for $2\alpha > 146°$ and complex otherwise; in the latter case, the real part of (22) must be taken. In particular, extending the calculations of Dean and Montagnon[52] and Moffatt[53], one obtains the first eigenvalue $\lambda = 3.09414+0.60459i$ for $2\alpha = 120°$. We used the exact solution (3.22) (with $C = 1$) to provide the boundary conditions for the velocity $\boldsymbol{u}$ on the perimeter of a triangular domain (with sides 1.3 and 1.8 along the corner, Figure 3.5) and then applied our 2D algorithm (with 300-600 nodes on the boundary segments) to restore $\boldsymbol{u}$ in the interior. For 13 randomly-chosen points in the domain (Figure 3.5), Table 3.2 presents a comparison between the numerical and exact values; the agreement is excellent.

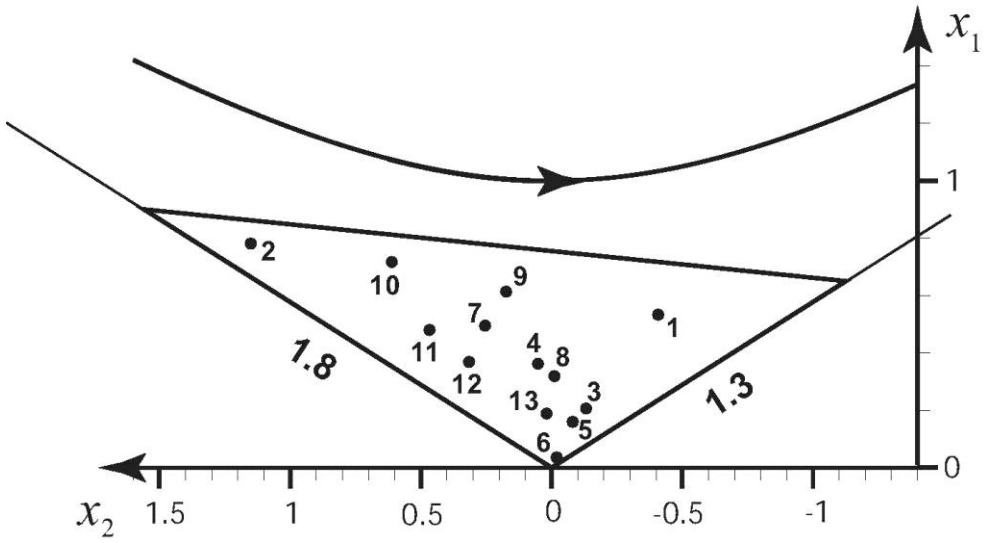

Figure 3.5 A test of the 2D algorithm for the flow in a 120° corner.

			BI solution		Exact solution	
Point No.	x_i	x_2	u_1	u_2	u_1	u_2
1	0.5333	–0.4078	0.2542	–0.9184	0.2542	–0.9184
2	0.7808	1.1504	–0.4290	–0.8315	–0.4291	–0.8319
3	0.2063	–0.1321	0.0103	–0.0695	0.0103	–0.0695
4	0.3622	0.0520	–0.0187	–0.4165	–0.0188	–0.4165
5	0.1597	–0.0809	0.0015	–0.0296	0.0015	–0.0296
6	0.0358	–0.0197	–0.0007	0.0023	–0.0007	0.0023
7	0.4950	0.2541	–0.1562	–0.8565	–0.1562	–0.8566
8	0.3191	–0.0107	0.0030	–0.2979	0.0029	–0.2979
9	0.6135	0.1736	–0.1615	–1.5303	–0.1615	–1.5303
10	0.7167	0.6110	–0.5668	–1.7618	–0.5668	–1.7618
11	0.4800	0.4669	–0.2098	–0.6088	–0.2098	–0.6088
12	0.3685	0.3156	–0.0965	–0.3358	–0.0965	–0.3358
13	0.1887	0.0191	–0.0009	–0.0604	–0.0009	–0.0604

Table 3.2 Comparison of the boundary integral (BI) and exact solutions for the flow in a 120° corner between two walls.

c. *Flow around the rectangular wedge.* For $2\alpha = 270°$, the exponent in (3.22) is $\lambda = 1.54448$. The stream function (3.22) was used again to calculate the boundary values of the velocity $\boldsymbol{u}$ on the perimeter of the computational domain (marked bold in Figure 3.6), and the 2D boundary integral algorithm was then employed to restore $\boldsymbol{u}$ in the interior. For all test points from Figure 3.6, Table 3.3 demonstrates very close agreement between the numerical and exact values.

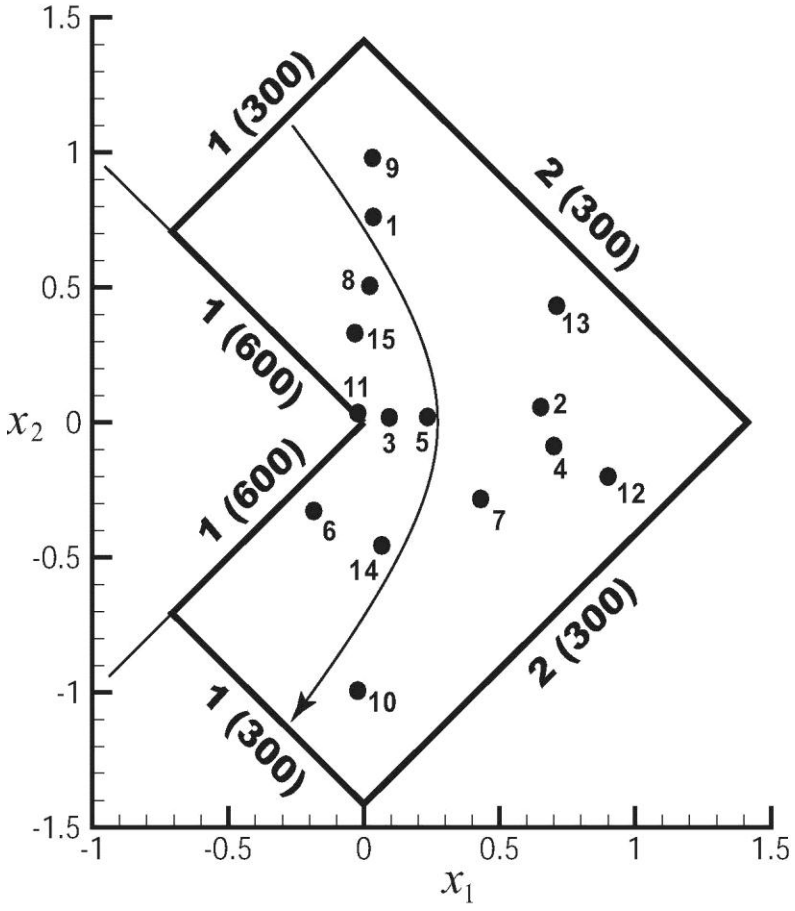

Figure 3.6 A test of the 2D algorithm for the flow around a rectangular wedge. For each boundary segment, the length and the number of mesh nodes (in parentheses) are given.

			BI solution		Exact solution	
Point No.	x_1	x_2	u_1	u_2	u_1	u_2
1	0.0347	0.7611	0.4766	–0.7858	0.4767	–0.7858
2	0.6518	0.0567	0.0605	–1.8863	0.0605	–1.8866
3	0.0938	0.0185	0.0471	–0.6553	0.0472	–0.6548
4	0.7000	–0.0875	–0.0900	–1.9598	–0.0900	–1.9600
5	0.2347	0.0200	0.0340	–1.0819	0.0340	–1.0819
6	–0.1843	–0.3279	–0.1209	–0.1390	–0.1209	–0.1390
7	0.4305	–0.2835	–0.3194	–1.4690	–0.3196	–1.4691
8	0.0220	0.5061	0.3810	–0.6273	0.3811	0.6272
9	0.0318	0.9798	0.5412	–0.8836	0.5413	–0.8836
10	–0.0225	–0.9937	–0.5202	–0.8158	–0.5202	–0.8158
11	–0.0220	0.0346	0.0293	–0.0327	0.0291	–0.0324
12	0.9001	–0.2005	–0.1817	–2.2415	–0.1818	–2.2416
13	0.7106	0.4323	0.3944	–1.9348	0.3945	–1.9349
14	0.0660	–0.4555	–0.3861	–0.6865	–0.3862	–0.6864
15	–0.0327	0.3306	0.2650	–0.3942	–0.2650	–0.3939

Table 3.3 Comparison of the boundary integral (BI) and exact solutions for flow around a rectangular wedge.

a. *Sphere in a Poiseuille flow between parallel walls.* As the first test of the 3D boundary-integral algorithm described in Section 3.3.3, consider a spherical particle of radius a freely suspended in a Poiseuille flow between two parallel plane walls (Figure 3.7a). The numerical solution for this problem was first obtained by Ganatos *et al.*[4] using a collocation method, although the results could only be obtained for a particle away from the walls ($h/a \geq 0.1$, where h is the surface spacing to the nearest wall). An alternative, boundary-integral solution of Staben *et al.*[3] has extended the range of parameters to near-contact with the walls ($h/a \geq 0.005$) and also incorporated ellipsoidal particle shapes.

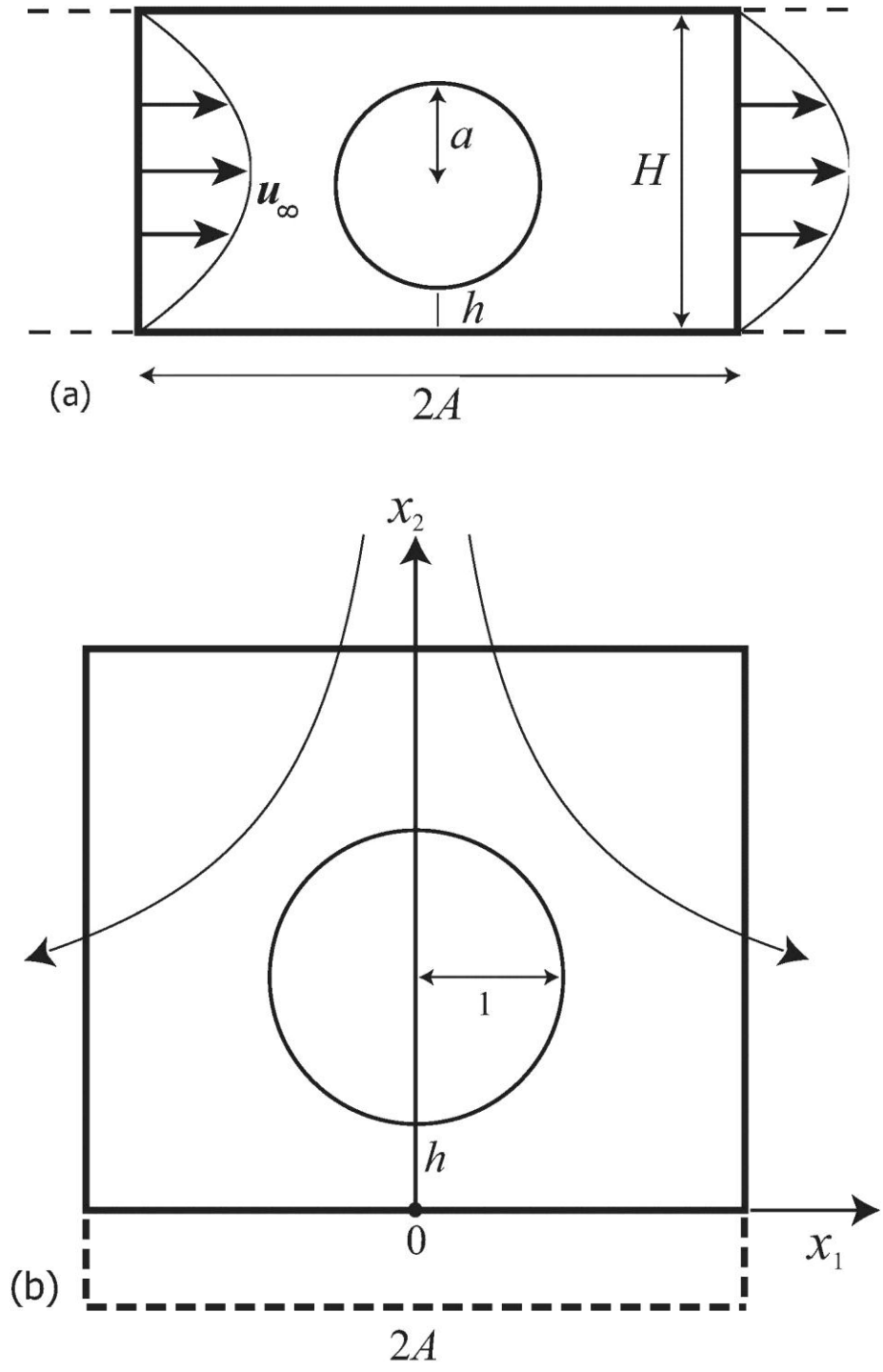

Figure 3.7 Tests for the 3D algorithm: (a) sphere in a Poiseuille flow between two parallel walls; (b) sphere in an unbounded planar quadratic flow near a plane wall.

3.4.2 Tests for the 3D Algorithm

The present approach to this problem requires discretization for both the particle surface and the surrounding computational cell boundary (marked bold in Figure 3.7a); the results depend on the width $2A$ of the cell, unless $A/a \to \infty$. In contrast, the solution of Staben et al.[3] which employs the Green function for the domain between two parallel walls,[54] does not contain such a parameter and requires discretization of the particle surface only. Both algorithms use unstructured sphere triangulations adaptive to particle-wall spacing, although the approach in Staben *et al.*[3] specific for the geometry in Figure 3.7a, is vastly different.

The present 3D algorithm of Section 3.3.3 was applied for a channel of unit width $H = 1$, at two values of the tightness parameter $\eta = 2a/H = 0.6$ and 0.9. The sphere triangulations were constructed as described in the Appendix, with the adaptivity exponent $\gamma = 1$; the parameter $c_\Delta =$ 2000 and 750 for $\eta = 0.6$ and 0.9, respectively. Adaptive cell boundary discretizations were made with the exponent $\alpha = 0.75$ in equation (3.20); $c_{\Delta\ell} = 0.138$ and 0.170 for $\eta = 0.6$ and 0.9, respectively. For each value of the relative surface clearance, h/a, Table 3.4 presents the translational particle velocity U scaled with the centerline velocity U_c of the Poiseuille flow; the number N_c of discretization line segments on the cell contour $\mathcal{C}$, and the number N_Δ of triangular elements on the sphere are given in parentheses. The total number of collocation nodes on all the surfaces varies from 5K (for $h/a = 1.1$) to 9K-12K (for $h/a = 1.005$). For comparison, Table 3.4 also presents the values of U/U_c from Staben *et al.*[3] at $N_\Delta = 8640$; the results for U/U_c at $N_\Delta =$ 3840 are given in parentheses. Excellent agreement between the two solutions is observed to h/a = 0.005.

	Present Solution		Staben *et al.*[3]	
h/a	$2a/H = 0.6$	$2a/H = 0.9$	$2a/H = 0.6$	$2a/H = 0.9$
0.005	0.424 (199, 8640)	0.496 (197, 8640)	0.423 (0.427)	0.492 (0.498)
0.007	0.437 (187, 8650)	0.504 (188, 8640)	0.436 (0.439)	0.505 (0.508)
0.01	0.455 (175, 8640)	0.521 (177, 8640)	0.455 (0.458)	0.521 (0.525)
0.02	0.499 (155, 6000)	0.559 (159, 6000)	0.499 (0.499)	0.559 (0.559)
0.04	0.554 (138, 6000)	0.600 (146, 6000)	0.553 (0.553)	0.559 (0.599)
0.07	0.607 (127, 5120)	0.629 (138, 5120)	0.606 (0.606)	0.629 (0.629)
0.1	0.647 (121, 5120)	0.641 (135, 5120)	0.646 (0.646)	0.640 (06.40)

Table 3.4 Non-dimensional translational velocities U/U_c for a sphere freely suspended in a Poiseuille flow between two parallel plane walls. For the present solution, the data in parenthesis are discretization parameters. For the solution of Staben *et al.*, the data in parentheses are U/U_c for cruder triangulation.

For the present solution at $\eta = 0.6$, the effects of the cell size, sphere discretization, and cell boundary discretization on the results were studied separately. Increasing A to $15a$ raises the values of U/U_c in Table 3.4 by 0.2-0.3%. The effects of the sphere and the cell boundary discretization are not appreciable for $h/a \geq 0.02$; at $h/a = 0.005$, they can reach ± 0.6-0.7%, but partially compensate each other. As in Staben *et al.*[3] (Table 3.4 therein), the convergence is slower for the rotational particle velocity Ω, especially in near-contact, but a good agreement is still observed between the two solutions. For example, at $\eta = 0.6$, the present values of $H\Omega/U_c$ are 0.525, 0.548 and 0.566 for $h/a = 0.01$, 0.02 and 0.04, respectively, compared to 0.521, 0.550 and 0.568 from Staben *et al.*[3] Rotational velocities are of less interest in the present study, since they do not affect the particle trajectories.

The effect of the particle mesh adaptation (see Appendix) on the results by the present algorithm in Table 3.4 was also tested. With non-adaptive meshes and the same N_Δ, the results are identical to those in Table 3.4 when $h/a \geq 0.04$, both for $\eta = 0.6$ and 0.9. At $h/a = 0.01$, the effect is less than 2%, but grows to 2.4% for smaller gaps.

b. *Sphere in a planar quadratic flow near a plane wall.* In the second test (Figure 3.7b), a sphere of unit radius is freely suspended in a planar quadratic Stokes flow $\boldsymbol{u}_\infty = (2x_1x_2 - x_2^2,\ 0)$ near a plane wall $x_2 = 0$. The x_1-axis is along the wall, and the sphere is centered at $x_1 = 0$, $x_2 = 1 + h$, $x_3 = 0$ (Figure 3.7b). The purpose of this test, more demanding than the previous test for Poiseuille flow, is to verify how accurately the present algorithm can describe the normal particle motion, strongly hampered by lubrication, in near contact. The 2D projection of the computational cell is obtained by intersecting the domain $x_2 > 0$ and the square, with sides 2A and centered with the particle; the cell boundary is marked bold in Figure 3.7b. The present solution was obtained for $A = 15$, using adaptive meshes on the sphere and the cell boundary

with $c_\Delta = 200$, $\gamma = 1$, $c_{\Delta\ell} = 0.0976$, $\alpha = 0.75$. For different values of the surface clearance, Table 3.5 shows the particle approach velocity, alongside with the number N_c of discretization line segments on the cell contour $\mathcal{C}$, and the number N_Δ of triangular elements on the sphere (in parentheses). The total number of collocation nodes on all the surfaces varies from 13K (for h = 0.1) to 34K (for h = 0.005).

h	Present Algorithm	Domain Green Function BI
0.005	0.0178 (398, 8640)	0.0161
0.007	0.0239 (375, 8640)	0.0225
0.010	0.0328 (352, 8640)	0.0320
0.02	0.0641 (314, 8640)	0.0637
0.04	0.1267 (282, 6000)	0.1264
0.07	0.2198 (259, 5120)	0.2195
0.1	0.3124 (246, 5120)	0.3120

Table 3.5 Approach velocities for a sphere freely suspended in a planar quadratic flow near a plane wall. For the present algorithm, the data in parentheses are discretization parameters.

An alternative solution, not employing a computational cell, was obtained by modification/simplification of the boundary-integral code from Staben *et al.*[3] In addition to the change in $\boldsymbol{u}_\infty$, the half-space Green function[55,56] with the corresponding stresslet[33] was used in the boundary-integral formulation, instead of the more complex form of Liron and Mochon.[54] Adaptive sphere triangulations were generated by a one-wall version of the algorithm from Staben *et al.*[3] The right side of Table 3.5 shows the approach velocities from this alternative solution ("Domain Green function boundary integral") at N_Δ = 15360; these results are fully converged, except at the smallest separation h = 0.005 (when coarsening N_Δ to 8640 yields 0.0164). The agreement between the two solutions is acceptable to h = 0.005, and excellent for $h \geq 0.02$. A cruder cell-boundary discretization ($c_{\Delta\ell} = 0.13$) in the present algorithm reduced the total number of collocation nodes by 1.5-1.7 fold, with no appreciable effect on the particle velocities in Table 3.5 for $h \geq 0.01$; at h = 0.007 and 0.005, however, such an approximation becomes inaccurate.

We have also studied the effect of the particle mesh adaptation on the results in Table 3.5. When the non-adaptive particle mesh is used, the results by the present algorithm change to 0.2199, 0.1290, 0.0712 and 0.0365 for h/a = 0.07, 0.04, 0.02 and 0.01, respectively. Even though the error in the normal velocity calculation is noticeable for $h/a \sim 0.01$, it was inconsequential for simulations reported in the next section.

3.5 Numerical Results

3.5.1 Applications to Pinched-flow Fractionation

In the experimental work of Nakashima *et al.*[10] pinched-flow fractionation (PFF) was demonstrated as an efficient, practical way to achieve accurate particle sizing and separation using fluid focusing and spreading in a microchannel. The device consists of two input sleeves

that meet to form a straight pinch area, followed by an expansion area and outlet (Figure 3.8). One of the input sleeves (the upper one in Figure 3.8) contains a dilute mixture of polydisperse, neutrally-buoyant particles, while the other input sleeve is fed by a pure liquid. The higher volumetric flow rate from the inlet section with pure liquid causes the particles to be pushed close to one wall in the pinch area. The particles then effectively separate by the spreading streamlines in the expansion area according to their sizes.

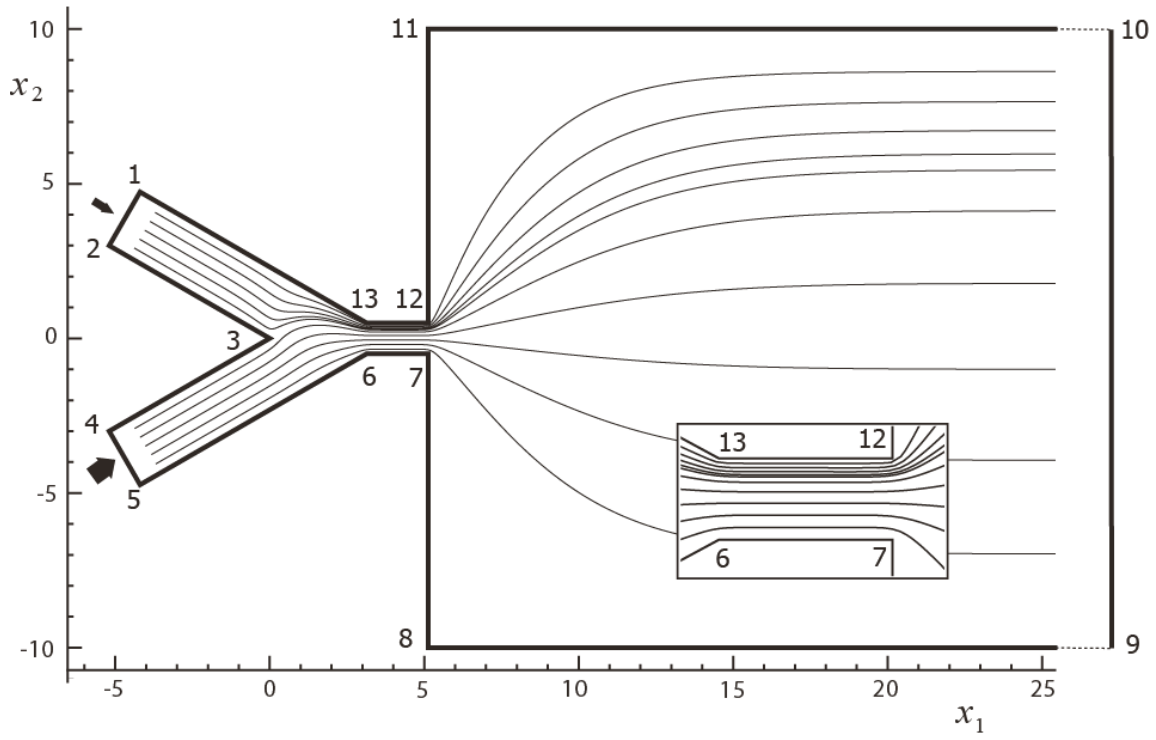

Figure 3.8 Pure liquid streamlines in the pinched-flow fractionation device for flow ratio of Q = 6. The inset is the close-up of the pinch area.

If the inertia, particle-particle interactions, and the effect of the third channel dimension can be neglected, the present moving-frame boundary-integral method is ideally suited to study the PFF phenomenon. The channel geometry in Figure 3.8 has been made non-dimensional using the pinch area width, H, as the length scale. The coordinates (x_1, x_2) of the channel vertices 1-13 are listed in Table 3.6, with x_1 and x_2 being the horizontal and vertical axes, respectively. The outlet section, formed by vertices 9 and 10, is farther downstream than shown in Figure 3.8, extending to $x_1 = 34$. The channel shape in Figure 3.8 is close to device geometries in the experiments of Nakashima *et al.*[10] Besides the non-dimensional particle size $\eta = 2a/H$, the ratio Q of flow rates in the lower and upper input sections and the angle between the pinched area and the broadening section are known to have significant effects on PFF.[10] However, within the limited scope of the present paper, we only demonstrate the effect of the particle size for one geometry in Figure 3.8 with $Q = 6$, leaving a systematic study of PFF for future work.

Vertex No.	x_1	x_2	No.	x_1	x_2
1	–4.196	4.732	8	5.134	–10.000
2	–5.196	3.000	9	34.000	–10.000
3	0.000	0.000	10	34.000	10.000
4	–5.196	–3.000	11	5.134	10.000
5	–4.196	–4.732	12	5.134	0.500
6	3.134	–0.500	13	3.134	0.500
7	5.134	–0.500			

Table 3.6 Coordinates of the channel vertices for the pinched-flow fractionation device shown in Figure 3.8.

The pure-liquid streamlines in Figure 3.8 were calculated by the 2D algorithm of Section 3.3.2 using Poiseuille flow for inlet and outlet boundary conditions. For a small but finite particle size $\eta = 0.3$, the particle trajectories are presented in Figure 3.9a,b. All the trajectories start close to the inlet segment 1-2 and are almost parallel to the sides 2-3 and 1-13 of the inlet sleeve far upstream, and so the initial locations are conveniently characterized by the parameter $p_0 = (d_0 - a)/(H_1 - 2a) \in (0,1)$, where d_0 is the initial distance from the particle center to the lower side 2-3 of the input sleeve, and H_1 is the width of the inlet section 1-2. Trajectories A and B with $p_0 = 0.15$ and 0.30, respectively, proceed to the outlet without reaching the channel walls. The critical trajectory C, with $p_0 = 0.622$, is of special significance. For this trajectory, the particle touches the wedge (vertex 12 in Figure 3.9a) of the device before proceeding to the outlet. To calculate this trajectory, we first determine the critical angle $\theta_{crit} = -67.5°$ between the positive x_1-axis and the radius-vector $\boldsymbol{r}_c$ from the wedge to the particle center, with $\boldsymbol{U} \cdot \boldsymbol{r}_c = 0$, by trial and error (Section 3.3.4). In this procedure, an artificial gap of $h_{min} = 0.005a$ between the particle surface and the wedge was sufficient to avoid numerical difficulties and still provide global accuracy. Backward and forward integrations from this critical position are then used to calculate the two portions of the critical trajectory C.

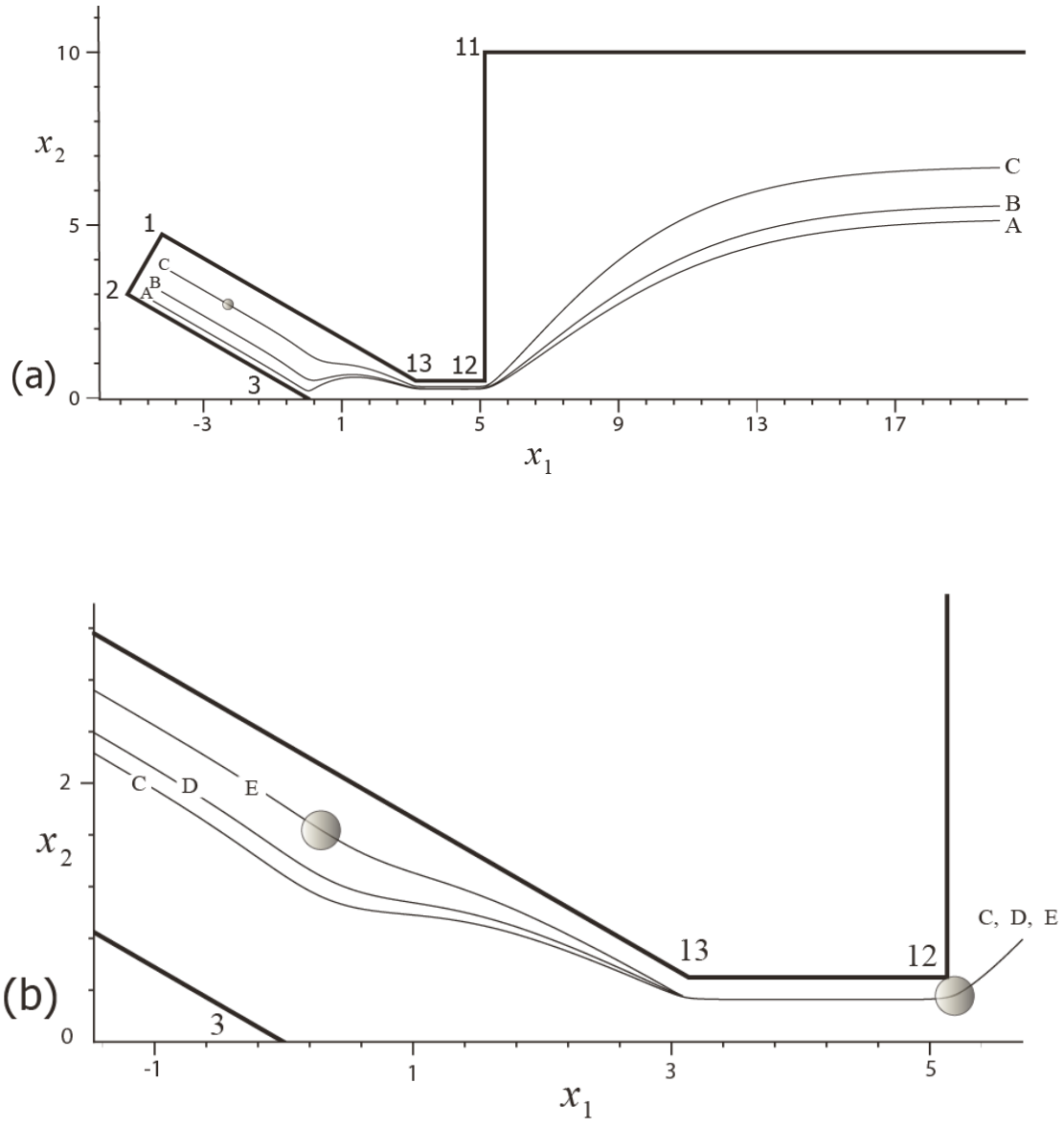

Figure 3.9 (a,b) Trajectories of the particle center in the pinched-flow fractionation device for the particle size $\eta = 0.3$ (shown as the grey circles); (b) is the close-up of the pinch area. Only the $x_2 > 0$ part of the channel is shown; for details, see the text. The grey particle in contact with vertex 12 is at the critical angle when it just begins to separate from the corner.

The close-up of the pinch area near the upper wall (Figure 3.9b) helps to complete classification of the particle trajectories for $\eta = 0.3$. For the critical trajectory D, with $p_0 = 0.702$, the particle touches the first corner (vertex 13) at the critical orientation of the radius vector $\mathbf{r}_c$ from the corner to particle center ($\theta_{crit} = -101.7°$), then separates from the corner, reaches a maximum spacing of $h = 0.07a$ from the upper wall, approaches the wall again and eventually hits the wedge (vertex 12). It must be assumed that the particle will then roll around the wedge and separate at the critical orientation ($\theta_{crit} = -67.5°$) of the $\mathbf{r}_c$-vector, making further motion identical to that from trajectory C. For all intermediate initial conditions between C and D ($0.622 < p_o < 0.702$), the particle misses the first corner but hits the wedge. Finally, for the trajectories initially above D ($p_o > 0.702$), the particle makes contact with the first corner, and then rolls around the corner until separation; further motion is the same as for trajectory D. Numerical difficulties, however, appear in this range. For the sample trajectory E with $p_o = 0.85$, the particle spacing h from the upper wall of the inlet sleeve reaches small values of $h \sim 0.01a$, although the surface clearance from the corner is still $0.08a$ (despite the fact that lubrication prohibits perfect contact with the wall). Without improvements to the algorithm, it would be prohibitively expensive to accurately continue simulations to such small particle-wall spacing; moreover, surface roughness (and possibly colloidal interactions) would need to be included, to make such simulations physically relevant. This indeterminancy, however, would only affect temporal dynamics after the particle has come into "contact" with the wall, and not the global trajectories of interest in the present analysis of PFF.

The results in Figures 3.9a,b and additional calculations yield the vertical position of the particle center in the outlet, $(x_2)_{exit}$, as a function of the initial location parameter p_0; in particular, $(x_2)_{exit}$ becomes independent of the initial location, when $p_0 > 0.622$. In practice, the initial

particle position in the inlet can be arbitrary, and it is best to average the results assuming equal probability of all values $p_0 \in (0,1)$. In this manner, we obtain $< (x_2)_{exit} > = 6.1$ for $\eta = 0.3$.

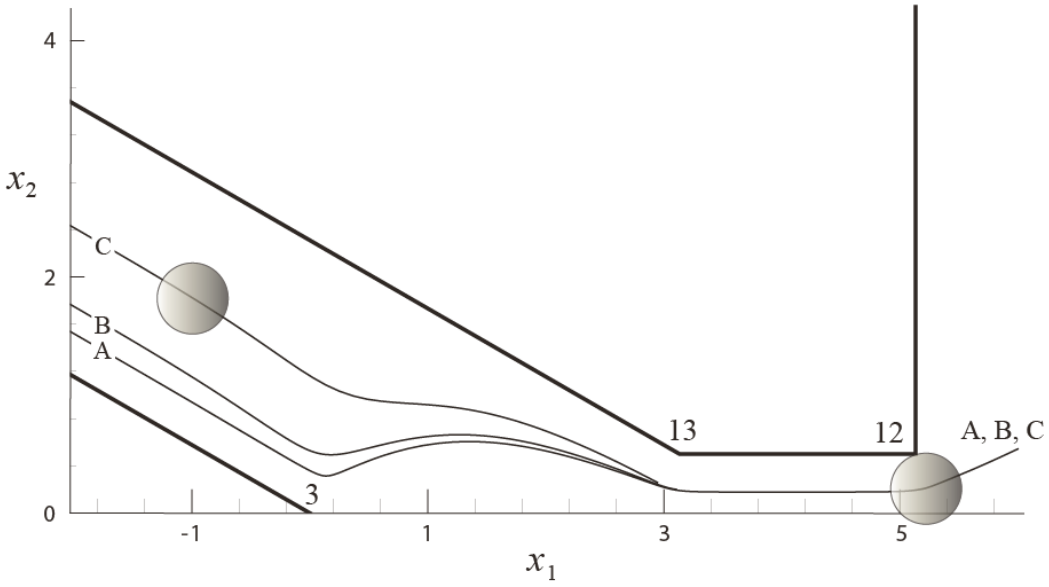

Figure 3.10 Trajectories of the particle center in the pinched-flow fractionation device for the particle size $\eta = 0.6$ (shown as the grey circle). The particle in contact with vertex 12 is at the critical angle when it just begins to separate from the corner. Only the close-up of the pinch area in the $x_3 > 0$ half of the channel is shown; for details, see the text.

The structure of particle trajectories is much different for the larger size, η = 0.6 (Figure 3.10). For trajectory A, the particle starts far upstream in near-contact with the lower wall of the inlet sleeve (the surface clearance being 0.01a), misses the lower corner (vertex 3) and the next corner (vertex 13) but eventually hits the wedge (vertex 12). In subsequent motion, the particle rolls around the wedge and separates at the critical angle θ_{crit} = -74.9° of the $\boldsymbol{r}_c$-vector, before proceeding to the outlet. A backward integration from this critical position (not shown in Figure 3.10) would result in the particle hitting the lower corner, with the $\boldsymbol{r}_c$-vector in the upper half-space ($x_2 > 0$). In this range, there are no critical orientations for the particle in contact with the lower corner, which means that, for *any* initial conditions in the input section, the particle will miss the lower corner but cannot miss the wedge. For the critical trajectory B, with p_0 = 0.130, the particle touches the upper corner (vertex 13) at the critical angle θ_{crit} = -101° of $\boldsymbol{r}_c$. Subsequently, the particle separates from the corner and the upper wall (while remaining in near contact), approaches the wall again and hits the wedge; the final outcome, after rolling around the wedge and separation, is the same as for trajectory A. For trajectories in the narrow range $p_0 < 0.13$, initially below B, the particle misses the upper corner. There is little difference between all such trajectories in the pinch area, because the flow from the lower inlet pushes all particles close to the top wall of the pinch; the maximum particle-wall spacing is 0.073a and 0.048a for trajectories A and B, respectively, and this difference is no more than the trajectory of line width in the figure. Again, for the trajectories initially above B ($p_0 > 0.130$), the particle is observed to approach near-contact with the wall slightly before reaching the corner. For the sample trajectory C, with p_0 = 0.56, we had to stop calculations at the surface clearance of 0.01a.

Unlike for η = 0.3, motion of large particles (η = 0.6) is fully focused in the sense that the outlet vertical position, $(x_2)_{exit}$, is independent of the initial location in the inlet section, because

all particles of this larger size are pushed by the flow up against the top wall and come into contact with the corner (vertex 12). There is a critical value of η_{crit}, between 0.3 and 0.6, with this property, but it was not determined within the limited scope of the present paper. At least, to predict the final outcome of the particle motion for all $\eta \geq 0.6$, it is sufficient to integrate forward from the critical particle orientation in (near) contact with the wedge. The results for η = 0.6, 0.75 and 0.85 are presented in Figure 3.11; the critical θ-angles of vector $\mathbf{r}_c$ with the positive direction of the *x*-axis are –74.6°, –81.2° and –81.8° for η = 0.6, 0.75 and 0.85, respectively. For comparison, the vertical bar shows the range of possible positions of the particle center in the outlet for η = 0.3; the circle is the result averaged over all initial conditions (see above). As follows from Figure 3.11, the particles separate in the outlet according to their sizes, thus demonstrating the efficiency of pinched-flow fractionation. Interestingly, the outlet positions for larger particles ($\eta \geq 0.6$) are considerably lower than the *lowest* possible position for a smaller particle with η = 0.3 (Figure 3.11), and so there is no overlap or mixing of particles of these sizes in the outlet.

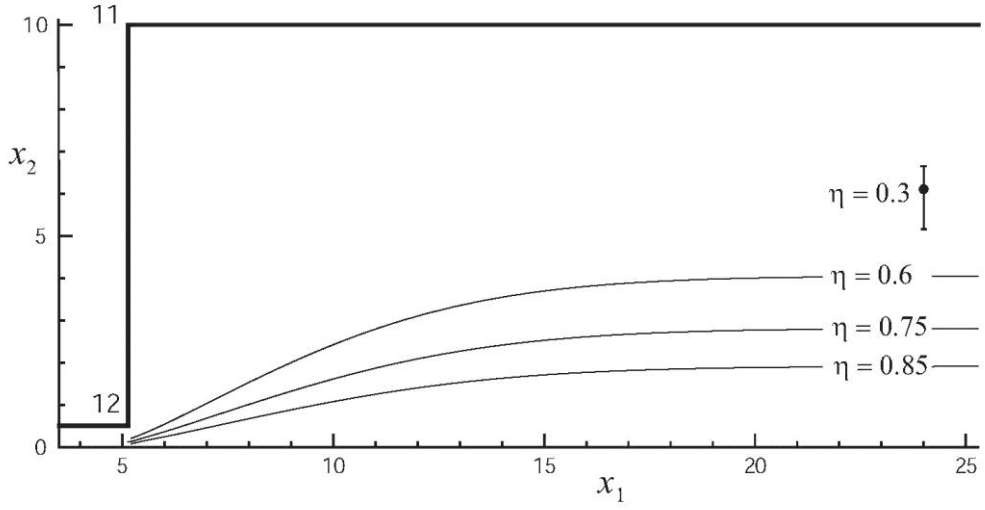

Figure 3.11 Trajectories of the particle center in the broadening section of the pinched-flow fractionation device for the dimensionless particle size η from 0.6 to 0.85. For η = 0.3, when the outlet position is partially dependent on the initial conditions, the whole range is shown by the vertical bar; the circle is the average result for all initial conditions assuming that the suspension is "well-mixed" in the inlet.

Our simulations and additional analysis (to be published separately) confirm all qualitative features of PFF observed in the experiments of Nakashima *et al.*[10] Quantitatively, however, their work shows stronger particle separation than in our simulations. For $\eta \approx 0.3$ and 0.6, the displacement of the particle center from the channel axis of symmetry far downstream is, respectively, 75% and 20% of the outlet halfwidth, according to Figure 3 of Nakashima *et al.*[10] Our simulations predict 61% and 41% for $\eta = 0.3$ and 0.6, respectively. There may be several reasons for these deviations. First, limited resolution of experimental photos in Nakashima *et al.*[10] did not allow us to reproduce their geometry precisely in our simulations; there are also uncertainties about the values of η and the sharpness of corners in their device. Probably most important, the microchannels in Nakashima *et al.*[10] have finite depth comparable with the particle diameter; this depth is assumed to be infinite in the present work. The fluid viscosity is not reported in Nakashima *et al.*[10] except that it is said to be "relatively high;" still, some inertial effects on the behavior of larger particles ($\eta = 0.6$) could be present in the experiments.[10] The microfluidic devices currently being fabricated in our research group are much closer to the assumptions of the present work; they have sharp corners and much larger depth.

In our calculations for Figure 3.11, half-size $A = 10a$ of the computational cell was used; the resolution parameters $c_{\Delta\ell}$ and c_Δ (Section 3.2.3 and Appendix) were such that each trajectory in Figure 3.11 starts with $N_c \approx 200$ points on the frame contour and $N_\Delta = 6000$ triangular elements on the sphere. A broad variation of the program parameters A, $c_{\Delta\ell}$ and c_Δ for $\eta = 0.6$ indicates < 1% error in the calculated downstream position x_2 of the particle center.

A simple analysis of pure liquid streamlines (Figure 3.8) does not describe the particle focusing phenomenon; for streamlines, the outlet position always depends on the initial conditions in the inlet. Nevertheless, it is interesting to explore if our results for $\eta \geq 0.6$ in Figure 3.11 could be

reproduced by a simplified theory based on streamlines only, partially taking the particle size into account and *assuming* particle focusing after its interaction with the wedge. To this end, the critical orientation angle of the particle in (near) contact with the wedge was determined solely as the root of the equation $\boldsymbol{u}_\infty \cdot \boldsymbol{r}_c = 0$, with the 2D fluid velocity $\boldsymbol{u}_\infty$ (in the absence of particle) calculated at the particle center. The particle center in this critical orientation was then used as the initial point for streamline integration downstream. The outlet positions x_2 of the particle center found in this simple manner, are 1.14, 1.27 and 1.46 times smaller than the exact results from Figure 3.11 for η = 0.6, 0.75 and 0.85, respectively. For η = 0.3, the particle trajectories are partially focused, which hampered the comparison.

3.5.2 A Solid Sphere in a T-bifurcation

As another and relatively easy application of our 3D algorithm, consider motion of a freely-suspended solid sphere in a plane-parallel, T-bifurcation (Figure 3.12). The volumetric flow rate $Q_T = Q_1 + Q_2$ of the fluid through the inlet is split into the flux Q_1 through the side channel and the flux Q_2 through the downstream channel, with a given partition ratio Q_1/Q_2. The inlet flow is loaded with spherical particles at dilute concentrations. Of primary interest is to determine the partition F_1/F_2 ($\neq Q_1/Q_2$) of the particle flow rates between the side (F_1) and downstream (F_2) channels; the particles may be comparable in size with the channel's width. An interest in the literature to this and similar problems has been stimulated, in part, by their relevance to the partition mechanism of red blood cells at vessel bifurcations. We are not aware, however, of 3D simulations performed previously, even for the simplified geometry shown in Figure 3.12. In an elucidating paper of Audet and Olbricht,[21] both "T" and "Y" bifurcations were studied, with calculation of F_1/F_2 (or F_1/F_T) in a broad range of the flow partitions Q_1/Q_2 and relative particle sizes. However, for a feasible solution with computer resources available at that time, Audet and

Olbricht[21] considered model, cylindrical particles by 2D boundary-integral simulations; besides, to avoid numerical difficulties with sharp corners, a smoothing radius, as large as the channels width, was used at the bifurcation joints.

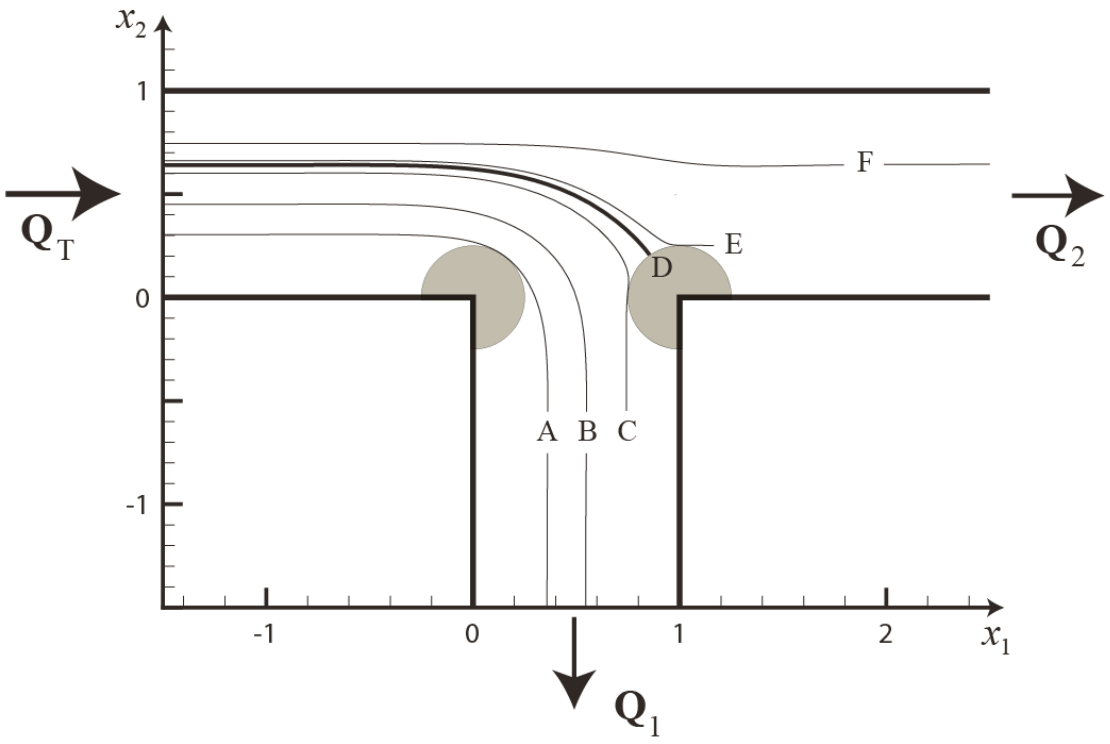

Figure 3.12 The structure of the particle center trajectories in the T-bifurcation for $Q_1/Q_2 = 3$ and $\eta = 0.5$. Shaded areas are the excluded regions for the particle center around the corners. The dividing line D separates the trajectories going into the side channel from those traveling downstream. For further details, see the text.

The present work offers, for the first time, more realistic 3D simulations for the T geometry; sharp corners at the bifurcation do not require smoothing in the present, robust algorithm. For simplicity, the inlet and both the outlet branches have the same width H used below as the lengthscale for non-dimensionalization; the tightness parameter $\eta = 2a$ is the non-dimensional particle diameter. The channel geometry extends to $x_1 = -6$ on the left, $x_1 = 7$ on the right, and $x_2 = -6$ on the bottom (outside the range of Figure 3.12) to make the end effects on the flow at bifurcation fully negligible. Figure 3.12 presents a complete classification of the particle center trajectories for $Q_1/Q_2 = 3$ and $\eta = 0.5$; far upstream, each trajectory is characterized by the vertical coordinate $x_2^0 \in (a, 1-a)$.. Most important, there is a dividing trajectory D (marked bold in Figure 3.12), which separates the trajectories entering the side branch from those going downstream. An efficient way to compute the end point of trajectory D is by considering a multitude of particle positions in apparent contact with the far corner (surface clearance of $0.01a$ sufficed) and finding the orientation of the $\boldsymbol{r}_c$-vector (from the corner to the particle center) with zero tangential velocity ($\boldsymbol{r}_c \times \boldsymbol{U} = \boldsymbol{0}$) by trial and error. Replacing the particle center velocity $\boldsymbol{U}$ by the fluid velocity $\boldsymbol{u}_\infty$, which would exist without the particle (and calculated at the particle center) was found to provide a good initial approximation for the root of the equation $\boldsymbol{r}_c \times \boldsymbol{U} = \boldsymbol{0}$, which is then refined using the 3D boundary-integral solution for $\boldsymbol{U}$. Due to the sharp corner, a number of the bioconjugate-gradient iterations in the 3D algorithm reached several hundred, making a good initial approximation for $\boldsymbol{r}_c$ quite important. For $\boldsymbol{r}_c \times \boldsymbol{U} = \boldsymbol{0}$, the angle θ between $\boldsymbol{r}_c$-vector and the positive direction of x_1-axis is 125°. The whole trajectory D is calculated from the end point by backward integration and reaches $x_2° = 0.639$ in the inlet. Since the departure from the corner is initially along $\boldsymbol{r}_c$, the computation quickly accelerates, and only the first several steps of backward integration are time consuming.

For the critical trajectory A, with $x_2^0 < 0.304$ and $x \to 0.358$ in the side outlet, the particle touches the near corner at the critical angle $\theta_{cr} \approx 56.7°$ of the $\boldsymbol{r}_c$-vector. For all trajectories with $x_2^0 = 0.304$, the particle would hit the corner and roll around it, but then separate at the same angle 56.7° of the $\boldsymbol{r}_c$-vector. The end portion of trajectory A delimits the particle-free zone in the side outlet.

For another critical trajectory, C, with $x_2^0 = 0.598$, the particle touches the far corner at the critical angle $\theta_{cr} \approx 175°$ of the $\boldsymbol{r}_c$-vector and then proceeds to the side outlet remaining in close contact with the wall ($x_1 \approx 0.743$). All the trajectories initially between A and C $(0.304 < x_2^0 < 0.598)$ would proceed from the inlet to the side outlet without reaching the channel boundaries, as demonstrated by trajectory B with $x_2^0 = 0.45$ and $x_1 \to 0.544$ in the outlet.

A narrow range $0.598 < x_2^0 < 0.639$ characterizes trajectories, initially between C and the dividing trajectory D, for which the particle hits the far corner and rolls around it, separating from the corner at the same position as trajectory C. We have also found the second critical position of the particle contacting the far corner, with $\boldsymbol{r}_c \cdot \boldsymbol{U} = 0$; the corresponding angle $\theta_c \approx 90.5°$ is just above 90°. For the trajectory E, with $x_2^0 = 0.661,$, the particle touches the corner at this critical position and then separates downstream. The particle-wall spacing, however, remains extremely small (less than $0.009a$) after the separation, making it difficult to continue trajectory E much further. For all the trajectories in the narrow range $0.639 < x_2^0 < 0.661,$ initially between D and E, the particle hits the corner and then rolls over towards the downstream channel; after the separation, the behavior is identical to that for trajectory E. Finally, for trajectories initially above E ($x_0 > 0.661$), the particle proceeds to the downstream outlet without reaching the channel boundaries. An example is trajectory F, which starts in almost contact with

the upper wall ($x_2^0 = 0.747$) reaching x_2 = 0.644 far downstream; with good accuracy, this trajectory delimits the particle-free zone. Obviously, sharp corners of bifurcation joints serve as an additional mechanism to create strong non-uniformity of particle density in the outlets.

For a relatively weak fluid suction through the side outlet and small particles (e.g., for Q_1/Q_2 = 1/3 and 2/3 with η = 0.2), the dividing particle trajectory was found to terminate not in contact with the far corner but (very) slightly below, in contact with the right wall of the side outlet. In this case, there is no solution for the particle orientation with $\boldsymbol{r}_c \times \boldsymbol{U} = \boldsymbol{0}$ in contact with the corner. Instead, we consider a multitude of particle positions in apparent contact with the wall slightly below the corner (surface clearance $\delta_w a$, $\delta_w \ll 1$) and find the configuration with zero vertical particle velocity (U_2 = 0) by trial and error. This procedure, which obviously gives the end point of the dividing trajectory, is followed by backward integration. While the temporal dynamics near the end point is strongly affected by δ_w (and suffers from numerical inaccuracies), the dividing trajectory itself is insensitive to it, and δ_2 = 0.01 was found to suffice.

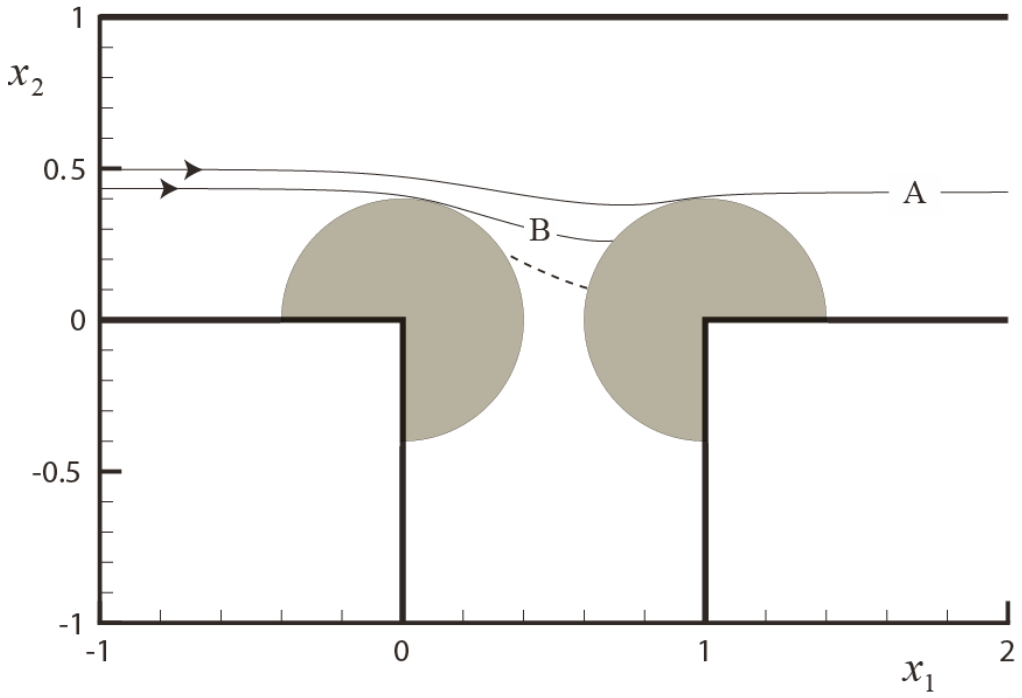

Figure 3.13 The structure of the particle center trajectories in the T-bifurcation for Q_1/Q_2 = 1/3 and η = 0.8 showing the lock-up mechanism for the side channel. For critical trajectory A (with $x_2 \rightarrow$ 0.496 and 0.426 upstream and downstream, respectively), the particle touches the right corner. For critical trajectory B (with $x_2 \rightarrow$ 0.435 upstream), the particle touches the left corner and then hits the right corner. The "dividing trajectory" (dashed line) does not extend upstream and cannot be physically realized. The side branch is inaccessible to particles regardless of the initial location in the inlet.

Another, probably most interesting possibility is observed for large particles and a relatively weak fluid suction through the side outlet; Figure 3.13 gives an example for $Q_1/Q_2 = 1/3$ and $\eta = 0.8$. In this case, there is a solution for the particle orientation with $\boldsymbol{r}_c \times \boldsymbol{U} = \boldsymbol{0}$ in contact with the far corner. However, backward integration (shown by the dashed line in Figure 3.13) from this position, results in particle hitting the left corner. Obviously such a "dividing trajectory" cannot be physically realized in the present model prohibiting particle-corner contact under tensile load (with $\boldsymbol{U}\cdot\boldsymbol{r}_c > 0$). The classification of particle trajectories in this case is as follows. For the critical trajectory A in Figure 3.13, the particle touches the right corner and then separates downstream; for all trajectories initially above A, the particle proceeds from the inlet to the outlet without reaching the channel boundaries. The critical trajectory B corresponds to the particle touching the left corner and then hitting the right corner; upon rolling around the corner, the subsequent separation and motion are the same as for trajectory A. For all trajectories initially between A and B, the particle would miss the left corner but hit the next one. All the trajectories initially below A would result in particle hitting and rolling over the left corner before separation. Remarkably, despite the appreciable fluid suction through the side outlet ($Q_1/Q_2 = 1/3$), *no* particle can enter this outlet regardless of the initial location in the inlet section!

When the dividing trajectory, obtained from the end point by backward integration, does extend far upstream without hitting the left corner (like in Figure 3.12), calculation of partition ratio F_1/F_2 of the particle fluxes through the outlets can be performed. This calculation is a much easier task than the complete trajectory analysis. According to Audet and Olbricht,[21] it is sufficient to know the particle density distribution across the inlet and the location of the

dividing trajectory far upstream to calculate F_1/F_2. For a "well-mixed" suspension in the inlet, all geometrically feasible positions $x_2^0 \in (a, 1-a)$ have equal probability density, and

$$F_1 \Big/ F_2 = \left[\int_a^{x_2^*} U\left(x_2^0\right) dx_2^0\right] \Big/ \left[\int_{x_2^*}^{1-a} U\left(x_2^0\right) dx_2^0\right] \quad , \tag{3.24}$$

where x_2^* is the value of the upstream vertical coordinate x_2^0 for the dividing trajectory, and $U(x_2^0)$ is the velocity (along x_1-axis) for the particle centered at $(x_1, x_2^0 \to -\infty)$ Obviously, an economical way to calculate the integrals (24) is to take the velocity U from the solution for a freely suspended sphere in a Poiseuille flow between two *infinite* plane walls discussed in Section 3.4.2 (which is justified since the inlet is far upstream). So, we used Table 3.1 from Staben *et al.*[3] with quadratic interpolation to calculate $U(x_2^0)/U_c$ for all $d/a \geq 1.01$, where U_c is the Poiseuille flow velocity in the middle between the two walls, and $d = \min(x_2^0,\ 1-x_2^0)$ is the distance from the particle center to the nearest wall. For $d/a < 1.01$, the accuracy of this solution deteriorates, and we instead used a near-contact asymptotic form adapted from Staben et al.[3]

$$\frac{U\left(x_2^0\right)}{U_c} = \frac{F^p T^r + F^r T^p}{F^t T^r - 3\left(F^r\right)^2/4} \quad . \tag{3.25}$$

Here,

$$F^t = -\frac{8}{15}\ln\left(\frac{\delta_1}{a}\right) - \frac{8}{15}\ln\left(\frac{\delta_2}{a}\right) + \Delta F^t \quad , \tag{3.26}$$

$$T^r = -\frac{2}{15}\ln\left(\frac{\delta_1}{a}\right) - \frac{2}{15}\ln\left(\frac{\delta_2}{a}\right) + \Delta T^r \quad , \tag{3.27}$$

$$F^r = -\frac{2}{15}\ln\left(\frac{\delta_1}{a}\right) + \frac{2}{15}\ln\left(\frac{\delta_2}{a}\right) + \Delta F^r \quad , \tag{3.28}$$

and δ_1 and δ_2 are the particle surface clearances from the nearest wall and the other wall, respectively. The coefficients F^{p}, T^{p}, ΔF^{t} and ΔT^{r} depend on the tightness parameter η only, and are taken from the table of Staben *et al.*[57] Expressions (26)-(28) for the resistance coefficients F^{t}, T^{r}, F^{r}, with the one-wall, log-term lubrication contributions,[58] are designed to make (3.25) accurate when one or both gaps δ_1, δ_2 are much smaller than a. Due to oversight in Staben *et al.*[3] (still uncorrected in Ref. [57]), the second logarithmic contribution to F^{r} therein has an incorrect sign. To compensate for this error, the formula (28) for F^{r} must be used with a modified after-log contribution ΔF^{r}, which differs from than in Ref. [57] by an additional quantity $-4\ln[(1-2a)/a]/15$ (these modifications are essential only for particle tightness $2a$ very close to 1). Comparisons with the more recent, multipole solution for a sphere between two parallel walls[9] at η = 0.2, 0.5 and 0.9 shows that the error of the approximation (25) does not exceed 1% for all $d/a < 1.01$; this accuracy is sufficient, since the near-contact regions generally make a rather small contribution to (3.24).

Table 3.7 presents our results for the upstream location of the dividing trajectory and the particle flux partition ratio F_1/F_2 for three particle sizes η = 0.2, 0.5, 0.8 and different fluid flux partition ratios Q_1/Q_2. Zero values of F_1/F_2 correspond to the case when the "dividing trajectory," obtained from the end point by backward integration, does not extend upstream, hitting the left corner instead. Interestingly, for η = 0.8, the side branch is inaccessible to particles even for Q_1/Q_2 = 2/3; this flow ratio is near-critical to block the particles from the side branch.

η	Q_1/Q_2 =	1/7	1/3	2/3	1	3/2	3	7
0.2	x_2^* =	0.219	0.328	0.435	0.501	0.567	0.671	0.773
	F_1/F_2 =	0.104	0.302	0.652	1.01	1.55	3.28	8.83
0.5	x_2^* =	–	0.346	0.440	0.499	0.556	0.639	0.708
	F_1/F_2 =	0	0.187	0.565	0.987	1.69	4.31	16
0.8	x_2^* =	–	–	–	0.483	0.520	0.565	0.589
	F_1/F_2 =	0	0	0	0.689	1.55	5.35	23

Table 3.7 The upstream location of the dividing trajectory (x_2^*) and the particle fluxes partition ratio (F_1/F_2) for the T-bifurcation. In some cases, such a trajectory does not exist, and no particles can enter the side outlet, regardless of the initial locations in the inlet.

Qualitatively, our 3D results for spheres show similarities with the 2D calculations of Audet and Olbright[21] for cylindrical particles. Both solutions confirm that the particles favor a higher flow-rate branch, so that $F_1/F_2 < Q_1/Q_2$ for small Q_1/Q_2 and $F_1/F_2 > Q_1/Q_2$ for large Q_1/Q_2; this feature is observed in many experiments. Moreover, for $Q_1/Q_2 = 1/7$ and $\eta = 0.5$, Figure 2c of Audet and Olbricht[21] appears to indicate that no particle can access the side branch (consistent with our Table 3.7), although the full range of initial particle locations in the inlet could not be studied in their work due to numerical difficulties. Our analysis, covering the whole range of initial locations, presents a clear picture of how the particle blockage from the side channel results from interaction with the sharp corners of the bifurcation. Quantitatively, significant deviations are observed between our 3D results and the calculations of Audet and Olbright[21] for particles of moderate and large size. For example, at $\eta = 0.5$, their $s = 1$ results for F_1/F_2 (corresponding to well-mixed particles in the inlet) are 20%, 28% and 47% lower than our values in Table 3.7 when $Q_1/Q_2 = 1/3$, 1 and 3, respectively. In our calculations, the half-size of the computational cell around the particle was $A = 6a$ to $9a$; the number of nodes on the cell contour and the number of triangular elements on the sphere at the end point of the dividing trajectory were 170-240 and 5120-8640, respectively. By variation of the program parameters, the accuracy of the three-digit results for F_1/F_2 in Table 3.7 is estimated as 0.5%-1%. It is not clear at present if the deviations from the solution of Audet and Olbricht[21] are mostly due to three-dimensional formulation herein, or to sharp corners in our geometry.

3.6 Conclusions

A three-dimensional, Moving-Frame Boundary-Integral Method (MFBIM) has been developed to accurately simulate motion of a spherical particle in plane-parallel microchannels of arbitrary, complex shape with bifurcations. Neutral buoyancy and low-Reynolds number

conditions are assumed. A standard approach would require a simultaneous solution of boundary-integral equations on the particle surface and the entire channel boundary. However, when the particle (which may be comparable in size with the narrowest channel dimensions) is much smaller than the overall channel domain, such an approach would be prohibitively expensive for dynamical simulations, due to a very large number of unknowns on the channel boundary. The central idea behind our algorithm is to embed the particle in a dynamically constructed computational cell ("moving frame") and solve the 3D boundary-integral problem in the cell only, with the outer boundary conditions provided by the 2D flow that would exist in the channel without the particle. The cell (constructed in a non-trivial fashion) is much larger than the particle, but can be made, in many cases of interest, much smaller than the overall channel domain, resulting in manyfold computational savings compared to the standard approach. The channel profile may consist of an arbitrary number of straight line segments in arbitrary configuration, which is a suitable model for particle transport in many microfluidic devices. To handle the close interactions of the particle with the walls, and especially with sharp corners of the device, crucial elements of the algorithm include corner-fitted, gap-adaptive discretizations of the cell boundary, special singularity and near-singularity subtractions, biconjugate-gradient boundary-integral iterations, and optional adaptivity of the particle surface triangulations. Unlike for particle interaction with smooth parts of the channel, the particle contact with a sharp corner can be reached with relatively little resistance, and in a finite time. Our model assumes that, once the contact is reached, it can only be maintained under compressive load. Accordingly, the concept of the critical particle orientation in (near) contact with a corner, where detachment occurs, is systematically used in our simulations. It may seem natural to apply Faxen's formula for particle motion in complex microchannels, but we have found it to be of little use in the

present work because of a very narrow range of validity; such an approach is not a substitute for the "moving-frame" solution.

The algorithm has been applied, for the first time, the rigorous 3D simulations of the "pinched-flow fractionation" (PFF), when particles, fed into one of the input branches, are being pressed by a buffer liquid (entering the second branch) to the wall of the pinched area, and eventually separate into the outlet. It is demonstrated how interaction of sufficiently large particles with sharp corners of the device makes their motion in the outlet fully focused, i.e., independent of the initial locations in the inlet. Our solution also predicts the effect of the particle size on their fractionation in the outlet, in reasonable quantitative agreement with the experiments of Nakashima *et al.*[10] Modest deviations from their measurements may be mostly due to small depth of their device (assumed infinite in the present plane-parallel geometry) and, to a lesser extent, to inertial effects neglected herein.

As another application of the developed algorithm, motion of a realistic 3D solid sphere in a T-bifurcation with sharp corners was simulated for the first time. Here, the fluid flux $Q_T = Q_1 + Q_2$ through the upstream branch is split into the fluxes through the side (Q_1) and downstream (Q_2) branches, with a specified partition ratio Q_1/Q_2; of primary interest is to determine the corresponding partition F_1/F_2 of the particle fluxes. For selected values of Q_1/Q_2 and the non-dimensional particle diameter η (scaled with the channel width), we present complete classification of particle trajectories and demonstrate how the particle interactions with sharp corners of the bifurcation can make the side branch totally inaccessible to the particle regardless of its initial location in the inlet. Interestingly, for $\eta = 0.8$, this blockage of the side branch is observed even for a relatively strong fluid suction ($Q_1/Q_2 = 2/3$) through this branch. We calculated the particle flux ratio F_1/F_2 in a broad range of Q_1/Q_2 (from 1/7 to 7) and η (from 0.2

to 0.8). Our results are qualitatively similar to those from 2D boundary-integral simulations for a cylindrical particle in a T-bifurcation with smooth corners.[21] The 2D model, however, is observed to significantly under predict F_1/F_2. It remains to be explored if the observed deviations are mostly due to the 3D formulation or sharp corners in our geometry.

It seems likely that the basic idea of the economical moving-frame solution can be extended to finite Reynolds number particle transport in microchannels of complex shape, and we will attempt such solutions in the future. Future work will also include the generalization of MFBIM for transport of deformable 3D particles or drops in complex microchannels. The MFBIM scheme is also attractive for simulating isolated clusters of several particles (drops) in a channel; the computational cell around a cluster can be constructed in the same manner as for single objects. However, for suspensions (emulsions) of particles (drops) filling the entire channel, with strong hydrodynamical interactions, this scheme would not provide a suitable replacement for a much more complex, multipole-accelerated boundary-integral solution of the 3D problem in the whole domain.

3.7 Acknowledgment

J.F.A. would like to acknowledge the Ashley/McCormic Research Institute 06204591 for financial support.

3.8 Appendices

3.A Details of the 2D and 3D algorithms

Calculation of the added-back integrals (3.8). The vector field $r_j r_k/(\pi r^4)$ corresponding to the 2D fundamental stresslet equation (3.2) is divergence-free and can be described by the stream function easily found in the explicit form. Accordingly, the added-back integral in (3.8), which is the flux of $\boldsymbol{\tau}^{2D}$ through the line segment $\mathcal{L}_i$, is calculated componentwise as

$$\left\{\int_{\mathcal{L}_i} \boldsymbol{\tau}^{2D}(\boldsymbol{r})\cdot\boldsymbol{n}(\boldsymbol{x})\,dS_x\right\}_{jk} = \pm\frac{\alpha}{2\pi}+\frac{1}{2\pi}\left[\psi_{jk}\right]_A^B \quad . \tag{3.A1}$$

Here, $\alpha\in[0,\pi]$ is the angle at which the segment $\mathcal{L}_i$ is seen from the observation point $\boldsymbol{y}$; the plus and minus signs are taken when $\boldsymbol{r}\cdot\boldsymbol{n}(\boldsymbol{x}) > 0$ and $\boldsymbol{r}\cdot\boldsymbol{n}(\boldsymbol{x}) < 0$ on the segment $\mathcal{L}_i$, respectively. In the last term of (A1), $[\cdots]_A^B$ is the jump of the quantity in the brackets from the starting point (A) to the end point (B) of $\mathcal{L}_i$. The channel contour $\mathcal{L}$ with the outward normal $\boldsymbol{n}$ is assumed to be passed counterclockwise. Finally,

$$\psi_{11} = -\psi_{22} = \frac{r_1 r_2}{r^2} \quad , \quad \psi_{12} = \psi_{21} = \frac{\left(r_2^2 - r_1^2\right)}{2r^2} \quad . \tag{3.A2}$$

Generation of the computational cell contour $\mathcal{C}$ for the 3D algorithm. When the intersection of the entire channel with the bounding square $|x_i - (x_c)_i| < A$ (I = 1,2) around the particle is a single domain, the contour $\mathcal{C}$ of this domain is generated as follows. Moving continuously along the channel perimeter (counterclockwise, so that the channel domain remains on the left), we mark successively the channel vertices inside the square and the intersection points with the square boundary as future vertices of contour $\mathcal{C}$. Whenever the channel perimeter exits the square and then re-enters it (at the same or different square side), the path along the channel perimeter from the exit to the re-entry point is replaced by the corresponding path along the square perimeter in the counterclockwise direction. This process is continued until a closed contour $\mathcal{C}$ is obtained. For channels of complex shape, difficulties may arise when the intersection of the bounding square and the channel domain consists of several isolated pieces. In PFF simulations, we encountered (extremely rarely, and for large cells only) the situations when this intersection consists of two separate parts. Each part was generated by a specific modification of the algorithm above, and the part containing the particle was chosen as the computational cell. A

universal remedy, though, would be difficult to develop. Note also that, as the particle moves through the channel, some sides of contour $\mathcal{C}$ can degenerate to a point, with no collocation nodes inside. Such situations are simply avoided by slightly changing the value of A.

Calculation of the added-back integrals (3.20). Bazhlekov *et al.*[47] were the first to notice that, since the 3D fundamental stresslet (3.10) is divergence-free, its flux through any patch on a surface can be calculated as a contour integral over the patch boundary, although their arguments are somewhat lengthy. We simply note herein that

$$\frac{3r_i r_k \boldsymbol{r}}{r^5} = \nabla \times \left[r_i \cdot \frac{\left(\boldsymbol{e}_k \times \boldsymbol{r}\right)}{r^3} \right] + \frac{\delta_{ik}\boldsymbol{r}}{r^3} \tag{3.A3}$$

where $\boldsymbol{e}_k$ is the unit vector of the coordinate axis x_k. Accordingly, using the Stokes theorem, one obtains for the added-back integral in (3.20):

$$3\int_{S_j^\infty} \frac{[\boldsymbol{r}\cdot\boldsymbol{n}(\boldsymbol{x})] r_i\, r_k}{r^5} dS_x = \pm\omega\delta_{ik} + \boldsymbol{e}_k \cdot \int_{\Gamma_j} \frac{r_i \left(\boldsymbol{r}\times d\boldsymbol{r}\right)}{r^3} \,. \tag{3.A4}$$

Here, ω is the body angle at which the rectangular panel S_j^∞ is seen from the observation point, and Γ_j is the panel perimeter with the direction seen counterclockwise from the end point of the normal vector $\boldsymbol{n}$; the plus/minus sign in (3.A4) is for $\boldsymbol{r}\cdot\boldsymbol{n} > 0$ and $\boldsymbol{r}\cdot\boldsymbol{n} < 0$ on the panel S_j^∞, respectively. Dividing the panel by a diagonal, ω is easily calculated as the sum of the areas of two spherical triangles using well-known formulae from spherical trigonometry. Since the path Γ_j consists of straight line segments $[\boldsymbol{P}_m\boldsymbol{P}_{m+1}]$, their contributions to the last integral (3.A4) are even easier to calculate,[47] and the results can be written as

$$\int_{P_m}^{P_{m+1}} \frac{\left[\boldsymbol{e}_k \cdot \left(\boldsymbol{r}\times d\boldsymbol{r}\right)\right]\boldsymbol{r}}{r^3} = \frac{\left[\boldsymbol{e}_k \cdot \left(\boldsymbol{z}_m \times \boldsymbol{z}_{m+1}\right)\right]\left(\boldsymbol{z}_m + \boldsymbol{z}_{m+1}\right)}{1+\boldsymbol{z}_m\cdot\boldsymbol{z}_{m+1}} \tag{3.A5}$$

where $\boldsymbol{z}_m$ and $\boldsymbol{z}_{m+1}$ are the unit directors of $\boldsymbol{P}_m - \boldsymbol{y}$ and $\boldsymbol{P}_{m+1} - \boldsymbol{y}$, respectively.

It should be noted, however, that our technique (3.20) to reduce the near-singularity of the double-layer integrals over rectangular panels is different from the general methodology of Bazhlekov *et al.*[47] Their approach would assume $\boldsymbol{q}(\boldsymbol{x})$ const within each boundary element, with calculation of $\boldsymbol{\tau}\cdot\boldsymbol{n}$ over this element by contour integration; such a technique is more costly and, in general, only first-order accurate.

Optional mesh adaptivity on the particle surface. Except for the simulations where the particle can come extremely close to sharp corners of a channel, the following procedure of gap-adaptive redistribution of mesh nodes can be recommended. At each particle configuration, we seek to minimize the mesh "potential energy" of the form

$$E = \sum_{x_{ij}} \left[\frac{1}{2} \left(\frac{x_{ij}^2}{\ell_{ij}^2} + \frac{\ell_{ij}^2}{x_{ij}^2} \right) \right]^{\nu} + c_E \sum_{\Delta} \frac{1}{C_{\Delta}^{\beta}} \tag{3.A6}$$

Here, the first summation is over all mesh edges $\boldsymbol{x}_{ij} = \boldsymbol{x}_j - \boldsymbol{x}_i$ (with $i < j$) between directly connected nodes of a triangular mesh. The "target" value of the distance $|\boldsymbol{x}_{ij}|$ is ℓ_{ij}, which depends on the clearance between $\boldsymbol{x}_i$, $\boldsymbol{x}_j$ and the channel walls. Namely,

$$\ell_{ij}^2 = \frac{1}{2}\left(f_i + f_j \right) \quad , \quad f_i = K\delta_i^{\gamma} \tag{3.A7}$$

$$\delta_i = \frac{h_i + h_b}{h_i + a} \quad , \quad K = \frac{4}{N_{\Delta}\sqrt{3}} \sum_{x_u} \frac{\Delta S_i}{\delta_i^{\gamma}} \quad , \tag{3.A8}$$

where h_{i} is the distance from mesh vertex $\boldsymbol{x}_i$ on S_{p} to the channel boundary measured along the outward normal $\boldsymbol{n}(\boldsymbol{x}_i)$ to the particle surface, and h_{b} (~0.003a) is the threshold to limit adaptivity for too small particle-wall spacing. For numerical tests in Section 3.4, we used $\nu = \gamma = 1$. The fractional form (3.A8) for δ_i is used to weaken the dependence on h_{i}, when $h_i >> 1$, and thereby smooth the energy function (3.A6).

The first term in (3.A6) bears some resemblance to the spring-like potential mesh energy that Cristini *et al.*[44] used in their deformable drop simulations (with quite different target scales ℓ_{ij}). We found the extra term (borrowed from Zinchenko and Davis[32]) to greatly improve robustness by preventing mesh triangle collapse, so mesh topology transformations could be avoided altogether. In this term, the summation is over all mesh triangles Δ on S_p, and $C_\Delta = S_\Delta/(a_1^2+a_2^2+a_3^2)$ is the "compactness" of triangle Δ with area S_Δ and sides a_1, a_2 a_3; numerical constants $c_E = 0.02$ and $\beta = 2$ were used herein.

The energy E is minimized iteratively (cf. Zinchenko and Davis[32]):

$$\boldsymbol{x}_i^{new} = \boldsymbol{x}_i - \lambda \frac{\partial E}{\partial \boldsymbol{x}_i} \quad , \quad \lambda = 0.01 \min_{x_i} \frac{\Delta x_i}{\left\| \partial E / \partial \boldsymbol{x}_i \right\|} \quad , \tag{3.A9}$$

where Δx_i is the shortest distance from $\boldsymbol{x}_i$ to its neighbors; the form (3.A9) for λ serves very gradual mesh transition. To simplify the method, partial derivatives $\partial E/\partial \boldsymbol{x}_i$ are calculated as if the target scales ℓ_{ij}^2 were independent of the node positions $\boldsymbol{x}_i$, $\boldsymbol{x}_j$; this incompleteness is compensated by updating ℓ_{ij}^2 on each iteration. After the operation (3.A9), the mesh nodes are placed back on the surface, which is particularly easy for a sphere by rescaling $\boldsymbol{x}_i^{new}$ about the particle center. In dynamical simulations, with a good initial approximation for $\boldsymbol{x}_i$ from the preceding time step, iterations (3.A9) to stabilize E do not degrade the overall algorithm performance.

Although this mesh algorithm was found to be generally very robust and improves the accuracy, it must give ground to non-adaptive surface triangulations when the particle comes very close to a sharp corner, to avoid too slow convergence of boundary-integral iterations. In

both adaptive and non-adaptive versions, the number N_Δ of triangular elements for each configuration is set as

$$N_\Delta \approx c_\Delta \int_{S_p} \frac{dS}{\delta^\gamma} \quad , \tag{3.A10}$$

with a constant c_Δ.

3.9 REFERENCES

[1] J. Happel and H. Brenner, *Low Reynolds Number Hydrodynamics*, 4th ed., Martinus Nijhoff, Dordecht (1986).

[2] C. Couillette and C. Pozrikids, Flow due to a periodic array of point forces, and the motion of small particles within a cylindrical tube of arbitrary cross section *Phys. Fluids* **8**, 2019-2031 (1996).

[3] M.E. Staben, A.Z. Zinchenko, and R.H. Davis, Motion of a particle between two parallel walls in low-Reynolds-number Poiseuille flow *Phys. Fluids* **15**, 1711-1733 (2003).

[4] P. Ganatos, R. Pfeffer, and S. Weinbaum, A strong interaction theory for the creeping motion of a sphere between plane parallel boundaries. 2. Parallel motion, *J. Fluid Mech.* **99**, 755-783 (1980).

[5] M.E. Staben, A.Z. Zinchenko, and R.H. Davis, Dynamic simulation of spheroid motion between two parallel plane walls in low-Reynolds-number Poiseuille flow *J. Fluid Mech.* **553**, 187-226 (2006).

[6] S. Bhattacharya, J. Blawzdziewicz, and E. Wajnryb, Many-particle hydrodynamic interactions in parallel-wall geometry: Cartesian-representation method *Physica A* **356**, 294-340 (2005a).

[7] S. Bhattacharya, J. Blawzdziewicz, and E. Wajnryb, Hydrodynamic interactions of spherical particles in suspensions confined between two planar walls *J. Fluid Mech.* **541**, 263-292 (2005b).

[8] S. Bhattacharya, J. Blawzdziewicz, and E. Wajnryb, Far-field approximation for hydrodynamic interactions in parallel-wall geometry *J. Comp. Physics* **212**, 718-738 (2006a).

[9] S. Bhattacharya, J. Blawzdziewicz, and E. Wajnryb, Hydrodynamic interactions of spherical particles in Poiseuille flow between two parallel walls *Phys. Fluids* **18**, 053301 (2006b).

[10] M. Nakashima, M. Yamada, and M. Seki, Pinched flow fractionation (PFF) for continuous particle separation in a microfluidic device 17th IEEE International Conference on Micro Electro Mechanical Systems, Maastricht, The Netherlands, 33-36 (2004).

[11] M. Yamada, M. Nakashima, and M. Seki, Pinched flow fractionation: Continuous size separation of particles utilizing a laminar flow profile in a pinched microchannel *Anal. Chem.* **76**, 5465-5471 (2004).

[12] Y. Sai, M. Yamada, M. Yasuda, and M. Seki, Continuous separations of particles using a microfluidic device equipped with flow rate control valves *J. Chromatography A* **1127**, 214-220 (2006).

[13] A. Jain and J.D. Posner, Particle dispersion and separation resolution of pinched flow fractionation *Anal. Chem.* **80**, 1641-1648 (2008).

[14] B.P. Ho and L.G. Leal, Inertial migration of rigid spheres in 2-dimensional unidirectional flows *J. Fluid Mech.* **65**, 365-400 (1974).

[15] S. Chien, C.D. Tvetenstrand, M.S. Farrel Epstien, and G.W. Schmid-Schnbien, Model studies on distributions of blood cells at microvascular bifurcations *Amer. J. Physiol.* **248**, H568-H576 (1985).

[16] R. Ditchfield and W.L. Olbricht, Effects of particle concentration on the partitioning of suspensions at small divergent bifurcations *J. Biomech. Eng.* **118**, 287-294 (1996).

[17] K. Svanes and B. Zweifach, Variations in small blood vessel hematocrits produced in hypothermic rats by micro-occlusion *Microvas. Res.* **1**, 210-220 (1968).

[18] Y.-C. Fung, Stochastic flow in capillary blood vessels *Microvas. Res.* **5**, 34-48 (1973).

[19]B.W. Roberts and W.L. Olbricht, Flow-induced particulate separations *AIChE J.* **49**, 2842-2849 (2003).

[20] B.W. Roberts and W.L. Olbricht, The distribution of freely suspended particles at microfluidic bifurcations *AIChE J.* **52**, 199-206 (2006).

[21] D.M. Audet and W.L. Olbricht, The motion of model cells at capillary bifurcations *Microvasd. Res.* **33**, 377-396 (1987).

[22] C.S. Peskin, Numerical analysis of blood flow in the heart *J. Comput. Physics* **25**, 220-252 (1977).

[23] E.A. Fadlun, R. Verzicco, P. Orlandi, and J. Mohd-Yusof, Combined immersed-boundary finite-difference methods for three-dimensional complex flow simulations *J. Comput. Physics* **161**, 35-60 (2000).

[24] A. Pinelli, I.Z. Naqavi, U. Piomelli, and J. Favier, Immersed-boundary methods for general finite-difference and finite-volume Navier-Stokes solvers *J. Comput. Physics* **229**, 9073-9091 (2010).

[25] R. Glowinski, T.-W. Pan, T.I. Hesla, and D.D. Joseph, A distributed Lagrange multiplier/ fictitious domain method for particulate flows *Int. J. Multiphase Flow* **25**, 755-794 (1999).

[26] N.A. Patankar, P. Singh, D.D. Joseph, R. Glowinski, and T.-W. Pan, A new formulation of the distributed Lagrange multiplier/fictitious domain method for particulate flows *Int. J. Multiphase Flow* **26**, 1509-1524 (2000).

[27] N. Sharma, Y. Chen, and N.A. Patankar, A distributed Lagrange multiplier based computational method for the simulation of particulate-Stokes flow *Comput. Methods Appl. Mech. Engrg.* **194**, 4716-4730 (2005).

[28] G.J. Wagner, N. Moes, W.K. Liu, and T. Belytschko, The extended finite element method for rigid particles in Stokes flow *Int. J. Numer. Meth. Engng.* **51**, 293-313 (2001).

[29] G.J. Wagner, S. Ghosal, and W.K. Liu, Particulate flow simulations using lubrication theory solution enrichment *Int. J. Numer. Meth. Engng.* **56**, 1261-1289 (2003).

[30] A.Z. Zinchenko and R.H. Davis, An efficient algorithm for hydrodynamical interaction of many deformable drops *J. Comp. Physics* **157**, 539-587 (2000).

[31] A.Z. Zinchenko and R.H. Davis, Shear flow of highly concentrated emulsions of deformable drops by numerical simulations *J. Fluid Mech.* **455**, 21-62 (2002).

[32] A.Z. Zinchenko and R.H. Davis, Algorithm for direct numerical simulation of emulsion flow through a granular material *J. Comp. Physics* **227**, 7841-7888 (2008).

[33] C. Pozrikidis, *Boundary Integral and Singularity Methods for Linearized Viscous Flow*, Cambridge University Press, Cambridge, MA (1992).

[34] S. Kim and S. Karilla, *Microhydrodynamics: Principles and Selected Applications.* Butterworth-Heinemann, Boston, MA (1991).

[35] H. Power and L.C. Wrobel, *Boundary Integral Methods in Fluid Mechanics.* Computational Mechanics Publications, Southampton-Boston (1995).

[36] J.J.L. Higdon, Stokes flow in arbitrary two-dimensional domains: Shear flow over ridges and cavities *J. Fluid Mech.* **159**, 195-226 (1985).

[37] M.A. Kelmanson, Modified integral equation solution of viscous flows near sharp corners *Computers & Fluids* **11**, 307-324 (1983).

[38] M.A. Kelmanson, An integral equation method for the solution of singular slow flow problems *J. Comp. Phys.* **51**, 139-158 (1983).

[39] O.A. Ladyzhenskaya, *The Mathematical Theory of Viscous Incompressible Flow*, 2nd edn., Gordon and Breach, New York, NY (1969).

[40] F.K.G. Odqvist, Uber die randwertaufgaben der hydrodynamic zaher Flussigkeiten *Math. Z.* **32**, 329-375 (1930).

[41] H. Power and G. Miranda, Second kind integral equation formulation of Stokes flow past a particle of arbitrary shape *SIAM J. Appl. Maths* **47**, 689-698 (1987).

[42] A.Z. Zinchenko, M.A. Rother, and R.H. Davis, A novel boundary-integral algorithm for viscous interaction of deformable drops *Phys. Fluids* **9**, 1493-1511 (1997).

[43] M. Loewenberg and E.J. Hinch, Numerical simulation of aconcentrated emulsion in shear flow *J. Fluid Mech.* **321**,395-419 (1996).

[44] V. Cristini, J. Blawzdziewicz, and M. Loewenberg, An adaptive mesh algorithm for evolving surfaces: simulations of drop breakup and coalescence *J. Comput. Phys.* **168**, 445-463 (2001).

[45] J.M. Rallison, A numerical study of the deformation and burst of a viscous drop in general shear flows *J. Fluid Mech.* **109**, 465-482 (1981).

[46] A.Z. Zinchenko and R.H. Davis, A boundary-integral study of a drop squeezing through interparticle constrictions *J. Fluid Mech.* **564**, 227-266 (2006).

[47] J.B. Bazhlekov, P.D. Anderson, and H.E.H. Meijer, Nonsingular boundary integral method for deformable drops in viscous flows *Phys. Fluids* **16**, 1064-1081 (2004).

[48] F. Pan and A. Acrivos, Steady flows in rectangular cavities *J. Fluid Mech.* **28**, 643-655 (1967).

[49] O. Burggraf, Analytical and numerical studies on the structure of steady separated flows *J. Fluid Mech.* **24**, 113-151 (1966).

[50] R.P. Gupta and M.M. Manohar, Boundary approximations and accuracy in viscous flow computations *J. Comput. Phys.* **31**, 265-288 (1979).

[51] R.P. Gupta, M.M. Manohar, and B. Noble, Nature of viscous flows near sharp corners *Computers and Fluids* **9**, 379-388 (1981).

[52] W.R. Dean and P.E. Montagnon, On the steady motion of viscous liquid in a corner *Proc. Camb. Phil. Soc.* **45**, 389-394 (1949).

[53] H.K. Moffatt, Viscous and resistive eddies near a sharp corner *J. fluid Mech.* **18**, 1-18 (1964).

[54] N. Liron and N. Mochon, Stokes flow for a Stokes-let between 2 parallel flat plates *J. Eng. Math.* **10**, 287-303 (1976).

[55] H.A. Lorentz, A general theorem concerning the motion of a viscous fluid and a few consequences derived from it *Zittingsverlag Konikl. Akad. Wet*[56] J.R. Blake, A note on the image system for a Stokeslet in a no-slip boundary *Proc. Cambridge Philos. Soc.* **70**, 303-310 (1971).

[57] M. Staben, A.Z. Zinchenko, and R.H. Davis, Erratum: Motion of a particle between two parallel plane walls in low-Reynolds-number Poiseuille flow *Phys. Fluids* (2003) **15,** 1711-1733). *Phys. Fluids* **16**, 4204-4206 (2004).

[58] A.J. Goldman, R.G. Cos, and H. Brenner, Slow viscous motion of a sphere parallel to a plane wall. I. Motion through a quiescent fluid *Chem. Eng. Sci.* **22**, 637-651 (1967). *ensch. Amsterdam* **5**, 168-175 (1896) [also in *Abhandlungenuber Theoretische Physik* (Leipzig, Berlin, 1907), Vol. 1, p. 23-42; and Collected Papers (Martinus Nijhoff, The Hague, 1937), Vol. 4, p. 7].

Chapter 4

Hydrodynamic Selection of Particulate Matter using Pinched-Flow Fractionation

(Ashley, Bowman, Davis, in review at *AIChE J.*)

The motion of rigid particles moving in a neutrally-buoyant fluid through a pinched-flow fractionation (PFF) device at low Reynolds numbers is determined numerically using a boundary-integral method (BIM). The PFF device provides a means for separating particles by size using a bifurcated microfluidic channel. Trajectories of particles having different sizes are controlled by the ratio of each particle diameter to the pinch height, the ratio of fluid flow rates in the two inlet channels, and channel geometry. Several PFF configurations were simulated to determine the effect of channel geometry on the critical flow ratio (flow-rate ratio of the two input channels) required to achieve complete separation of large and small particles. The critical flow ratio decreases with increasing diameter of the larger particles relative to the pinch height, and is nearly independent of the size of the smaller particles. A narrow pinch with a square exit was shown to have the lowest critical flow ratio and, hence, was selected to fabricate a device. Experiments were conducted using this channel geometry to compare particle trajectories to those simulated using BIM. The experiments confirm that the larger particles exit further from the top wall, due to steric exclusion, and the final exit positions are within a few percent of the simulation results. The use of the BIM in modeling the transport of particles in a complex microchannel is shown to be a valuable tool in the design of a microfluidic device with characteristics that optimize application-specific performance.

4.1 Introduction

The use of microchannel devices to sort and separate particles in a liquid is important for a number of industries and applications. Biotechnology and biomedical industries use processes that separate viruses, cells, organelles, and microbes by size,[1-7] while various manufacturing applications require sorting of ceramic particles, polymeric beads and components of encapsulated drug-delivery systems and by necessity employ microchannel devices that separate particles by size.[8]

Several methods utilizing microchannel devices are available for microparticle separation. Dielectrophoresis (DEP)[9-11] and field-flow fractionation (FFF)[12-18] allow for the sorting of particulate matter on a limited scale. They utilize microfluidics, but do not provide continuous-flow operation and are used for limited quantities of particles. Continuous microparticle separation methods include continuous DEP, acoustic methods, and split-flow fractionation.[19,20]

In this work, particles made neutrally buoyant by suspension in a fluid of equal density are separated by size using pinched-flow fractionation (PFF). Pinched-flow fractionation, as illustrated in Figure 4.1, provides a method for separation of small particles by size based on principles of fluid mechanics and steric exclusion.[21] Incorporation of pinched-flow fractionation in a microchip would provide for the continuous separation of particulate matter utilizing microfluidics. Figure 4.1 shows a pinched-flow-fractionation channel (not to scale), with key sections labeled. The device consists of two entry channels, a pinch area and an expansion area that serves as an exit where the two entry channels meeting at the entrance to the pinch region are separated by an angle θ_i. It is assumed that channel width W in the direction normal to the plane of Figure 4.1 is large compared to the channel height H, so that the flow of pure fluid through the channel is two-dimensional (2D). However, the introduction of particles into this

device gives rise to three-dimensional (3D) flow around the particles. Particles are introduced along with the fluid in the top inlet channel (subscript i), while pure fluid is introduced in the bottom sweep channel (subscript s) to force the particles toward the upper wall of the pinch region (subscript p). At lower flow ratios, defined as the ratio Q_s/Q_i of the sweep and inlet flow rates, the particles are not forced near the upper pinch wall and incomplete separation of particles in the exit area takes place, resulting in a 'banding' effect. Under these circumstances a 'band' of exit trajectories forms for each particle size with the potential for the suboptimal condition in which overlap of the bands occurs for particles of different sizes. At high flow ratios, all particles are essentially pressed against the upper wall of the pinch, such that all particles of a given size theoretically would follow a single trajectory into the exit region (subscript e), starting at one radius from the upper wall of the pinch. Thus, larger particles remain a greater distance from the wall, follow a distinct trajectory exiting the pinch region, and ultimately can be separated from smaller particles.

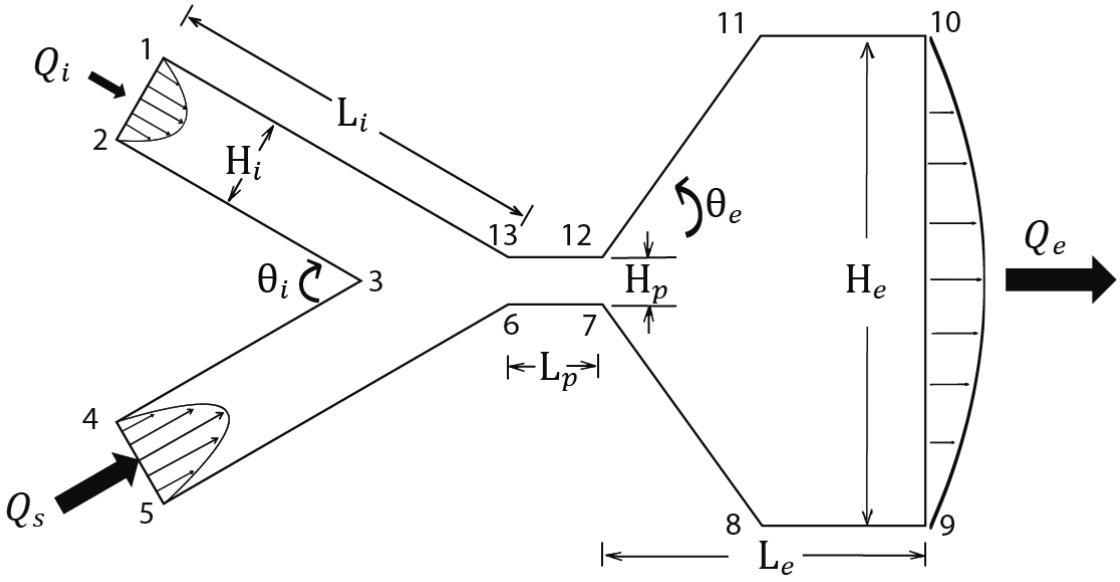

Figure 4.1 Idealized (not to scale) representation of a pinched-flow fractionation device. Schematic shows two inlet channels (left side), pinch region (mid diagram), and the exit area (right side). Vertices are shown, and are numbered clockwise starting from the upper-inlet channel. Inlet flow rates (Q_i , Q_s) and exit flux ($Q_e = Q_i + Q_s$) are illustrated to include Poiseuille flow profiles. The angle described by the bifurcation of the two input channels is noted by θ_i, while the exit angle from the pinch region is represented by θ_e. Dimensions of the device are represented by L (length of inlet channel), L_p (length of pinch area), L_e (length of exit channel), H_i(height of inlet channel), H_p (height of pinch area), and H_e (height of exit area).

Pinched-flow fractionation has previously been demonstrated in a microchannel device as a way to separate microparticles by size with continuous flow.[22] Targeted applications include size determination of air-borne particles,[23] marine-sediment measurement, and whole-blood separation.[24,25] Channel geometry, particle size, fluid transport and volumetric flow ratio of input-channel fluids all are known to affect the trajectories of particle motion through the device. Andersen *et al.*[26] recently developed a model based on the laminar velocity profile in a rectangular channel[27] assuming that particles leave the top corner of the pinch and follow the fluid streamlines into different exit or drain channels depending on particle size. This model gave better agreement with experiments than previous models. However, rather than simply understanding only the idealized separation behavior, it is important to determine the conditions under which particles actually reach the top of the pinch and the degree to which hydrodynamic interactions with the walls and corners affect the trajectories. Systematic studies of the hydrodynamic, particle-wall and particle-corner interactions that produce the pinched-flow fractionation effects have only recently been developed, using a moving-frame, boundary-integral method (BIM) to describe the particle trajectories.[28]

In the current work, the moving-frame BIM is used to simulate the trajectories of the particles as they are transported through the PFF device. The effects related to drag of the distant walls perpendicular to the channel walls shown in Figure 4.1 are neglected, which is valid for large aspect ratios and allows for a reduction in the dimensionality of the calculations required to build a model. BIM has the advantage of further reducing the dimensionality of the model, as implementation only requires integration at the particle and device surfaces. Limiting the discretization to these surfaces reduces the computational requirements when compared to other methods such as finite-difference, volume-of-fluid, or finite-element methods. The ability to

optimize application-specific operation based on information obtained from BIM simulations alleviates the need for fabricating multiple device configurations. We use this BIM to design a device with favorable separation characteristics, which was subsequently used to perform experiments and compare with the model predictions.

4.2 Simulation Method

4.2.1 Boundary-integral Method Formulation

Our approach uses a moving-frame, completed-double-layer, boundary-integral method (CDL-BIM) developed for use in channels where the surfaces of particles and walls affecting particle movement are discretized. The method used for the derivation for the CDL-BIM builds on the work of Pozrikidis,[29] Ladyzhenskaya,[30] and Kim and Karilla.[31] Complex channel geometries and lubrication effects between the particle and channel wall when in close proximity present computational challenges for numerical simulations. To address the computational difficulties, a 'moving-frame boundary-integral method'[28] was developed, to provide a solution where the computational domain changes while a particle moves through the complex channel. The problem is formulated as a CDL-BIM equation for the surface potential, with the fluid velocity on the cell boundary taken from the 2D solution for fluid-flow only, and solved iteratively at each time step. The method is outlined here, and the details are provided in Zinchenko *et al.* [28]

The moving-frame, boundary-integral method is systematically used to study the effects of particle radius, the ratio of flow rates, and the channel geometry on particle trajectories and the efficiency of size segregation. Using a two-step approach, a 2D model of the fluid transport through the channel with no particles is first determined using BIM. A sphere is then placed within the fluid-only, 2D flow field, and the trajectory of the sphere is determined using the 3D,

moving-frame BIM. Our BIM calculations are used to determine when there is a significant difference between particle trajectories and the fluid streamlines, and to predict the critical conditions for complete separation of particles of different sizes along with the degree of separation when operated under subcritical conditions. The approach is quite general for various microchannel geometries, consisting of an arbitrary number of rectangular panels and is not limited to spherical particles.

For microfluidic applications with small Reynolds numbers, inertia may be neglected, so that creeping or Stokes flow may be assumed. Since the Stokes equations are linear, the differential equations of motion may be converted to integral equations over the domain surface.

The velocity $\boldsymbol{u}_\infty$ for fluid-only flow in the device channel is calculated first. Poiseuille flow profiles are assumed. Once determined, the velocity $\boldsymbol{u}_\infty$ serves as the outer boundary condition used to solve the 3D problem, where particles are being transported in the fluid. The boundary-integral equation for the fluid-only velocity is [28]

$$\boldsymbol{u}_\infty(\boldsymbol{y}) = 2\sum_{i=1}^{m} \int_{\mathcal{L}_i} \boldsymbol{q}_\infty(\boldsymbol{x}) \cdot \boldsymbol{\tau}^{2D}(\boldsymbol{x}-\boldsymbol{y}) \cdot \boldsymbol{n}(\boldsymbol{x}) dS_{\boldsymbol{x}}, \tag{4.1}$$

where $\boldsymbol{q}_\infty$ is a yet-unknown potential density, m is the number of panels or contours, $\boldsymbol{n}(\boldsymbol{x})$ is the outward unit normal to the contour $\mathcal{L}$ (representing the different panels in Figure 4.1), dS_x is the length element, $\boldsymbol{\tau}^{2D}$ is the fundamental stresslet:

$$\boldsymbol{\tau}^{2D}(\boldsymbol{r}) = \frac{1}{\pi}\frac{\boldsymbol{rrr}}{r^4}, \tag{4.2}$$

in the 2D environment, $\boldsymbol{r} = \boldsymbol{x} - \boldsymbol{y}$ is the vector from the reference point to the integration point, and $\mathcal{L}_i = \mathcal{L}_1, \mathcal{L}_2, \ldots$are the line segments representing the channel boundary as shown in Figure 4.1

(i.e. $\mathcal{L}_1$ is the line segment from vertex 1 to vertex 2, etc.). Parabolic velocity profiles for $\boldsymbol{u}_\infty(\boldsymbol{y})$ are assumed on the entrances and exit, and $\boldsymbol{u}_\infty = \mathbf{0}$ on the walls due to the no-slip condition. A database is generated using equation (4.1) for a set channel geometry and flow ratio Q_s/Q_i.

The motion of fluid within the channel requires determination of the density function, $\boldsymbol{q}_\infty(\boldsymbol{x})$, which varies over the device surface. The integral equation for $\boldsymbol{q}_\infty(\boldsymbol{x})$ is transformed by way of Wielandt's deflation.[32] The potential density, $\boldsymbol{q}_\infty(\boldsymbol{x})$, is then expressed in terms of a new unknown, $\tilde{\boldsymbol{q}}_\infty(\boldsymbol{x})$:

$$\boldsymbol{q}_\infty(\boldsymbol{x}) = \tilde{\boldsymbol{q}}_\infty(\boldsymbol{x}) - \frac{1}{2}\tilde{\boldsymbol{q}}'_\infty(\boldsymbol{x}), \tag{4.3}$$

where $\tilde{\boldsymbol{q}}'_\infty(\boldsymbol{x})$ is a 'rigid-body' projection of $\tilde{\boldsymbol{q}}_\infty(\boldsymbol{x})$. Integration of equation (4.1), as y$\rightarrow \mathcal{L}$ (the inner contour wall), provides an expression used to calculate the 2D density function:[28]

$$\tilde{\boldsymbol{q}}_\infty(\boldsymbol{y}) = \boldsymbol{u}^b(\boldsymbol{y}) - 2\int_{\mathcal{L}} \tilde{\boldsymbol{q}}_\infty(\boldsymbol{x})\cdot\boldsymbol{\tau}^{2D}(\boldsymbol{r})\cdot\boldsymbol{n}(\boldsymbol{x})dS_x + \tilde{\boldsymbol{q}}'_\infty(\boldsymbol{y}) - \frac{\boldsymbol{n}(\boldsymbol{y})}{L}\int_{\mathcal{L}} \tilde{\boldsymbol{q}}_\infty(\boldsymbol{x})\cdot\boldsymbol{n}(\boldsymbol{x})dS_x, \tag{4.4}$$

where $\mathcal{L}_m$ is the overall channel contour and L is its length. Derivation of the double-layer contribution to the line segment $\mathcal{L}_i$ provides the 2D density function [28] as

$$\int_{\mathcal{L}_i} \tilde{\boldsymbol{q}}_\infty(\boldsymbol{x})\cdot\boldsymbol{\tau}^{2D}(\boldsymbol{r})\cdot\boldsymbol{n}(\boldsymbol{x})dS_x = \int_{\mathcal{L}_i} [\tilde{\boldsymbol{q}}_\infty(\boldsymbol{x}) - \tilde{\boldsymbol{q}}(\boldsymbol{x}^*)]\cdot\boldsymbol{\tau}^{2D}(\boldsymbol{r})\cdot\boldsymbol{n}(\boldsymbol{x})dS_x + \tilde{\boldsymbol{q}}(\boldsymbol{x}^*)\cdot\int_{\mathcal{L}_i} \boldsymbol{\tau}^{2D}(\boldsymbol{r})\cdot\boldsymbol{n}(\boldsymbol{x})dS_x, \tag{4.5}$$

where $\boldsymbol{x}^* = \boldsymbol{x}^*(\boldsymbol{y}_i)$, with the position $\boldsymbol{y}_i$ being closest to the mesh node $\boldsymbol{x}_j$ on line segment $\mathcal{L}_i$. This equation has a unique solution that is determined by iterative methods.

Once $\boldsymbol{u}_\infty(\boldsymbol{y})$ for fluid-only flow is determined, the 3D boundary-integral equations are used to provide the translational and rotational velocities of a particle placed in this flow, and a moving-frame BIM as described by Zinchenko *et al.*[28] is employed. The fluid velocity inside the cell in terms of double-layer velocity contributions from the cell and particle surface is given by:[28]

$$\boldsymbol{u}(\boldsymbol{y})=\boldsymbol{u}_\infty(\boldsymbol{y})+2\int_{S_c+S_p}\boldsymbol{q}(\boldsymbol{x})\cdot\boldsymbol{\tau}^{3D}(\boldsymbol{r})\cdot\boldsymbol{n}(\boldsymbol{x})dS_x, \tag{4.6}$$

where $\boldsymbol{u}(\boldsymbol{y})$ is the fluid velocity, $\boldsymbol{q}(\boldsymbol{x})$ is a yet-unknown potential density, $\boldsymbol{\tau}^{3D}(\boldsymbol{r})$ is the 3D fundamental stresslet, S_p is the particle surface, and S_c is the surface of the cell, which is composed of flat panels making up the cell boundary. The 3D fundamental stresslet is given by

$$\boldsymbol{\tau}^{3D}(\boldsymbol{r})=\frac{3}{4\pi}\frac{\boldsymbol{rrr}}{r^5}\quad . \tag{4.7}$$

The density function $\boldsymbol{q}(\boldsymbol{x})$ on the cell surface S_c is provided by

$$\boldsymbol{q}(\boldsymbol{y})=-2\int_{S_c+S_p}\boldsymbol{q}(\boldsymbol{x})\cdot\boldsymbol{\tau}^{3D}(\boldsymbol{r})\cdot\boldsymbol{n}(\boldsymbol{x})dS_x \quad \text{for} \quad \boldsymbol{y}\in S_c\quad . \tag{4.8}$$

For rigid-body motion, we choose

$$\boldsymbol{q}'(y)=\boldsymbol{V}+\boldsymbol{\Omega}\times(\boldsymbol{y}-\boldsymbol{x}_c), \tag{4.9}$$

which is added to $\boldsymbol{q}(\boldsymbol{y})$ on the cell boundary to make the total flux through S_c equal to zero, as shown by[28]

$$\boldsymbol{q}(\boldsymbol{y})=\boldsymbol{u}_\infty(\boldsymbol{y})-\boldsymbol{V}-\boldsymbol{\Omega}\times(\boldsymbol{y}-\boldsymbol{x}_c)+2\int_{S_c+S_p}\boldsymbol{q}(\boldsymbol{x})\cdot\boldsymbol{\tau}^{3D}(\boldsymbol{r})\cdot\boldsymbol{n}(\boldsymbol{x})dS_x \quad \text{for} \quad \boldsymbol{y}\in S_p, \tag{4.10}$$

with $\boldsymbol{V}$ and $\boldsymbol{\Omega}$ being the particle translational and rotational velocities, respectively, which are determined from equation (4.9). The surface centroid about which the angular velocity $\boldsymbol{\Omega}$ of the particle takes place, is described by

$$\boldsymbol{x}_c = \frac{1}{S_p} \int_{S_p} \boldsymbol{x}\, dS \,. \tag{4.11}$$

In the moving-frame BIM, a computation cell encloses the particle at each instant of time, and the fluid velocity on the cell boundary is given by the 2D solution for fluid-only flow. Thus, the cell boundaries that cut through the fluid must be at least several radii from the particle. Figure 4.2 illustrates the use of cell constructs surrounding the sphere for the moving-boundary BIM. The trajectory of the particle is created by sequentially determining the particle velocity and location within each cell.

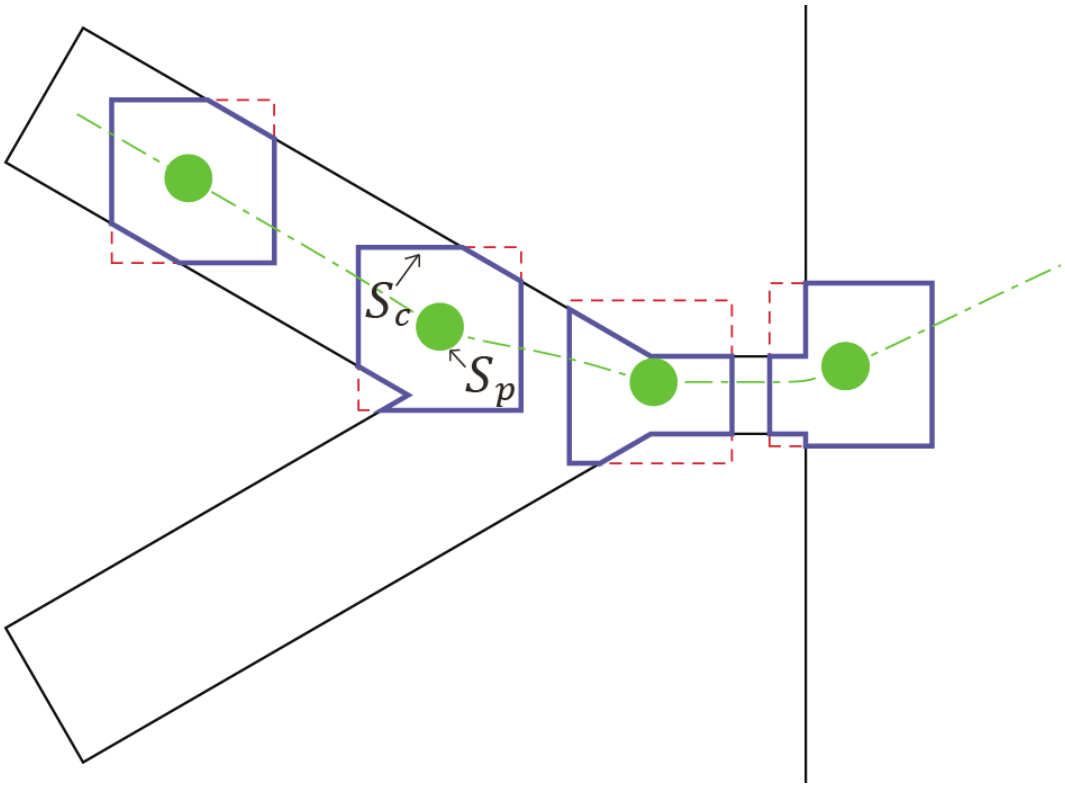

Figure 4.2 Schematic showing a succession of four computational cells as a particle moves through the PFF device. The trajectory of the particle is designated by the green dash-dot curve, and the cell boundaries shown by bold, blue lines. The red dashed lines represent the portions of the square frames that are outside the PFF domain and hence, not analyzed. The frames are in fact cubes, with additional sides above and below and parallel to the plane of the illustration.

4.2.2 Numerical Considerations

The numerical solution of the boundary-integral equations requires discretization of the channel and particle surfaces. A meshing bias is used to increase computational efficiency, with the panels for the inlet channels and pinch area having a greater number of meshing units per length of contour than those in the exit portion of the device. For the 2D solution for fluid only, the inlet, pinch and exit panels of the overall channel are divided into increments with lengths made dimensionless by the pinch height, H_p. A greater emphasis is given to the inlet and pinch segments, as shown in Table 4.1 for a typical case.

Channel region	Panel	Panel length	Number of Increments
Pinch	$\mathcal{L}_6, \mathcal{L}_{12}$	$2H_p$	500
Inlet	$\mathcal{L}_1$	$2H_p$	500
	$\mathcal{L}_2$	$6H_p$	1500
	$\mathcal{L}_{12}$	$8.46H_p$	2115
Sweep	$\mathcal{L}_4$	$2H_p$	500
	$\mathcal{L}_3$	$6H_p$	1500
	$\mathcal{L}_5$	$8.46H_p$	2115
Exit	$\mathcal{L}_7$	$9.5H_p$	1781
	$\mathcal{L}_8$	$30H_p$	5625
	$\mathcal{L}_9$	$20H_p$	3750
	$\mathcal{L}_{10}$	$30H_p$	5625
	$\mathcal{L}_{11}$	$9.5H_p$	1781

Table 4.1 Table showing a typical meshing for the PFF device by region. The panels correspond to the first vertex number of each panel, moving counter-clockwise about the channel, beginning with vertex 1 (shown in Figure 4.1). The increment length is the panel length divided by the number of increments.

Six different geometries of the PFF device were considered in the simulations:

(i) Base geometry: For the base case, which corresponds to the dimensions in Table 4.1, $H_i = 2H_p$, $L_i = 8.46H_p$, $\theta_i = 60°$, $L_p = 2H_p$, $H_e = 20H_p$, $L_e = 40H_p$ and $\theta_e = 90°$.

(ii) Angled exit: For this case, the geometry is the same as the base case, except $\theta_e = 45°$.

(iii) Elongated pinch: For this case, the geometry is the same as the base case, except $L_p = 4H_p$.

(iv) Narrow inlet: For this case, the geometry is the same as the base case, except $H_i = H_p$.

(v) Wing geometry: For this case, the geometry is the same as base case, except $\theta_e = 135°$.

(vi) Beveled exit corner: For this case, the geometry is the same as base case, except the sharp corner at the exit of the pinch is replaced with a 45° beveled edge.

To simulate particle trajectories, a 3D particle is placed in the 2D, fluid-only environment. For the cell wall, the mesh was generated using the gap-adaptive surface discretization as described by Zinchenko et al.[28] The surface of the particle is meshed, using N_Δ triangles as shown in Figure 4.3. Meshing of the particle surfaces for the BIM is based on providing acceptable numerical accuracy for simulations within computational limits. We found that N_Δ = 3840 was sufficient to give results that converged to within 0.05%. All of the calculations for this work used uniform meshing for the spheres, though a future improvement might be to use an adaptive mesh with greater refinement in areas where the sphere is close to the wall.

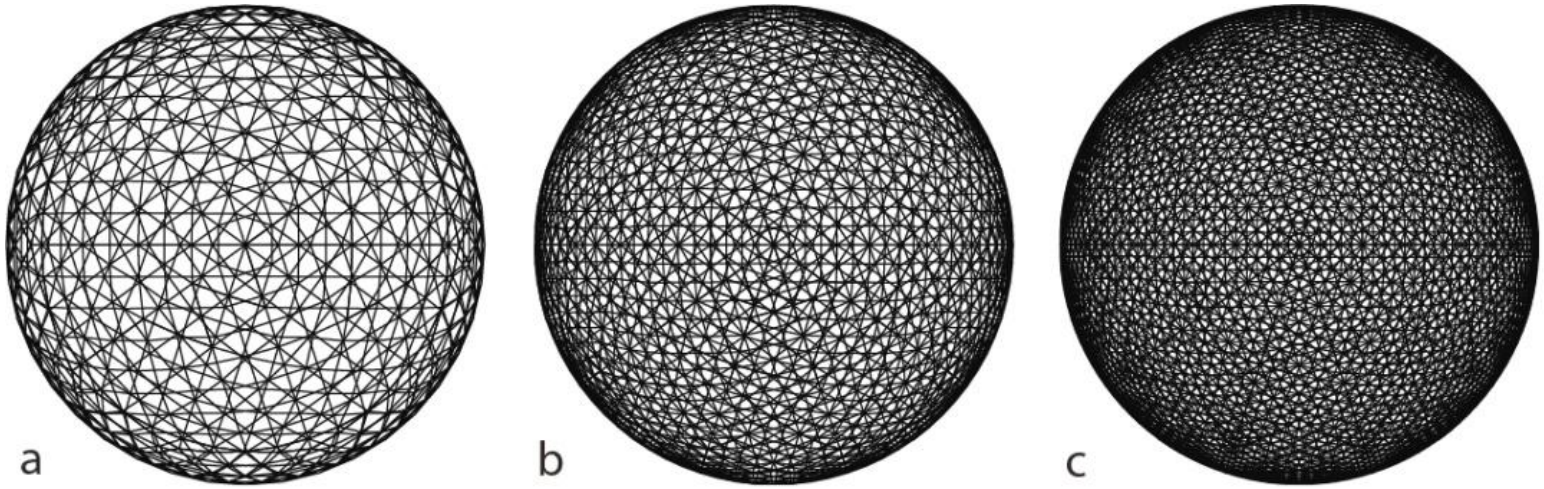

Figure 4.3 Sample uniform mesh using triangulations with $N_{\Delta} =$ (a) 240, (b) 3480 and (c) 8640. Meshing is uniform and independent of location on the sphere.

All numerical calculations were generated using single-core (logical) calculations with an Intel Core 975 CPU (4.2 GHz) using PGI accelerator Visual Fortran, release 11.5.

4.3 Experimental methods and materials

4.3.1 Microchannel device fabrication

A photopolymerizable thiol-ene based resin was used to fabricate the pinched-flow fractionation device. The aromatic urethane diacrylate (Ebecryl 4827) was donated by Cytec Surface Specialties (Smyrna, GA), and pentaerythritol tetra(3-mercaptoproprionate (PETMP) was donated by Evans Chemetics (Waterloo, NY). Triallyl- 1,3,5- triazine 2,4,6 trione (TATATO) was purchased from Sigma-Aldrich (Milwaukee, WI). The inhibitor, N-nitrosophenyl-hydroxylamine (Q1301), was donated by Wako Pure Chemicals (Osaka, Japan). The initiator, Irgacure 651, was donated by Ciba Specialty Chemicals (Tarrytown, NY). All materials were used as received without additional purification.

The previously-developed, soft-lithography fabrication method known as contact liquid photolithographic polymerization (CLiPP)[32,33] was employed to produce the device. A modified, one-step 'sandwich' method (Figure 4.4) was used to fabricate channels with narrow channel features (< 100 μm width). Glass cover slides were cleaned by etching with a solution consisting of one part hydrogen peroxide and three parts sulfuric acid for 3 hours. The slides were then washed with deionized water and acetone. After cleaning, the slides were coated with methacryloxypropyl-trimethoxysilane (MPS) (Gelest, Morrisville, Pa.) by surface-layer deposition, which involved placing the cleaned cover slides with 3 ml of MPS inside a sealed Teflon container. The Teflon container was placed inside an oven and heated to 70° C for 4 hours. Subsequently, the monomer formulation was injected between the two treated glass cover slides, with a photolithographic mask attached to the surface. Masks were created with feature

resolution of 30 μm (printed masks), and the masks were used to fabricate the PFF channel geometries. The monomer was exposed to a collimated light source from an optical mask alignment system (Optical Associates, Inc. San Jose, Ca) using a 5 x 5 cm area collimated flood exposure source with irradiation intensity of 37.5 mW/cm^2 with principal output at 365 nm. Irradiation intensities were measured using an International Light, model IL1400A radiometer (Newburyport, Ma.). Following the cure process, uncured monomer was removed by flushing the channels with methanol followed by removal of excess solvents and monomer, leaving only the photopatterned, crosslinked polymer device.

Cure time for the device was determined using a method developed to optimize feature fidelity.[34] For a device having a pinch height of 1 mm and width of 4 mm, an optimal cure time of 37 seconds was used with a 37.5 mw/cm^2 light source.

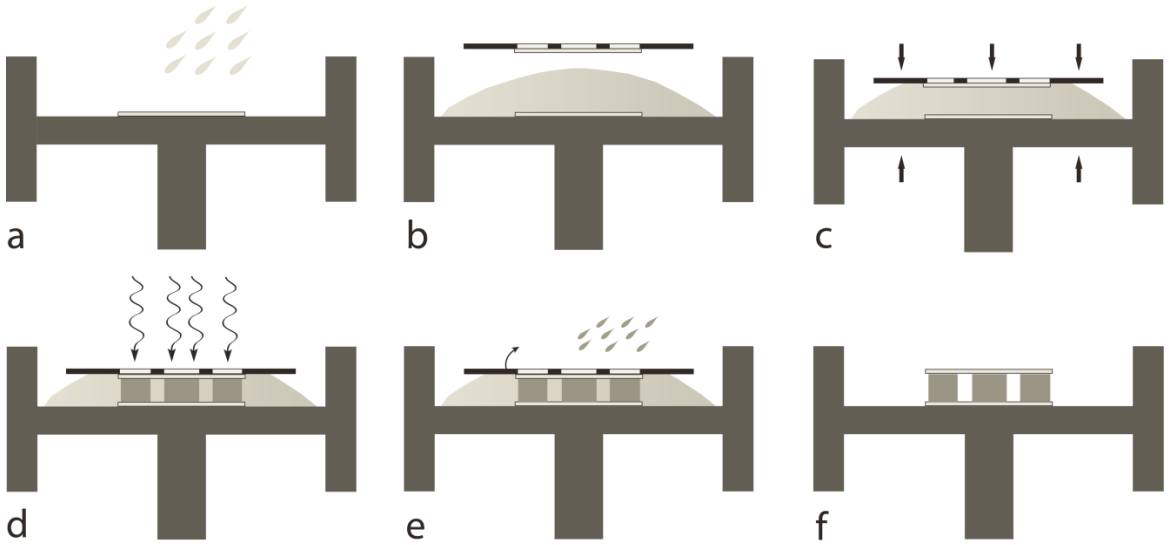

Figure 4.4 Schematic of CLiPP process. Step a: The siloxane-treated glass slide is secured to the chamber base. A monomer mixture fills the chamber. Step b: After filling the chamber with monomer, an aligned mask (top) is joined with a siloxane-treated glass slide and placed over the monomer. Step c: The siloxane-treated glass slide is brought in contact with the monomer and lowered to the desired feature height. Step d: The monomer mixture is exposed to 365 nm UV radiation through the aligned mask. Step e: The mask is removed from glass slide. Step f: Excess, uncured monomer is removed by washing with solvent. After washing, only the substrate, top glass slide and pinched-flow fractionation device remain.

A single pinched-flow geometry was constructed, with channel dimensions of H_p = 1 mm, L_p = $2H_p$, $H_i = 2H_p$ $L_i = 8.46H_p$, $H_e = 20H_p$, $L_e = 40H_p$, $\theta_i = 60°$, and $\theta_e = 90°$. The width or depth of the channels in the direction perpendicular to the plane of Figure 4.1 is $W = 4$ mm. This size is larger than those used for typical microfluidic devices, to provide ease of visualization and to reduce the effects of surface roughness. Appropriately larger size particles were used to preserve the desired pinch height to particle size ratio.

4.3.2 Particle Tracking

Polystyrene particles (Polysciences Inc., Warrington, PA) with diameters in the range $200 \leq 2a \leq 500$ μm were analyzed and separated in the PFF device. The particle density is 1.05 g/cm^3, and the particles were suspended in a fluid consisting of 22 weight percent glycerol in water, with a fluid density matching that of the particles. The viscosity of the mixture was 0.017 g/(cm·s) at the ambient temperature of 23 ± 1° C. Two polystyrene bead sizes ($\eta = 2a/H_p = 0.25$ and 0.5, respectively) were suspended in the inlet solution. Dilute concentrations of 10 spheres per ml of solution were created by mixing the polystyrene beads with the water/glycerol solution for 20 minutes, so that individual spheres could be tracked without particle-particle interactions, as simulated by the model. Volumetric flow rates for the sweep stream were varied from 5 to 15 ml/min, with flow ratios ranging from 2 to 35.

Tracking of the particles during transport was accomplished using an experimental setup as shown in Figure 4.5. A pump controller (Bee Hive; Bioanalytical Systems (BAS), Inc.) was used to control the volumetric flow rates from two disposable 5-ml syringes (Becton-Dickinson, Franklin Lakes, NJ). Each syringe was placed onto a syringe drive (Baby Bee; BAS, Inc., West Lafayette, IN), connected to the pump controller by an RJ-45 cable. The Bee pump control system provided independent control of the fluid-only sweep stream (Q_s), and the fluid/particle

mixture inlet stream (Q_i) flow rates. Flow rates were set using a variable knob-adjustment controlling the rate of fluid injection of each 5-ml syringe. Tygon tubing with 3/32" OD was joined to the syringe using a Luer-lock connection. The tygon tubing was connected to an 18-gauge needle using an additional Luer-lock connection. Calibration of the syringe pumps was carried out by measuring the volumes of fluid collected for time periods of 5, 10 and 20 minutes, which showed consistent delivery over time.

The PFF device was mounted onto the stage of a Nikon TE300 microscope (Nikon TE300, Melville, NY). The microscope objective (4X, Nikon Achromat, NA 0.10, WD 30) faced upward, toward the PFF. Digital imaging and data collection were carried out using a video camera (KP-M2, Hitachi Corporation, Chula Vista, CA) with 2X intermediate magnification. Data analysis was accomplished using Metamorph imaging software (Universal Imaging Systems, Downington, PA).

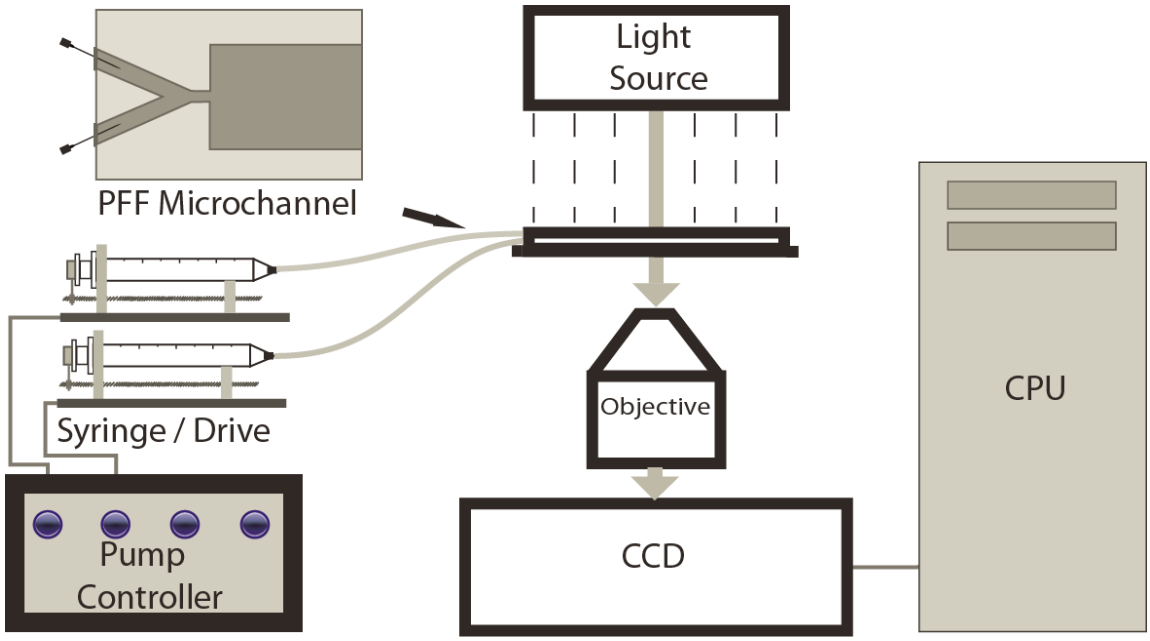

Figure 4.5 Schematic of experimental setup used to track particle trajectories. A top view of the PFF device is shown in the upper left corner. Two syringes provide fluid and fluid/particle suspension injected into separate inlet channels of the PFF device. Syringe injection is controlled by a pump controller (lower left-hand corner). The PFF microchannel is fixed to a microscope stage below a light source and above the microscope objective (middle of figure). Images of particle movement are captured by a video camera and transmitted to a PC (right side).

4.4 Simulation Results and Discussion

4.4.1 Example Fluid Streamlines

2D examples of the simulation for fluid-only streamlines in the PFF using BIM are provided in Figure 4.6, which shows the pinch and adjacent areas of the pinched-flow fractionation device, for flow ratios of Q_s/Q_i = 2.0, 6.0 and 10.0. At a flow ratio of 2.0, as shown in Figure 4.6a, the streamlines originating from the upper, inlet stream are compressed less in the pinch area than those with higher flow ratios. Thus, it is expected that higher flow ratios will give better particle separation due to steric hindrance as particles of different sizes are pressed against the top wall of the pinch region. On the other hand, high flow ratios may be undesirable due to dilution of the particle stream, and so optimal conditions to obtain the desired separation at the lowest possible flow ratios are sought.

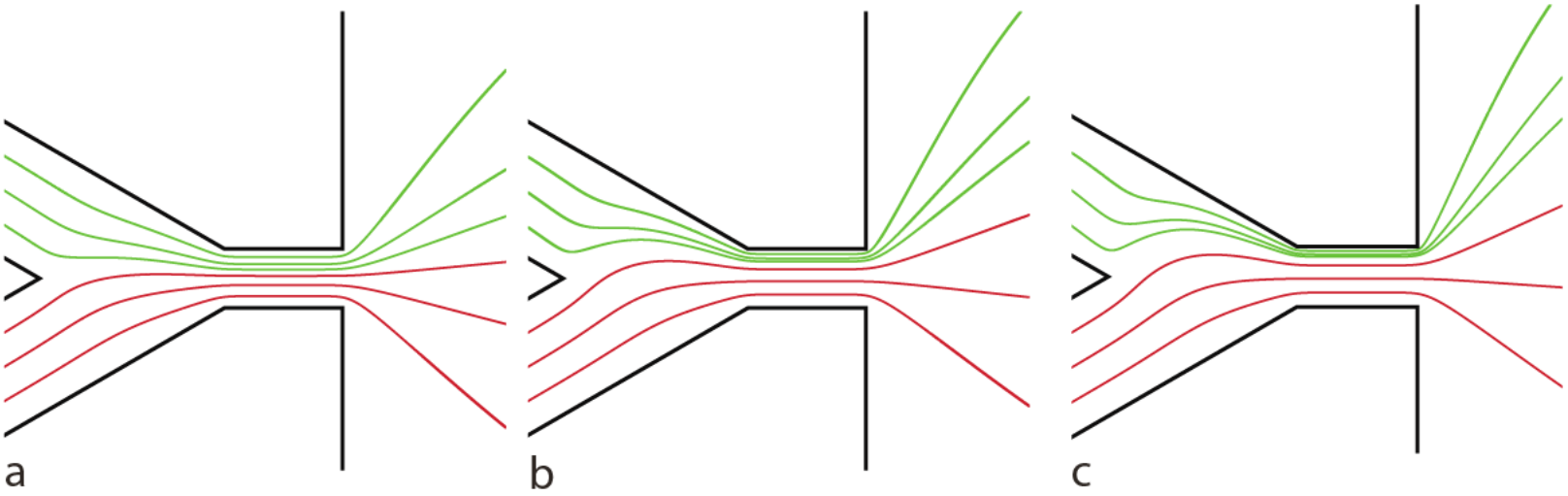

Figure 4.6 Inlet and pinch areas of a pinched-flow fractionation device showing fluid-only streamlines for Q_s/Q_i = 2.0, 6.0 and 10.0 (left to right). The device geometry uses the base case, where $H_i = 2H_p$.

4.4.2 Example Particle Trajectories

Figure 4.7 shows example particle trajectories from the BIM simulations that demonstrate the separation of particles by size. In this example, all particles start at the center plane of the inlet channel. As expected, the smaller spheres move toward the upper portion of the exit area, while the larger particles move closer to the center of the exit area. Note that the smallest particles closely follow the fluid streamline, whereas the departure of the particle trajectories from the fluid streamline increases with particle size due to steric exclusion.

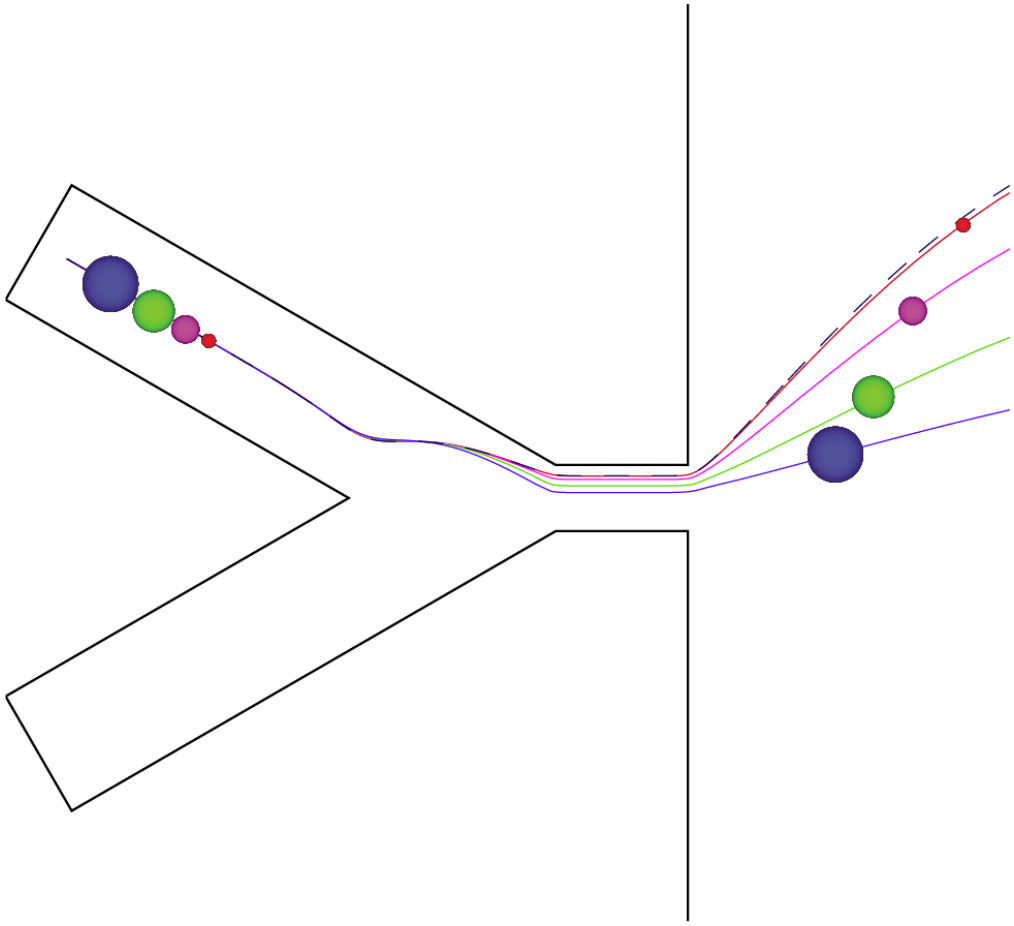

Figure 4.7 Trajectory paths for spheres entering along centerplane of the inlet channel, with flow ratio Q_s/Q_i = 6.0. Sphere sizes of η = 0.2 (●), 0.4 (●), 0.6 (●) and 0.8 (●) are included, and the fluid-only streamline (dashed line) is also shown. The device geometry uses the base case.

Figure 4.8 further illustrates particle separation by size. It shows the lateral exit positions of particles of different sizes that started at the inlet centerplane. As noted previously, the smallest particles exit on the highest trajectory because their centers are able to approach most closely to the upper wall of the pinch. As the flow ratio is increased, the smaller particles are pressed closer to the upper wall, and so exit at an even higher position, whereas the largest particles were already as close as allowed to the upper wall and so exit at the same position. Thus, separation improves with increasing flow ratio, until all particles are pressed as close as possible to the upper wall.

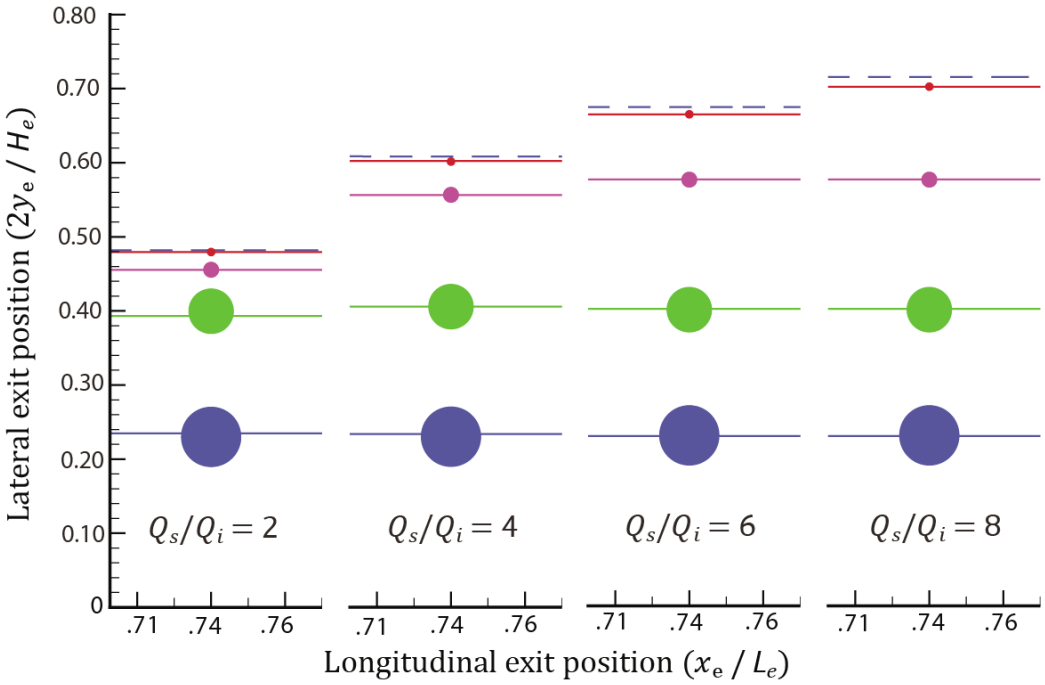

Figure 4.8 Lateral exit position distribution of particles starting at the inlet centerplane and with η = 0.2 (●), 0.4 (●), 0.6 (●), and 0.8 (●) for Q_s/Q_i = 2.0 (left), 4.0 (2nd), 6.0 (3rd) and 8.0 (right). The base geometry is used and all particles enter the inlet with particle centers located on the mid-plane. Lateral and longitudinal positions are normalized with respect to pinch height H_p. The dashed line shows the fluid-only streamline with the same starting position as the particles. Here, y_e is the vertical distance above the channel mid-plane, and x_e is the horizontal distance from the pinch exit.

4.4.3 Particle trajectory ‘banding’ and critical flow rate

The trajectories shown in the previous section are for particles starting on the inlet channel centerplane. However, in reality the particles will enter throughout the entire inlet channel with their centers ranging from one radius above the lower wall to one radius below the upper wall (plus any small surface roughness or other exclusion effect imposing a minimum surface clearance). Hence, a ‘band’ of trajectories is observed for each particle size. Such bands are shown in Figure 4.9 for two particle sizes. In general, the band is lower for the larger particles due to steric hindrance by the upper wall of the pinch. For the relatively low flow ratio of Q_s/Q_i = 3.385 in Figure 4.9 (left), the bands overlap in the exit region, illustrating incomplete separation. However, at the higher flow ratio of Q_s/Q_i = 6.0 in Figure 4.9 (right), the bands do not overlap and complete separation is predicted. Moreover, the larger particles shown in Figure 4.9 (right) all proceed through the exit on a single trajectory, because the sweep flow is sufficiently strong to press all of the larger particles to the upper wall of the pinch region.

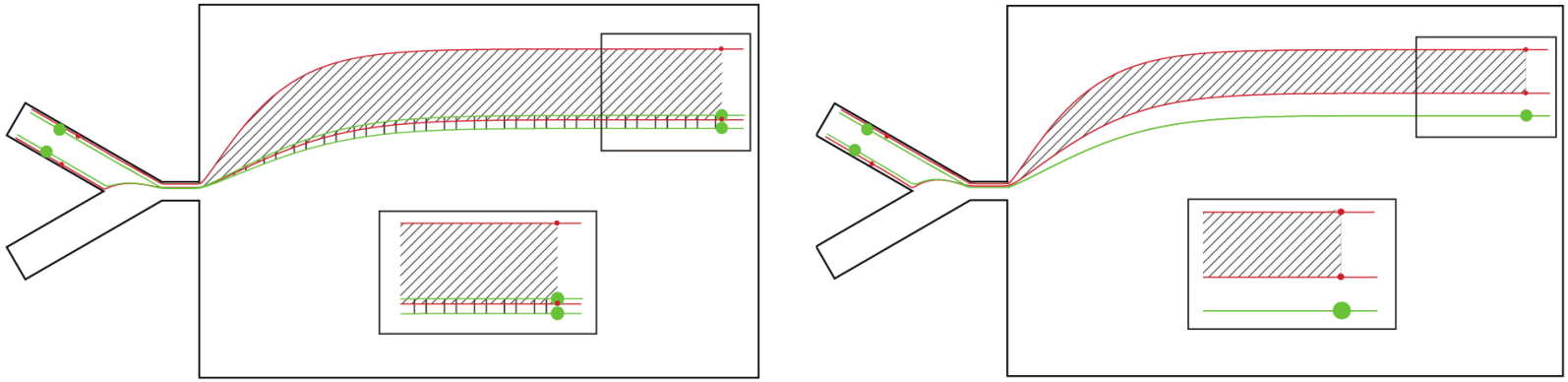

Figure 4.9 Banding effect illustrated, where spheres of two sizes, η = 0.2 (●) and 0.6 (●), enter near the top and bottom of the inlet channel at flow ratio = 3.385 (left) and 6.0 (right). Solid red and green lines indicate trajectories of the η = 0.2 and 0.6 spheres, respectively. At lower flow ratios, incomplete separation takes place, resulting in a 'band' of mixed spheres in the area marked by a mix of diagonal and vertical lines (as shown by inset on left), while at higher flow ratios, complete separation of particles takes place (as shown by inset on right). In each case, the inset shows an expanded view of the trajectory 'bands' exhibited by the spheres at a given flow ratio. For this illustration, the base-case geometry is used.

Figure 4.10 shows the lateral exit position versus inlet position. Here, $P = (y_i - a)/(H_i - 2a)$, where y_i is the initial distance of the particle center above the lower inlet wall. As noted previously, the smaller particles have higher exit locations, and the lateral exit location increases with increasing entrance location above the lower wall. Of particular interest is that a plateau is observed for each particle size, where the exit position becomes independent of the entrance position. The plateau occurs because all particles entering above a critical location come in contact with the upper wall of the pinch. The critical entrance location is determined by using 'backward' integration of the trajectory from particle contact with the corner (vertex 12 in Figure 4.1). The larger particles come in contact with the upper wall of the pinch at lower inlet positions due to greater steric exclusion. Similarly, the exit plateau occurs at lower inlet positions when the flow ratio is increased, since the particles are then more strongly pressed against the upper wall of the pinch region by the sweep fluid. At a high enough flow ratio and/or particle size, all particles of a given size reach the upper wall and exit on a single trajectory rather than within a band of trajectories, as shown for the larger particles in Figure 4.10.

An average lateral exit position at a fixed distance downstream from the pinch exit may be determined:

$$\langle y_e \rangle = \int_0^1 y_e(P_i)\, dP_i, \tag{4.12}$$

where it is assumed that all physically possible entry positions are equally probable. This average exit position is also shown in Figure 4.11, and it increases with decreasing particle size.

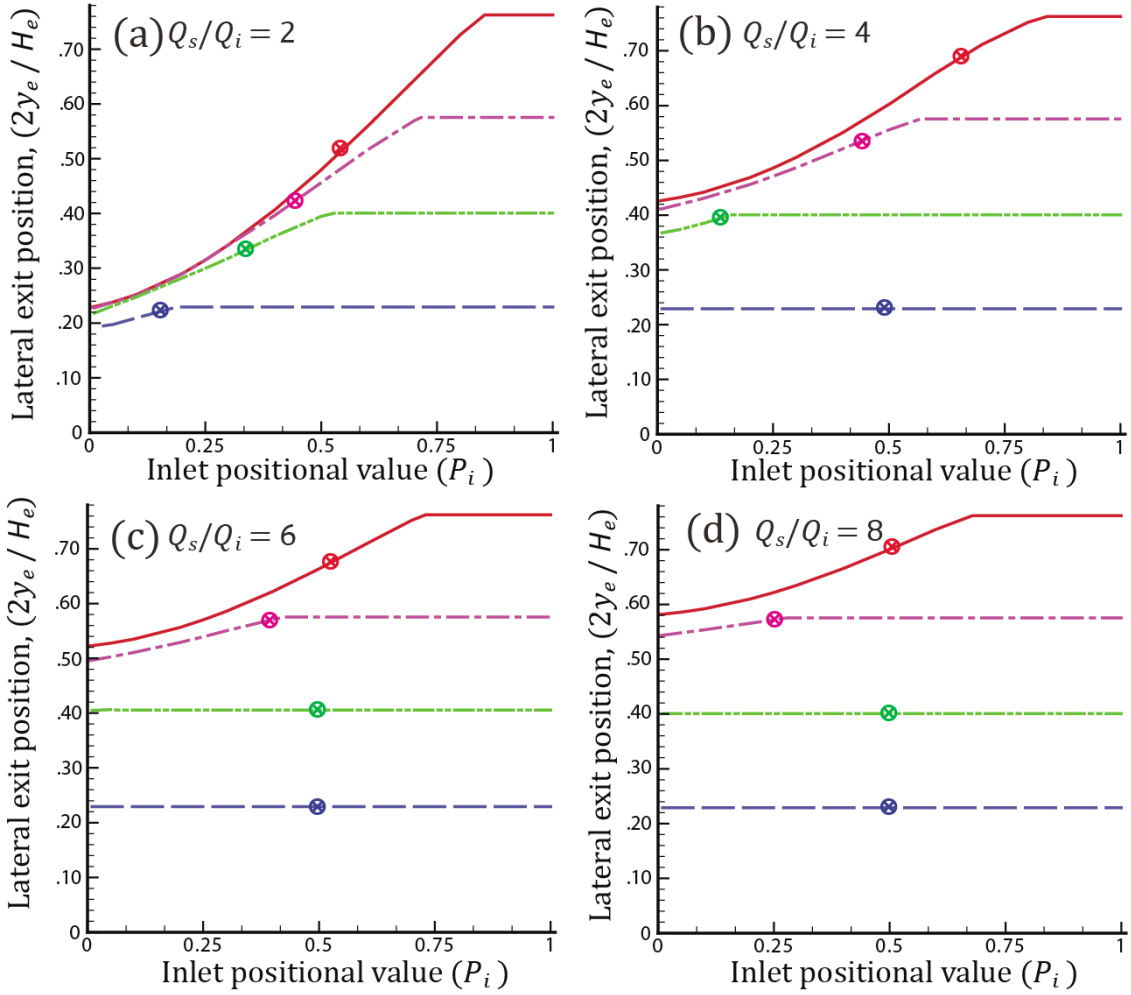

Figure 4.10 Exit position versus entrance position for particles of size $\eta = 2a/H_p$ = 0.2, 0.4, 0.6 and 0.8 (top to bottom) and flow ratios of Q_s/Q_i = (a) 2, (b) 4, (c) 6 and (d) 8. The average exit position, $< y_e >$, is denoted by ⊗**.** The device geometry uses the base case.

As evident from Figure 4.10, particles of a given size reach the upper wall of the pinch at sufficiently high inlet positions and flow ratios, and then depart at the same downstream trajectory from vertex 12. For a given particle size, there is a critical flow ratio, $(Q_s/Q_i)_c$, above which all particles reach the upper wall and depart on the same downstream trajectory, even if the particles enter near the bottom of the inlet channel. In Figure 4.11, this critical flow ratio is plotted versus particle size. The critical flow ratio decreases with increasing particle size, since the larger particles more easily reach the upper wall. These results have important practical value, because operation at the critical flow ratio, rather than a higher or lower value, for a given particle size ratio allows for those particles to be collected in a narrow exit drain with minimal dilution by the sweep fluid.

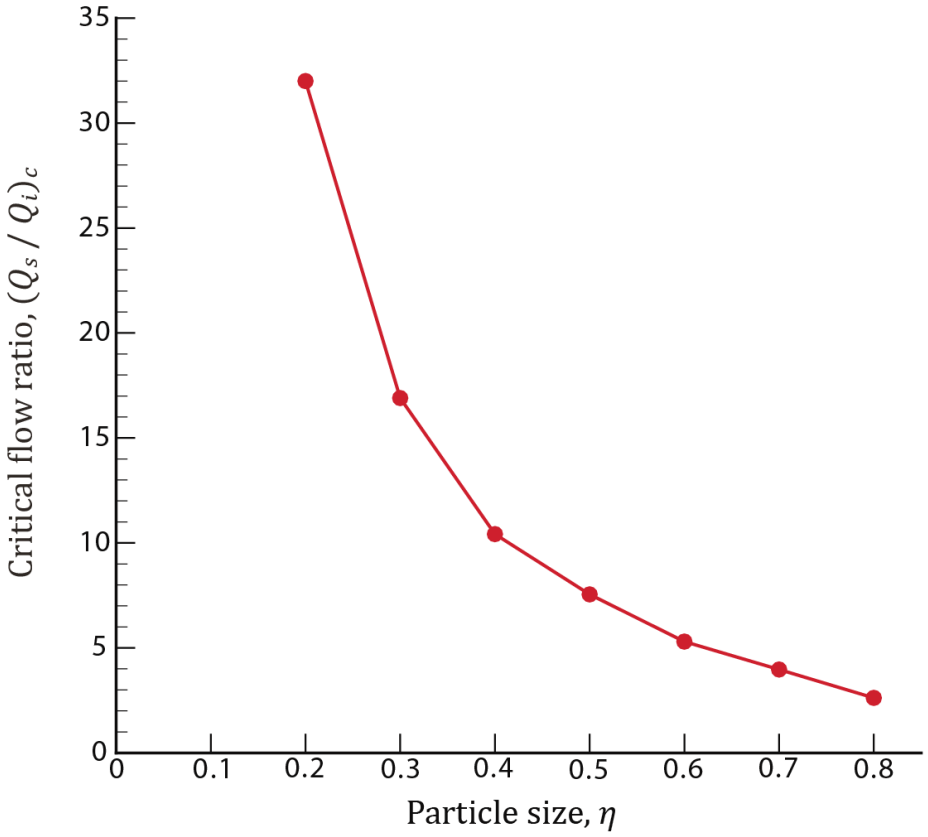

Figure 4.11 Critical flow ratio $(Q_s/Q_i)_c$ for a single exit trajectory versus dimensionless particle size $\eta = 2a/H_p$.

4.4.4 Corner Effects

Figure 4.12 illustrates the critical trajectory of a sphere with η = 0.6 as it comes in contact with the walls and corners of the pinch region. A minimum sphere-wall gap of $0.01a$ is used in this example, such as might be the case if there are surface roughness elements with heights of 1% of the particle radius, and it is assumed that the sphere comes into contact with the wall when this minimum gap is reached. Once the sphere comes in contact with a wall, it moves parallel to the wall until reaching a corner. The sphere then pivots about the corner until hydrodynamic forces pull it away from the corner. The 'departure' angle (relative to the normal from the wall), is where the sphere departs from the corner and is described by $\theta_{v,\mathrm{dep}}$, with v denoting the vertex number.

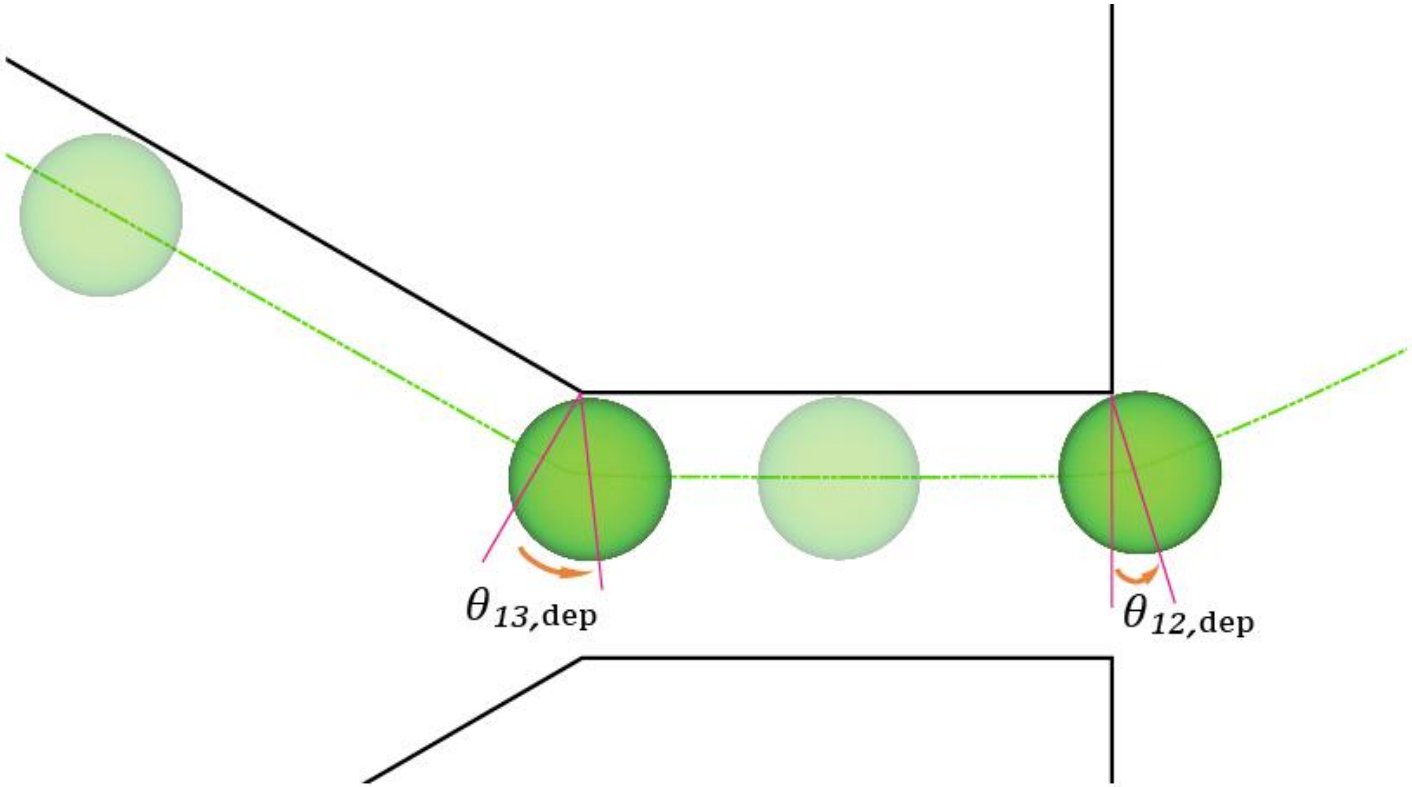

Figure 4.12 A η = 0.6 sphere at Q_s/Q_i = 3.86 coming into close contact with the upper walls and then pivoting about the entrance and exit corners of the pinch region. The departure angle, $\theta_{v,\mathrm{dep}}$, at which the sphere moves away from the corner, is illustrated. The trajectory path is shown by the curve.

Table 4.2 illustrates the relationship between the critical angle of spheres exiting the pinch, $\theta_{12,\text{dep}}$, to particle size. As particle size increases, so does the associated departure angle at the pinch exit, as the fluid streamlines and particle trajectories have less curvature further from the corner (see Figures 4.6 and 4.7). Values for $\theta_{12,dep}$ change very little with an increase or decrease in flow ratio, since the fluid flow is fully developed (i.e., independent of inlet conditions) by the pinch exit.

η	0.2	0.3	0.4	0.5	0.6	0.7	0.8
$\theta_{12,\mathrm{dep}}$	14.0°	18.0°	19.2°	22.5°	23.6°	24.6°	28.1°

Table 4.2 Table showing the variation of the departure angle with particle size at the pinch exit.

Figure 4.13 shows the trajectories of the spheres after they leave the corner at the pinch exit. For smaller spheres, the fluid-only streamline approximates the sphere trajectory. As the sphere radii increases, so does the trajectory deviate more from the fluid-only streamline. The fluid streamlines and particle trajectories are essentially independent of the flow ratio, because the flow is fully developed by the exit of the pinch and so independent of inlet conditions. Fluid-only streamlines are farther from the upper exit wall than the associated particle trajectory. Lubrication effects associated with particle-wall interactions result in a lag in release of the particle as they exit the pinch area, and the particle-wall interactions increase with particle size.

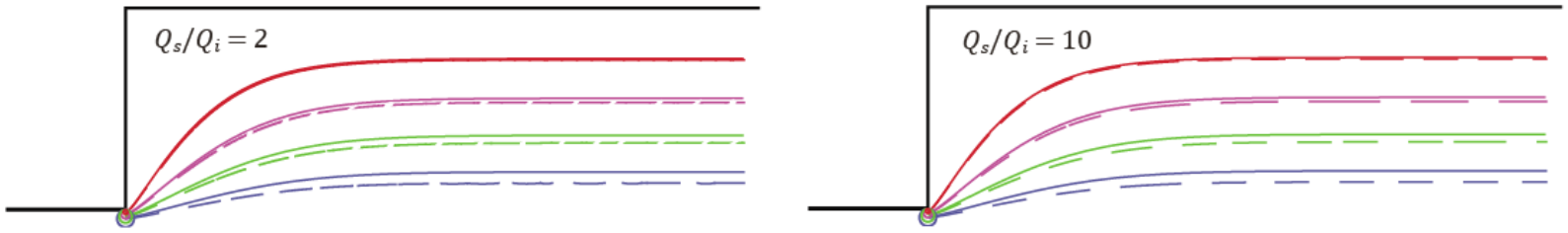

Figure 4.13 Comparison of particle trajectories (solid curves) to fluid-only streamlines (dashed curves) for particle sizes η = 0.2, 0.4, 0.6, and 0.8 (top to bottom), with Q_s/Q_i = 2.0 (left), and 10.0 (right). The fluid streamlines and particle trajectories originate at the exit of the pinch at a distance of 1.01a directly below the upper-corner of the pinch exit. The base geometry configuration is used for this illustration.

4.4.5 Particle Separation

As was seen in Figure 4.10, complete separation of two particle sizes may be achieved at sufficiently high flow ratios. We define the separation flow ratio, $(Q_s/Q_i)_s$, such that complete particle separation by size occurs above this value. Figure 4.14 illustrates conditions (a) below separation flow ratio, (b) at the separation flow ratio $Q_s/Q_i = 3.87$, and (c) above the separation flow ratio. At a flow ratio less than the separation flow ratio, mixing of the particle bands occurs, while at a flow ratio above the separation flow rate, complete separation occurs. The concept of 'banding' of exit trajectories based on the distribution of particles of a given size and entry position across the inlet channel provides the basis for determining the minimum flow ratio needed for complete separation of particles, $(Q_s/Q_i)_s$. As shown in Figure 4.14, we consider a larger particle that enters the inlet channel at $P_i = 0.99$ near the upper wall, representing the top of the band of larger particles. The smaller particle enters the inlet channel at $P_i = 0.01$ near the lower wall, representing the lower trajectory of the smaller particle band. Here, it is assumed that there is surface roughness or repulsion that prevents particles from being less than 1% of its radius from the wall. In Figure 4.14a, the smaller particle is below the larger particle in the exit, whereas it is above the larger particle in Figure 4.14c. In Figure 4.14b, where $Q_s/Q_i = (Q_s/Q_i)_s$, the lowest small particle and the highest large particle achieve the same exit position. The separation flow ratio was determined by the Newton-Rhapson iteration of the numerical results.

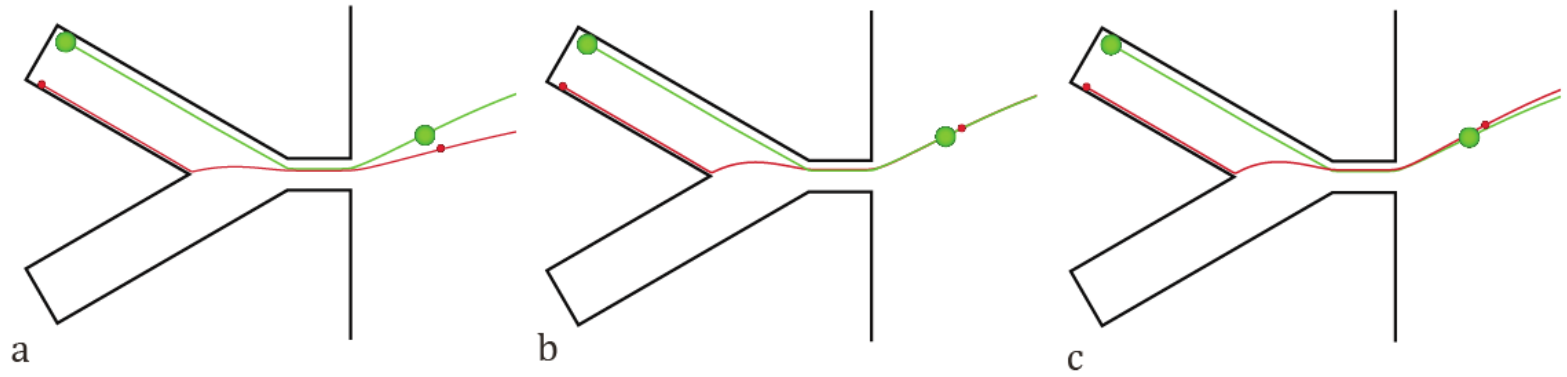

Figure 4.14 Effect of increased flow ratio on η = 0.2 (red) and η = 0.6 (green) particle trajectories, with (a) Q_s/Q_i = 3.64, (b) Q_s/Q_i = 3.87, and (c) Q_s/Q_i = 4.06.

Figure 4.15 gives the separation flow ratios for pairs of dimensionless particle sizes ranging from η = 0.2 to η = 0.8. The value of $(Q_s/Q_t)_s$ decreases with increasing size of the larger particle, because the exit trajectory is lowered due to steric exclusion when the size of the larger particle is increased, making it easier for smaller particles to cross the trajectory with a lower flow ratio. This result indicates that the pinch region should have a height that is slightly larger than that of the largest particles, to minimize the amount of sweep fluid used during operation. In contrast, $(Q_s/Q_t)_s$ increases weakly with an increase in the size of the smaller particle. The weak dependence on size of the smaller particle is due to the fact that its separation trajectory does not reach the pinch wall; hence, it does not have steric exclusion. However, there are hydrodynamic interactions between the particles and upper wall, which increase with the particle size and thereby require a slightly higher flow ratio to push all of the small particles above the highest large particle. An important finding from Figure 4.15 is that the separation flow ratio needed to achieve complete separation is less than the critical flow ratio (for all particles to reach the upper wall and depart on a single trajectory for each particle size - see Figure 4.11). This finding implies that less sweep fluid is required for complete separation than for the bands to collapse to single exit trajectories, but the exit drains must be larger to collect the particles from the bands rather than from single exit trajectories.

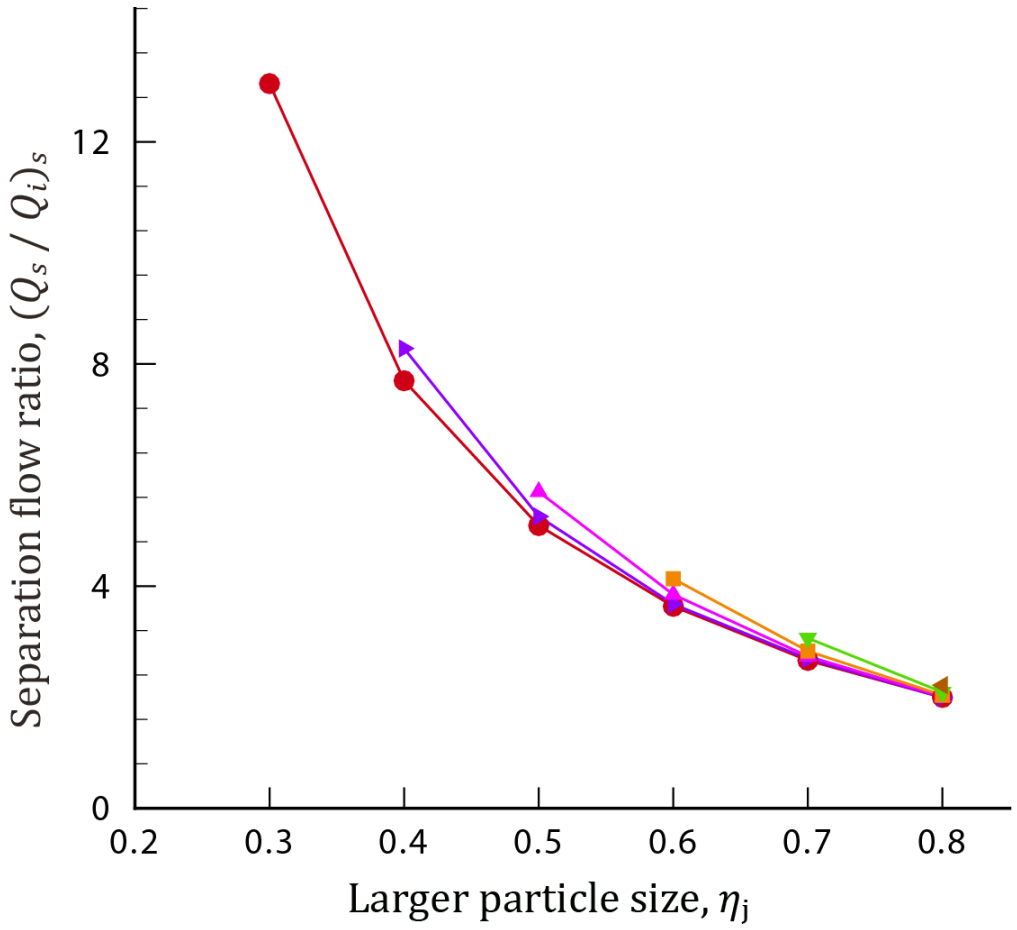

Figure 4.15 Separation flow ratio $(Q_s/Q_i)_s$ required for complete separation of smaller particles (η_i) from larger particles (η_j). The dimensionless sizes of the smaller particles are η_i = 0.2 (●), 0.3 (▶), 0.4 (▲), 0.5 (■), 0.6 (▼), and 0.7 (◀). The base geometry was used.

4.4.6 Channel geometry effects

To study the effects of channel geometry on particle trajectories and separation, changes were made to the inlet, pinch and outlet areas of the PFF geometry. Figure 4.16 shows the results from the simulations to determine the required separation flow rates from the different geometric configurations considered. Lengthening the pinch region or making the inlet channels more narrow (not shown) has only a small effect, which is not unexpected, given the results in Figures 4.6 and 4.7 showing that the fluid streamlines and particle trajectories become parallel to the channel walls almost immediately upon entering the pinch, so that the flow is fully developed at the pinch exit and independent of initial conditions. In contrast, an angled exit with $\theta_e = 90°$ gives poorer separation than does the base case, requiring larger flow ratios to achieve complete separation. The reduced performance is because the angled exit does not provide as much separation of the trajectories of particles of different sizes as they pivot around the corner (vertex 12) and leave the pinch region for the exit region. In particular, the angled wall is closer to the particles and causes resistance as they pull away from the corner, so that the particle trajectories are higher than the streamlines, as shown in Figure 4.17. This effect is greatest for the larger particles, reducing their separation from the smaller particles. Finally, the wing exit with $\theta_e = 135°$ has almost the same separation (Figure 4.16) as the base case, because the angled wall in this case has almost the same small effect on the particle trajectories (Figure 4.17) as does the vertical wall for $\theta_e = 90°$.

To ascertain the cause of lower separation efficiency exhibited by the angled exit, we examined whether a small change in the corner geometry would have a similar impact as modifying the full length of the wall adjacent to the pinch exit. For Figure 4.17d, the 90° sharp corner was replaced with a 45° beveled edge having a length equal to $0.75a$ for a particle with η

= 0.6. The deviation of the particle trajectory from the fluid streamline is slightly less than that shown by the angled exit configuration, but much greater than that shown with the base case geometry. Lubrication effects are stronger between the particle and the beveled edge than between the particle and sharp corner, thereby causing the greater deviation of the particle trajectory from the fluid streamline. The simulation illustrates the pronounced effect that an irregularity at the pinch exit may have on the particle trajectory and device performance. As the length of the beveled edge is reduced, so are the particle-wall interactions, resulting in an increase in separation efficiency (not shown).

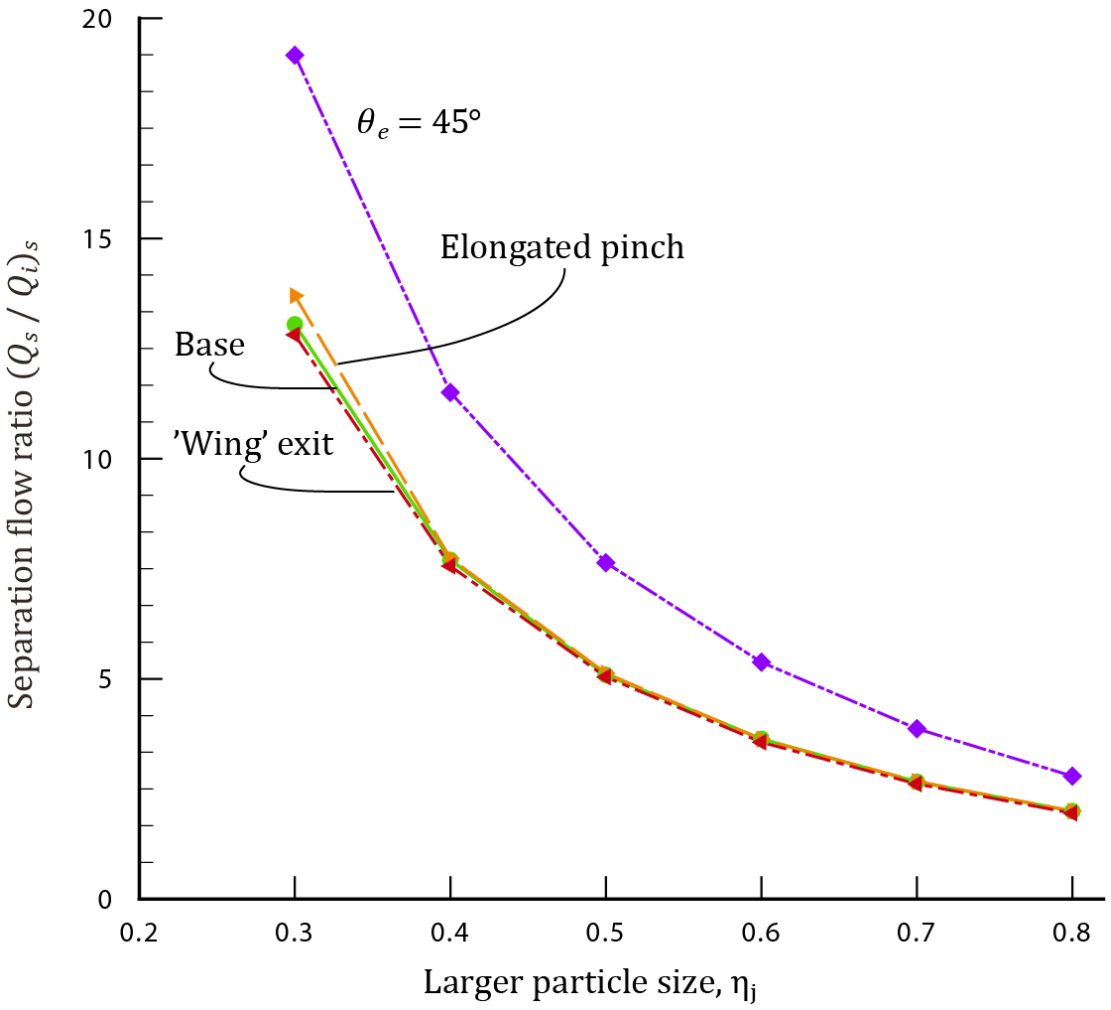

Figure 4.16 Separation flow ratio $(Q_s/Q_i)_s$ required to completely separate smaller particles (η_i = 0.2) from larger particles (η_j= varied) for four geometric configurations of the PFF. The base geometry is represented by (●) solid lines, angled exit by (♦) dash-dot-dot lines, elongated pinch by (►) long-dash lines, and wing geometry by (◄) short-dash lines.

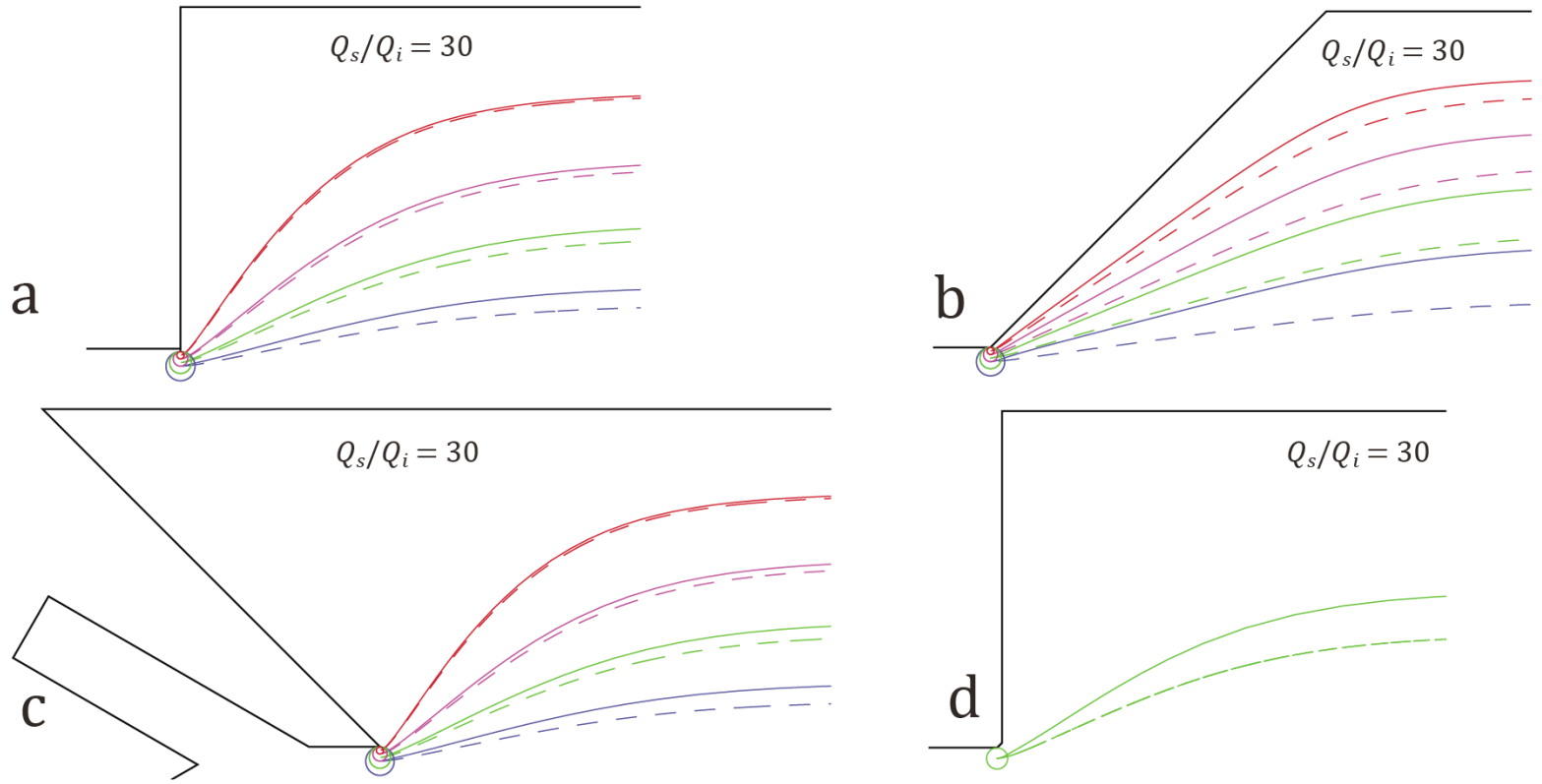

Figure 4.17 Comparison of particle trajectories (solid lines) to fluid-only streamlines (dashed curves) corresponding to starting positions of particle sizes η = 0.2, 0.4, 0.6, and 0.8 (top to bottom) with Q_s/Q_i = 30.0 for (a) base case, (b) angled exit, (c) winged exit and (d) beveled corner for η = 0.6. The fluid streamlines and particle trajectories originate at the exit of the pinch at a distance of 1.01a directly below the upper corner of the pinch exit.

4.4.7 Particle selectivity and recovery

For some applications, complete separation of particles by size is not necessary or may not be desired. A pre-determined ratio of small particles relative to larger particles may be achieved by varying the flow ratio. Moreover, the resulting mixture of particles exiting the PFF in a narrow trajectory band is more concentrated than the mixture entering the device. In this section, we show how the particle recovery and mix ratio may be determined when there is incomplete separation.

For simplicity, we consider two particle sizes and two product or exit streams, though the principles below may be easily extended to multiple particle sizes and/or product streams. Let y_e^* be the location of the 'splitter' in the exit area that separates the top and bottom product streams. To calculate the recovery of the particles of a given size in each product stream, we need to find the entry position (designated as y_i^*) that corresponds to a lateral exit position of y_e^*, as illustrated in Figure 4.18. This determination may be found by backwards integration of the particle trajectory from the exit to the inlet.

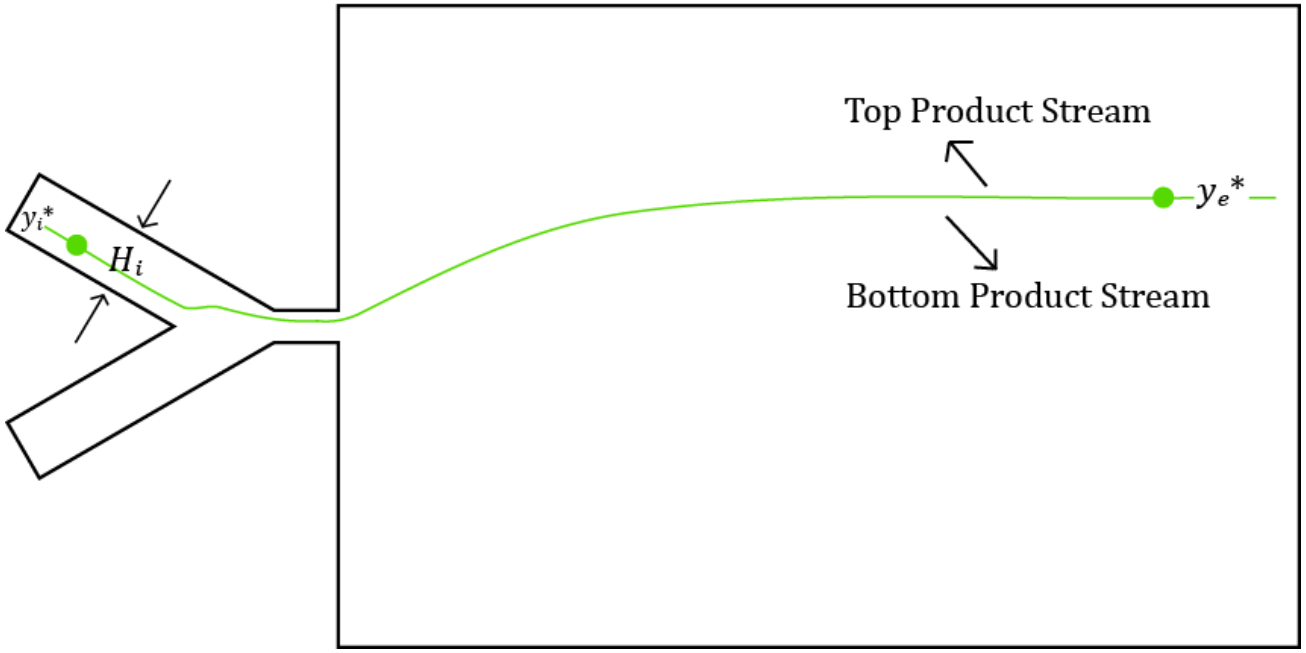

Figure 4.18 Separation trajectory of a particle entering the inlet at position y_i^* and proceeding to the exit at position y_e^*, which separates the top and bottom product streams.

The recovery of particles of the given size i in the top product stream is then simply the fraction of particles of size i that enter the inlet channel at locations above y_i^*:

$$R_i^{Top} = \frac{\int_{y_i^*}^{H_i - a_i} C_i(y_i) V_i(y_i) dy_i}{\int_{a_i}^{H_i - a_i} C_i(y_i) V_i(y_i) dy_i} , \tag{13}$$

where H_i is the inlet height, y_i is the distance from the lower wall of the inlet to the center of a particle of radius a_i, with C_i and V_i are the being the concentration and longitudinal velocity, respectively, of particles of radius a_i in the inlet. If we further assume that the entry flux is uniform so that the product $C_i(y_i)Vi(y_i)$ is constant for $a_i < y_i < (H_i - a_i)$, then equation (4.13) reduces to

$$R_i^{Top} = (H_i - a_i - y_i)/(H_i - 2a_i) . \tag{4.14}$$

Of course, the recovery of particles of size i in the bottom product stream is simply

$$R_i^{Bot} = 1 - R_i^{Top} . \tag{4.15}$$

Then, the fraction of particles of size i in the bottom product stream, by either number or mass, is

$$F_i^{Bot} = F_i^{Feed} R_i^{Bot} / R_j^{Bot} , \tag{4.16}$$

where F_i^{Feed} is the fraction of particles of size i (by number or mass) in the inlet feed stream, and R_j^{Bot} is the recovery of particles of size j in the bottom product stream.

Figure 4.19 shows numerical results for the recovery of the smaller particles in the top product stream as a function of the flow ratio of the sweep and inlet streams for several pairs of small and large particle sizes. Here, we consider the special case where the exit splitter location y_e* is placed just at the top of the band of the larger particles, so that all of the large particles are recovered in the bottom stream (R_j^{Bot} = 1, R_j^{Top} = 0). At low flow ratios, a relatively small fraction of the small particles is recovered in the top product stream, and so the bottom stream contains a mix of small and large particles given by equations (4.15) and (4.16). However, the separation efficiency increases with increasing flow rate, and complete separation (R_i^{Top} = 1, R_i^{Bot} = 0) is achieved when $Q_s/Q_i \geq (Q_s/Q_i)_s$.

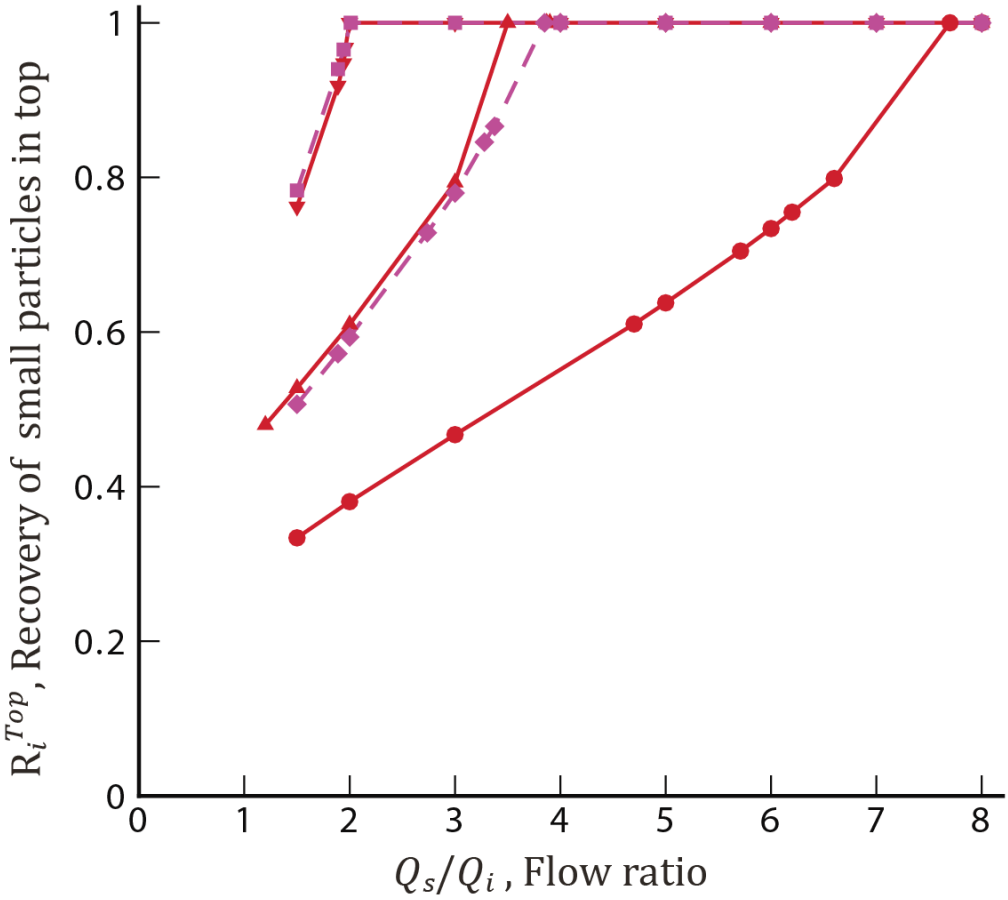

Figure 4.19 Recovery of smaller particles in the top outlet as a function of flow ratio, for several pairs of small and larger particles with η_i , η = 0.2, 0.4 (▼), 0.2, 0.6 (▲), 0.2, 0.8 (●), 0.4, 0.6 (■), and 0.4, 0.8 (♦).

4.5 Experimental Results

4.5.1 Pump calibration / measurement uncertainty

Accurate measurement of fluid volumetric flow ratio is critical for obtaining accurate and reproducible results. Pump selection for the experiment relied upon the delivery of constant flow rate. Settings for the pump flow rate are based on the syringe volume. The pumps were calibrated over 2, 10 and 20 minute intervals using settings of 10, 20 and 30 μL/min for five sets of experiments. Linear regression of the calibration data gives $Q_{meas} = (0.95 \pm 0.02)\ Q_{set}$ at the 95% confidence level, where Q_{set} is the manufacturer setting and Q_{meas} is the measured value of the flow rate.

4.5.2 Lateral exit positions of particles

Experiments using two sets of particle sizes (η = 0.25, 0.5) at sub-critical and super-critical flow ratios were conducted. Lateral exit positions of the particles were compared to BIM simulations. Critical flow ratios of $(Q_s/Q_i)_c$ = 32.5 and 7.73, respectively, are predicted for η = 0.25 and 0.5. Particles with η = 0.25 were tested at flow ratios of Q_s/Q_i = 2.0 (subcritical), 8.0 (subcritical), and 35 (supercritical). Particles with η = 0.5 were tested using flow ratios of Q_s/Q_i = 4.0 (subcritical), 9.0 (supercritical) and 35 (supercritical).

The lateral exit positions of the particles from the experiments and BIM simulations are compared in Table 4.3. Variations in particle radius are provided by the manufacturer as ≤ 0.1%, while variations in the channel height and particle location are ≤ 0.5% and attributed to pixel sizes of the mask and digital images.

This table shows that the exit position increases with inlet position for subcritical flow ratios but reaches a plateau for inlet positions above a critical value where the particles reach the upper wall of the pinch. It also shows that the exit position increases with flow ratio until the critical

flow ratio is reached. Most important, both theory and experiment show that the smaller particles exit on higher trajectories, so that separation is feasible. The exit locations from theory and experiment are within a few percent of each other, which may be somewhat fortuitous, as described below.

η	Q_s/Q_i	P	$2(y_e/H_e)_{sim}$	$2(y_e/H_e)_{exp}$
0.25	2	0.1	0.27	0.26
0.25	2	0.5	0.45	0.44
0.25	2	0.9	0.68	0.71
0.25	8	0.5	0.61	0.59
0.25	35	0.1	0.76	0.74
0.25	35	0.5	0.76	0.74
0.5	4	0.1	0.41	0.44
0.5	4	0.5	0.49	0.50
0.5	4	0.9	0.49	0.50
0.5	9	0.5	0.49	0.50
0.5	35	0.1	0.49	0.50
0.5	35	0.5	0.49	0.50

Table 4.3 Table showing comparisons of experimental results to BIM simulations of particle lateral exit positions at varying lateral entry positions and flow ratios. Here, y_e is measured from the channel midplane, and so $2y_e/H_e = 1.0$ is at the top wall of the exit. The longitudinal position at which the comparison is made is $x_e/L_e = 0.98$. The volumetric flow rate in the sweep stream was $Q_s = 5$ ml/min for all experiments in this table.

Although experimental results for lateral exit positions closely agree with the BIM simulations as shown in Table 4.3, the simulated and experimental particle trajectories differ. As shown in figure 4.20, the smaller particles exit the device closer to the top of the exit area, while the larger particles exit further away from the top of the device, as expected. However, the simulated particle trajectories (see figure 4.17a) have a more pronounced arch upon exiting the pinch, while the experimental trajectories are shallower. The experimentally-observed lateral positions of the particles continue to rise as the particles traverse the exit, and ultimately reach or even cross the simulated trajectories. We believe that the differences between the simulated and experimental trajectory are due to inertial effects and the low aspect ratio of the device exit area. For the experiments in figure 4.20, the Reynolds number in the pinch is Re = 5.3, where Re = $\rho U H_p/\mu$ and $U = (Q_s + Q_i)/(WH_p)$ is the average velocity. The inertia in the experiments causes fluid and particles to exit the pinch with flatter paths than predicted by the simulations, which assume Re << 1. For the moving-frame simulations, we also assumed a high ratio of width (in the direction normal to the paper) to height. For the experiments, this aspect ratio is 2.0 in the inlet, and 4.0 in the pinch, but only 0.2 in the exit area. Thus, the assumption of high aspect ratio is not met in the exit region, and the flow profiles (and, hence, particle trajectories) are different from the simulations. After the flow becomes fully developed in the exit, it is nearly a plug flow instead of parabolic flow in the *x*-*y* plane of the paper, with nearly parabolic flow instead in the *x*-*z* plane normal to the paper. As a result, the fluid streamlines became more evenly spaced in the exit far from the pinch, causing the particle exit positions to become closer to the upper wall.

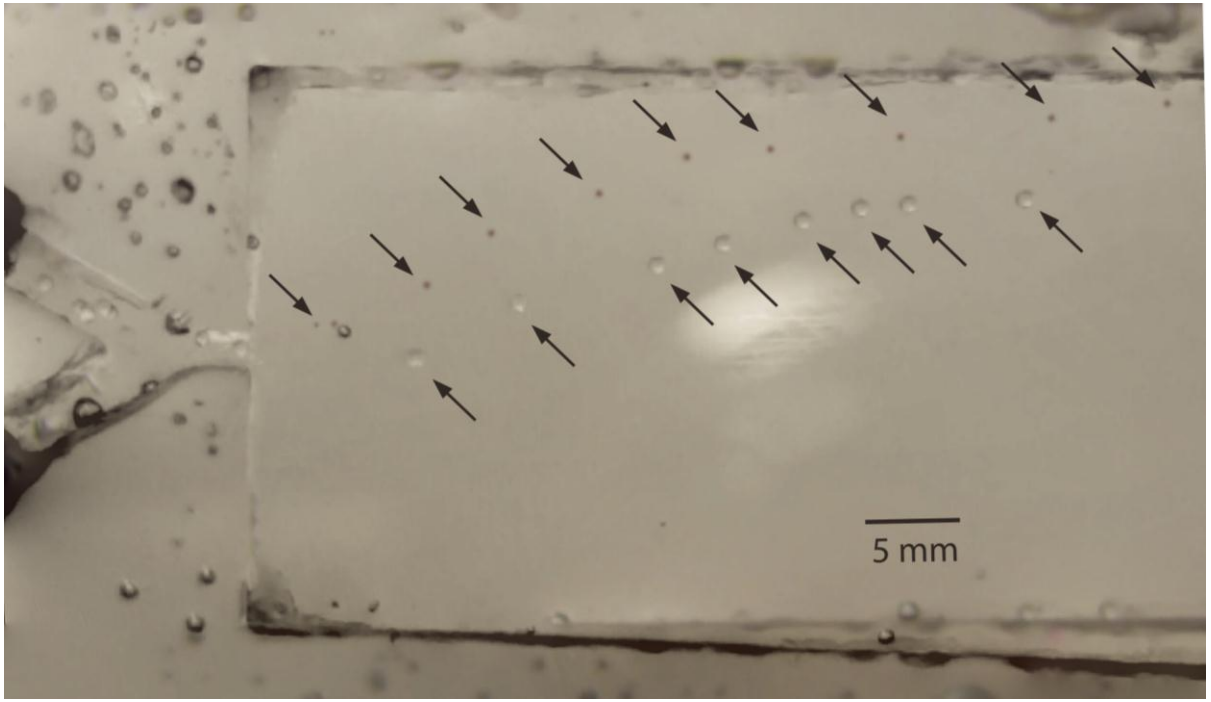

Figure 4.20 Time-lapse photographs of experiments (particle positions shown by arrows) for a supercritical flow ratio of $Q_s/Q_i = 35.0$, with Q_i, $Q_s = 0.14$, 5 ml/min (respectively). The two particle sizes shown are: $\eta = 0.25$ (downward-facing arrows) and $\eta = 0.5$ (upward-facing arrows).

4.6 Concluding remarks

This work provides theoretical and experimental studies of particle transport in a microfluidic device at low Reynolds numbers. The effects of systematically changing channel geometry and flow ratios on the trajectories are investigated for particles of different sizes being transported through a pinched-flow fractionation device. The ability to predict particle trajectories through complex channel geometries such as a PFF device, and how these trajectories deviate from fluid streamlines, aids in the design of devices with higher particle separation efficiency.

A method for handling particles that approach or even touch the channel walls and corners was implemented, resulting in the reduction of computational resources. A critical flow ratio $(Q_s/Q_i)_c$, where all particles (for a given particle size) reach the upper wall of the pinch and depart on the same downstream trajectory, was determined. A minimum separation flow ratio $(Q_s/Q_i)_s$, where complete separation of two particle sizes occur, was also determined. The values of $(Q_s/Q_i)_c$ and $(Q_s/Q_i)_s$ were found to decrease with an increase in the size of the larger particle. The ability to predict the separation flow ratios provides a means to quantify separation efficiency, and was used to design a PFF device having greater particle separation efficiency.

A channel geometry that delivers the greatest particle separation based on the lowest overall flow ratio can be predicted based on our MFBIM simulations. Variations to the inlet, pinch and outlet areas of the PFF geometry were examined to determine the effects of channel geometry on particle trajectories and separation efficiency. Of the geometries simulated using MFBIM, the base case configuration with a square exit provides the maximum particle separation with the lowest flow ratio of the sweep and inlet channels. An angled exit from the pinch region has reduced separation efficiency, due to particle-wall interactions, as does a beveled exit. Changing

the inlet geometry or pinch length had essentially no effect, since the flow is fully developed before reaching the pinch exit.

Experiments were conducted to test and validate our model using a PFF device. The device was fabricated using the channel geometry with greatest separation efficiency predicted by MFBIM simulations. Lateral exit positions and trajectories were obtained experimentally using small and large (η = 0.25, 0.5) polystyrene particles. The particles were tracked using subcritical and supercritical flow ratios obtained from simulations. Variation in lateral exit positions at subcritical flow ratios were greater, as expected, than those from supercritical flow ratios, due to the fact that subcritical flow ratios give rise to 'banding' effects. At supercritical flow ratios, a single trajectory was observed, with minimal variation in lateral exit position for both particle sizes. To experimentally examine the effect of lateral particle entry position on lateral exit position, particles were tracked at subcritical flow ratios.

Comparisons of values obtained from simulation and experimentation show qualitative agreement for predicted lateral exit positions, with the smaller particles exiting on higher trajectories, as expected. However, differences are observed in the particle trajectories predicted by the MFBIM and those obtained experimentally. We believe that the discrepancy between theory and experiment is due to inertial effects and the small aspect ratio of the exit area. Unfortunately, it was not feasible to operate the device with such low flow rates that Re << 1 was achieved, because the long transit times then allowed the particles to approach the horizontal walls due to imperfect density match of the particles and fluid.

Future experimental work should include smaller devices with high aspect ratios in the exit as well as entrance regions, while future simulations should include fully 3D geometries not restricted to high aspect ratios. Particle tracking and data acquisition can be improved with

particle image velocimetry (PIV). Parallel processing and GPU-based computing may be used to reduce the time required for computer-based simulations, resulting in cost savings.

4.7 Acknowledgements.

The authors thank the Ashley/McCormick Research Institute (06204591) for funding.

4.8 References

[1] S. Khan, A. Gunther, M. Schmidt, K. Jensen, Microfluidic synthesis of colloidal silica, *Langmuir* **20**, 8604-8611 (2004).

[2] T. Nisisako, T. Torii, T. Higuchi, Novel microreactors for functional polymer beads, *Chem. Eng. J.* **101**, 23-29 (2004).

[3] S. Sugiura, M. Nakajima, H. Ito, M. Seki, Synthesis of polymeric microspheres with narrow size distributions employing microchannel emulsification, *Macromol. Rapid Commun* **22**, 773-777 (2001).

[4] V. Larsen, L. Poulsen, H. Birgens, M. Dufva, A. Kristensen, Pinched flow fractionation devices for detection of single nucleotide polymorphisms *Lab Chip* **8**, 818-821 (2008).

[5] H. Maenaka, M. Yamada, M. Yasuda, M. Seki, Continuous and size-dependent sorting of emulsion droplets using microfluidic hydrodynamics in pinched microchannels, *Langmuir* **24**, 4405-4410 (2008).

[6] D. Inglis, J. Davis, T. Zieziulewicz, D. Lawrence, R. Austin, J. Sturm, Determining blood cell size using microfluidic hydrodynamics *J. of Immunological Methods* **329**, 151-156 (2008).

[7] M. Matsuda, M. Yamada, M. Seki, Blood cell classification utilizing hydrodynamic filtration, , *Electron. Commun. Jpn.* **94**, 1-6 (2011).

[8] S. Gawad, L. Schild, P. Renaud, Micromachined impedance spectroscopy flow cytometer for cell analysis and particle sizing, *Lab Chip* **1**, 76-92 (2001).

[9] H. Li, R. Bashir, Dielectrophoretic separation and manipulation of live and heat-treated cells of *Listeria* on microfabricated devices with interdigitated electrodes, *Sens. Actuators, B* **86**, 215-221 (2002),.

[10] H. Tsutsui, C. Ho, Cell separation by non-inertial force fields in microfluidic systems, *Mechanics Research Communications* **36**, 92-103 (2009).

[11] M. Kersaudy-Kerhoas, R. Dhariwal, M. Desmulliez, Recent advances in microparticle continuous separation, *IET Nanobiology* **2**, 1-13 (2008).

[12] M. Blom, E. Chmela, J. Gardeniers, R. Tijssen, M. Elwenspoek, A. Van den Berg, Design and fabrication of a hydrodynamic chromatography chip, A. *Sens. Actuators, B* **82**, 6761-6768 (2002).

[13] E. Chmela, R. Tijssen, M. Blom, J. Gardeniers, A. Van den Berg, A chip system for size separation of macromolecules and particles by hydrodynamic chromatography, *Anal. Chem* **74**, 3470-3475 (2002).

[14] T. Edwards, B. Gale, A. Frazier, A Microfabricated thermal field-flow fractionation system, *Anal. Chem*. **74**,1211-1216 (2002).

[15] J. Janca, J. Berneron, R. Boutin, Micro-thermal field-flow fractionation: new high-performance method for particle size distribution analysis, *J. Colloid Interface Sci.* **260**, 317-323 (2003).

[16] A. Nilsson, F. Petersson, H. Jonsson, T. Laurell, Acoustic control of suspended particles in micro fluidic chips, *Lab Chip* **4**, 131-135 (2004).

[17] M. Yamada, V. Kasim, M. Nakashima, J. Edahiro, M. Seki, Continuous cell partitioning using an aqueous two-phase flow system in microfluidic devices, *Biotechnol. Bioeng.* **88**, 484-489 (2004).

[18] J. Giddings, A system based on split-flow lateral-transport thin (SPLITT) separation cells for rapid and continuous particle fractionation, *Sep. Sci. Technol* **20**, 749-768 (1985).

[19] Y. Jiang, A. Kummerow, M. Hansen, Preparative particle separation by continuous SPLITT fractionation, *Microcolumn* **9**, 261-273 (1997).

[20] C. Fuh, Peer reviewed: Split-flow thin fractionation, *Anal. Chem.* **72**, 266A-271A (2000).

[21] M. Nakashima, Pinched-flow fractionation (PFF) for continuous particle separation in microfluidic device, *17th IEEE International Conference on Micro Electro Mechanical Systems* 33-36 (2004).

[22] M. Yamada, M. Nakashima, M. Seki, Pinched flow fractionation: Continuous size separation of particles utilizing a laminar flow profile in a pinched microchannel, *Anal. Chem*. **76**, 5465-5471 (2004).

[23] W. Kim, Y. Park, J. Shin, D. Lee, Size determination of diesel soot particles using flow and sedimentation field-flow fractionation, *Anal. Chem.* **71**, 3265-3272 (1999**)**.

[24] M. Moon, H. Kim, S. Kwon, S. Lee, Y. Chang, H. Lim, Pinched inlet split flow thin fractionation for continuous particle fractionation: Application to marine sediments for size-dependent analysis of PCDD/Fs and Metals, *Anal. Chem.* **76**, 3236-3243 (2004).

[25] J. Takagi, M. Yamada, M. Yasuda, M. Seki, Continuous particle separation in a microchannel having asymmetrically arranged multiple branches, *Lab Chip* **5**, 778-784 (2005).

[26] K. Andersen, S. Levinsen, W. Svendsen, F. Okkels, A generalized theoretical model for "Continuous particle separation in a microchannel having asymmetrically arranged multiple branches', *Lab Chip* **9**, 1638-1639 (2009).

[27] H. Bruus, *Theoretical Microfluidics*, Oxford University Press, 1st edn., 48-51 (2007).

[28] A. Zinchenko, J. Ashley, R. Davis, A moving-frame boundary-integral method for particle transport in microchannels of complex shape, *Phys. Fluids* **24**, 043302 (2012).

[29] C. Pozrikidis, *Boundary-Integral and Singularity Methods for Linearized Viscous Flow*, Cambridge University Press, Cambridge, UK 1992.

[30] O. Ladyzhenskaya, *The Mathematical Theory of Viscous Imcompressible Flow*, Revised Second Edition, Gordon and Breach Science Publishers, NY, NY, 1969.

[31] S. Kim, S. Karilla, *Microhydrodynamics – Principles and Selected Applications*, Dover, Mineola, NY 2005.

[32] K. Haraldsson, J. Hutchison, K. Anseth, C. Bowman, 3D polymeric microfluidic device fabrication via contact liquid photolithographic polymerization (CLiPP), *Sens. Actuators B, Chemical* **113**, 454-460 (2006).

[33] J. Hutchison, K. Haraldsson, B. Good, R. Sebra, L. Luo, K. Anseth, C. Bowman, Robust polymer microfluidic device fabrication via contact liquid photolithographic polymerization (CLiPP), *Lab Chip* **4**, 658-662 (2004).

[34] J. Ashley, N. Cramer, R. Davis, C. Bowman, Soft-lithograpy fabrication of microfluidic features using thiol-ene formulations, *Lab Chip* **11**, 2772-2778 (2011).

Chapter 5

Concluding remarks and recommendations

5.1 Concluding remarks

5.1.1 Device materials formulation

Microfluidic devices, such as pinched-flow-fractionation (PFF) devices, require high quality and fidelity and high-aspect-ratio features, which creates unique design and fabrication challenges. This work developed techniques for constructing microfluidic devices with high-aspect-ratio features with high quality and fidelity. In Chapter 2, a modified, confocal-microscopy technique was developed to quantatively determine feature quality quantitatively. Microfluidic devices and independent, photolithographically-defined features were constructed using thiol-ene resins via contact liquid photolithographic polymerization (CLiPP).[1] Resin cure times and initiator-to-inhibitor ratio were found to have a strong impact on feature quality. Both resin cure time and the initiator-to-inhibitor ratio were systematically varied to optimize feature quality to produce a variety of feature shapes and depths commonly found in microfluidic devices. The highest feature quality was found for initiator-to-inhibitor ratios that ranged from 1:1 to 1:1.5 and for cure times that were just sufficient to achieve gelation in the desired volumes. A correlation between aspect ratio and feature thickness for thiol-enes was established, as well. Unlike features fabricated using acrylate resins, the quality of features produced from the thiol-ene resins did not diminish with an increase in aspect ratio. Combining the optimization technique with thiol-ene materials lead to a photopolymerizable resin that was capable of fabricating high quality, high-aspect-ratio microfluidic channels that were used to fabricate a PFF device.

5.1.2 Moving-Frame Boundary-Integral Method

A Moving-Frame Boundary-Integral Method (MFBIM) was developed in Chapter 3 and used in this work to accurately predict the movement of a spherical particle in microfluidic channels having complex geometries. Validation of the model was proceeded by systematically simulating fluid-only transport in a 2D environment having straight channels[2,3,4,5] and sharp corners.[6,7] Following validation of the 2D model, the more complex 3D model was compared to existing numerical solutions for transport of 3D particles in a straight channel with a high degree of accuracy.[8,9] Complex channel configurations, including a 'T' bifurcation and pinched-flow-fractionation' geometry, were simulated using the MFBIM algorithm. Simulation results for the 'T' configuration compare favorably to data provided by Audit and Olbricht[10] though few accurate simulation models exist for the pinched-flow-fractionation geometry.[11,12] Our algorithm was applied to the PFF geometry and compared to existing experimental data, showing good qualitative agreement between the two.[13]

5.1.3 Simulations and experimental procedure

The final goal of this dissertation was to utilize MFBIM to assist in the design of a microfluidic device with enhanced separation efficiency. Previous studies of PFF devices have shown that channel geometry, flow rate and particle size all affect particle trajectories, and hence, separation efficiency. To study the effects of channel geometry, particle size, and fluid flow on the PFF device's separation performance, a microfluidic channel using the PFF geometry was fabricated. In Chapter 4, simulations were conducted to predict the effects of channel geometry, flow rates, and particle sizes on separation efficiency. For a given PFF geometry, Q_s / Q_i represents the flow ratio of the sweep and inlet streams, respectively. Two categories of flow ratios were found useful in determining the optimal separation efficiency. The

critical flow ratio $(Q_s/Q_i)_c$, is where all particles (of a given particle size) are predicted to reach the upper wall of the pinch and depart on the same trajectory, independent of initial particle location in the inlet. A minimum separation flow ratio $(Q_s/Q_i)_s$, where complete separation of two particle sizes is predicted to occur, was also explored. The value of $(Q_s/Q_i)_s$ was found to decrease with an increase (in size) of the larger-sized particle, thus allowing for lower dilution by the sweep stream as the ratio of particle size and pinch brought increases. The ability to predict the separation flow ratios provides a method to quantify separation efficiency and was used to design a PFF device having greater particle separation efficiency.

In Chapter 4, to examine the effects of channel geometry on particle trajectories and separation; adjustments were made to the inlet, pinch and outlet areas of the PFF geometry. Lengthening the pinch region or making the inlet channels more narrow (not shown), where the flow ratio is supercritical, has only a small effect on particle trajectory after exiting the pinch. The minimized effect of modifications to the inlet areas and lengthening of the pinch is not unexpected, as the fluid streamlines and particle trajectories become parallel to the channel walls almost immediately upon entering the pinch, resulting in fluid-flow flow that is fully developed at the pinch exit and independent of initial conditions. In contrast, the angled exit case gives poorer separation than does the base case, requiring larger flow ratios to achieve complete separation. The reduced performance is because the angled exit does not provide as much separation of the trajectories of particles of different sizes as they pivot around the corner (vertex 12) and leave the pinch region for the exit region. In particular, the angled wall is closer to the particles and causes resistance as they pull away from the corner, so that the particle trajectories are higher than the streamlines. This effect is greatest for the larger particles, reducing their separation from the smaller particles. Finally, the wing exit case has almost the same separation

as the base case, because the angled wall in this case has almost the same small effect on the particle trajectories as does the vertical wall.

To determine the cause of lower separation efficiency exhibited by the angled exit, we examined whether a small change in the corner geometry would have a similar impact as modifying the full length of the wall adjacent to the pinch exit. Simulation results predict that the deviation of the particle trajectory from the fluid streamline is slightly less than that shown by the angled exit configuration, but much greater than that shown with the base case geometry. Lubrication effects are stronger between the particle and the beveled edge than between the particle and sharp corner, as the particle is closer to the wall immediately after exiting the pinch, thereby causing the greater deviation of the particle trajectory from the fluid streamline. The simulation illustrates the pronounced effect that an irregularity at the pinch exit may have on the particle trajectory and device performance.

Experiments were conducted using a PFF device that was fabricated with the optimized, thiol-ene-based photopolymerizable resin from Chapter 2 using the CLiPP process. The PFF device exhibited many desirable characteristics such as short cure time without significant oxygen inhibition, high feature fidelity and quality, and the formation of high-aspect-ratio channels. To alleviate some of the issues associated with traditional micro-scale microfluidic devices, such as pump control at small volumetric flow rates and ease of particle tracking, a larger-scale device was used. To test the operation of the device, polystyrene particles in the range of 200 - 500 μm (diameter) were injected and separated in the PFF device. Lateral exit positions of the particles were compared to the MFBIM simulations. Comparisons show that lateral exit position increase proportionally with inlet position for subcritical flow ratios. The lateral exit position reaches a plateau for inlet positions above the critical position where the particles reach the upper wall of

the pinch. Both theory and experiment indicate that the smaller particles exit on higher trajectories, making separation possible.

Although experimental results for lateral exit positions agree qualitatively with the MFBIM simulations, the simulated and experimental particle trajectories differ in some aspects. The simulated particle trajectories have a more pronounced arch upon exiting the pinch, while the experimental trajectories are shallower. The experimentally-observed lateral exit positions of the particles continue to rise as the particles traverse the exit, and ultimately reach or even cross the simulated trajectories. The discrepancy between MFBIM simulations and experimental results is likely due to differences in the simulated and experimental geometries of the exit region. Additionally, a greater total volumetric flow rate was required to move the particles through the device, resulting in higher than expected Reynolds numbers. Higher Reynolds numbers in the exit area of the device resulted in inertial effects, impacting the particle trajectories. For the MFBIM simulations, the assumption that the exit-area aspect ratio is large, so that the top and bottom walls had minimal effect on the particle trajectory, is not met. For the PFF used in the experiments, the aspect ratio is 2.0 for the inlet region, and 4.0 in the pinch, but only 0.2 in the exit area. The low aspect ratio in the exit region does appear to affect particle trajectories, resulting in particle trajectories that differ from those provided by the MFBIM simulations using a 2D fluid flow model that assumes the top and bottom walls are an infinite distance apart. In particular, there is more resistance to flow toward the corner regions just above and below the pinch exit, causing shallower exit streamlines and trajectories. After the flow becomes fully developed in the exit, it is nearly a plug flow instead of parabolic flow in the *x*-*y* plane of the device, with nearly parabolic flow instead in the *x*-*z* normal plane of the device, as shown in Figure 5.1. As a result, the fluid streamlines became more evenly spaced in the exit far from the

pinch, causing the particle exit positions to be closer to the upper wall than predicted by simulation.

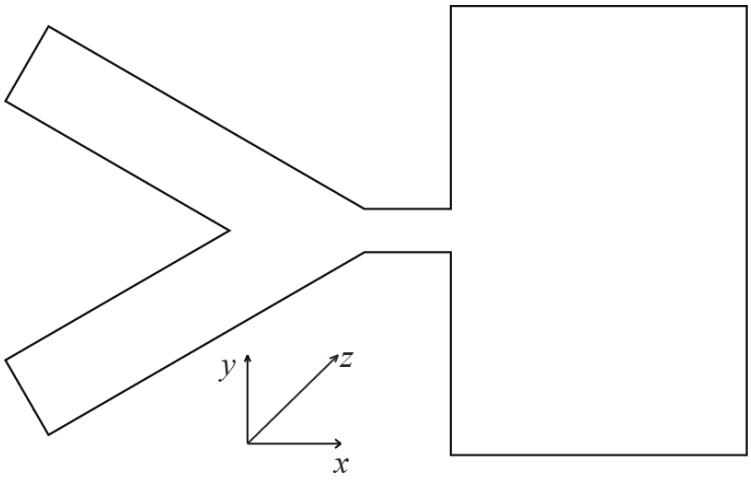

Figure 5.1 Idealized view (not to scale) of PFF device along *x*-*y* plane. The *z*-plane is normal to the plane of the paper.

5.2 Recommendations for future work

5.2.1 Device materials formulation

The use of photopolymerizable thiol-ene resins in the construction of microfluidic devices presents a significant opportunity for creating a wide range of application-specific formulations.[14] Combination of thiol-enes with (meth)acrylates presents an even greater array of achievable physical and chemical characteristics that can be customized to fit application-specific requirements. Additional work related to formulation development for thiol-ene-(meth)acrylate resins should present novel and innovative solutions in fabricating microfluidic devices. In particular, application-specific physical and chemical attributes can be achieved by tuning the resin formulation and cure characteristics.

In response to the need to quantify feature quality, an optical technique using confocal microscopy was investigated. The optical technique developed during the course of this work provides a tool that can be used to enhance or optimize a wide range of photopolymerizable resins. For this work, feature fidelity, as well as various aspects of feature and quality, were assessed as functions of various attributes. The use of statistical design in selection and formulation of resin attributes that have an effect on feature fidelity will lead to additional refinement of the materials and formulations used to fabricate microfluidic devices.

Measurement techniques used in the determination of feature quality can also be improved. Several software packages are now available for use in conjunction with confocal microscopy to provide quantitative measurement of features.[15,16,17] Feature topology can be measured with a high degree of accuracy, providing information about feature curvature, roughness, and surface irregularities that affect the microfluidic device performance.

5.2.2 Moving-Frame Boundary-Integral Method

For this work, the surface of the particle, assumed to be a sphere, was discretized into triangular elements to form an unstructured mesh. When the particle comes in near-contact with the channel wall, lubrication effects play a role in particle transport behavior; computational resolution at the channel wall is increased by redistribution of mesh nodes on the particle surface. The gap-adaptive algorithm provides flexibility for discretization of the particle surface and the panels of the computational cell. Improvements in numerical precision while decreasing computational requirements were achieved with the implementation of an adaptive mesh over the particle surface, where the number of elements is modified based on proximity to the channel wall.

The MFBIM algorithm could be modified to include transport of a 3D particle in a fully-rendered 3D device. Further enhancement of the code would include a generalized model of MFBIM to simulate transport of deformable drops and particles through complex microchannels.

5.2.3 Simulations and experimental procedure

Extending the computer code to include a 3D fluid-only domain provides a method for predicting particle transport at low Reynolds number in channels with multiple wall effects. Predicting the transport attributes of 3D particles with different shapes and contours (such as oblate or prolate spheroids) in a complex microchannel would also provide insight into the behavior of whole-blood transport through capillaries.

To mitigate some of the operational and particle tracking issues associated with micro-scale features, the overall scale of our PFF device was enlarged. A micro-scale device with channel sizes of ~ 30 μm and similarly scaled particle diameters should be constructed and tested with appropriate exit geometry. The aspect ratio should be increased for all channels, and in

particular, we theorize that the low aspect ratio of the exit area of the PFF device influenced the trajectory path. Increasing the aspect ratio of the device exit area would mitigate some of the experimental issues requiring a higher volumetric flow rate in the device resulting in inertial effects and deviation from simulations. Aspect ratios of at least 4 should be used in the design of all interior channel components of the PFF.

Particle image tracking, data acquisition and information related to particle velocity can be improved through the use of particle image velocimetry (PIV).[18] The enhanced capability of the technique provides high-resolution particle-image fields, vector field information, and flow field images useful in studying particle movement in low Reynolds number flows.

As the complexity of channel configurations that can be modeled increases, so do the necessary computational resources. Incremental increases in the dimensionality of a model result in exponentially higher demands on processing time. Recent advances in computer architecture and the use of general processing unit (GPU) computing provides relief for computationally-intensive applications. All computer-based code for this work is FORTRAN based whereas compute unified device architecture (CUDA)[19,20,21] is a parallel computing architecture based code that is compatible with traditional FORTRAN code. The availability of high-performance computing resources relieves some of the constraints brought about with modeling of complex systems and would be ideal for implementations that would be used here.[22]

5.3 References

[1] J. Hutchison, K. Haraldsson, B. Good, R. Sebra, N. Luo, K. Anseth, and C. Bowman, Robust polymer microfluidic device fabrication via contact liquid photolithographic polymerization (CLiPP), *Lab Chip* **4**, 758-662 (2004).

[2] F. Pan and A. Acrivos, Steady flows in rectangular cavities, *J. Fluid Mech.* **28**, 643–655 (1967).

[3] O. Burggraf, Analytical and numerical studies on the structure of steady separated flows, *J. Fluid Mech.* **24**, 113–151 (1966).

[4] R. P. Gupta and M. M. Manohar, Boundary approximations and accuracy in viscous flow computations, *J. Comput. Phys.* **31**, 265–288 (1979).

[5] R. P. Gupta, M. M. Manohar, and B. Noble, Nature of viscous flows near sharp corners, *Comput. Fluids* **9**, 379–388 (1981).

[6] W. R. Dean and P. E. Montagnon, On the steady motion of viscous liquid in a corner, *Proc. Cambridge Philos. Soc.* **45**, 389–394 (1949).

[7] H. K. Moffatt, Viscous and resistive eddies near a sharp corner, *J. Fluid Mech.* **18**, 1–18 (1964).

[8] N. Liron and N. Mochon, Stokes flow for a Stokes-let between two parallel flat plates, *J. Eng. Math.* **10**, 287–303 (1976).

[9] M. Staben, A. Z. Zinchenko, and R. H. Davis, Erratum: Motion of a particle between two parallel plane walls in low-Reynolds-number Poiseuille flow, *Phys. Fluids* **16**, 4204–4206 (2004).

[10] D. M. Audet and W. L. Olbricht, The motion of model cells at capillary bifurcations, *Microvasc. Res.* **33**, 377–396 (1987).

[11] M. Nakashima, M. Yamada, and M. Seki, Pinched flow fractionation (PFF) for continuous particle separation in a microfluidic device, in *Proceedings of 17th IEEE International Conference on Micro Electro Mechanical Systems* 33–36 (IEEE, Piscataway, NJ, 2004).

[12] M. Yamada, M. Nakashima, and M. Seki, Pinched flow fractionation: Continuous size separation of particles utilizing a laminar flow profile in a pinched microchannel, *Anal. Chem.* **76**, 5465–5471 (2004).

[13] Y. Sai, M. Yamada, M. Yasuda, and M. Seki, Continuous separations of particles using a microfluidic device equipped with flow rate control valves, *J. Chromatogr. A* **1127**, 214–220 (2006).

[14] C. Hoyle, A. Lowe and C. Bowman, Thiol-ene click chemistry, *Angew. Chem., Int. Ed.* **49**, 1540-1572 (2010).

[15] S. Paddock, Principles and practices of laser scanning confocal microscopy, *Mol. Biotech.* **16(2)**, 215-225 (2000).

[16] S. Weidtkamp-Peters, K. Weisshart, L. Schmiedeberg, and P. Hemmerich, Fluorescence correlation spectroscopy to assess the mobility of nuclear proteins, *Meth. In Mol. Biology* **464**, 321-341 (2008).

[17] R. Rigler, *Biochem. and Biophys. Res. Com.* **396**, 170-175 (2010).

[18] J. Santiago, S. Werely, C.D. Meinhart, D. Beebe and R. Adrian, A particle image velocimetry system for microfluidics, *Exp. In Fluids* **25**, 316-319 (1998).

[19] J. Sanders, E. Kandrot, *CUDA by example: An introduction to general-purpose GPU programming*, Addison-Wesley Professional, 1st ed., 2010.

[20] S. Cook, *CUDA Programming: A developer's guide to Parallel computing with GPUs (Applications of GPU Computing series)*, Morgan Kaufmann, 1st ed., 2012.

[21] W. Hwu, *GPU computing gems emerald edition (Applications of GPU computing series)*, Morgan Kaufmann, 1st ed., 2011.

[22] D. Kirk, W. Hwu, *Programming massively parallel processors: A hands-on Approach (applications of GPU Computing series)*, Morgan Kaufmann, 1st ed., 2010.

Bibliography

Andersen, K., Levinsen, S., Svendsen,W. and Okkels, F., A generalized theoretical model for "Continuous particle separation in a microchannel having asymmetrically arranged multiple branches', *Lab Chip* **9**, 1638-1639 (2009).

Ashley, J. F., Bowman, C. N. and Davis, R. H., Hydrodynamic selection of particulate matter using pinched-flow fractionation, *Langmuir* (2012, submitted).

Ashley, J. F., Cramer, N. B., Davis, R. H. and Bowman, C. N., Soft-lithography fabrication of microfluidic features using thiol-ene formulations, *Lab Chip* **11**, 2772-2778 (2011).

Audet, D. M. and Olbricht, W. L., The motion of model cells at capillary bifurcations, *Microvasd. Res.* **33**, 377-396 (1987).

Li, H. and Bashir, R., Dielectrophoretic separation and manipulation of live and heat-treated cells of *Listeria* on microfabricated devices with interdigitated electrodes, *Sens. Actuators, B* **86**, 215-221 (2002),.

Bazhlekov, J. B., Anderson, P. D. and Heijer, H. E. H., Nonsingular boundary integral method for deformable drops in viscous flows *Phys. Fluids* **16**, 1064-1081 (2004).

Bhattacharya, S., Blawzdziewicz, J. and Wajnryb, E., Many-particle hydrodynamic interactions in parallel-wall geometry: Cartesian-representation method, *Physica A* **356**, 294-340 (2005a).

Bhattacharya, S., Blawzdziewicz, J. and Wajnryb, E., Hydrodynamic interactions of spherical particles in suspensions confined between two planar walls, *J. Fluid Mech.* **541**, 263-292 (2005b).

Bhattacharya, S., Blawzdziewicz, J. and Wajnryb, E., Far-field approximation for hydrodynamic interactions in parallel-wall geometry *J. Comp. Physics* **212**, 718-738 (2006a).

Bhattacharya, S., Blawzdziewicz, J. and Wajnryb, E., Hydrodynamic interactions of spherical particles in Poiseuille flow between two parallel walls *Phys. Fluids* **18**, 053301 (2006b).

Bland, M. H., and Peppas, N. A., Photopolymerized multifunctional (meth)acrylates as model polymers for dental applications, *Biomaterials* **17**, 1109-1114 (1996).

Blom, M., Chmela, E., Gardeniers, J., Tijssen, R., Elwenspoek, M., and Van den Berg, A., Design and fabrication of a hydrodynamic chromatography chip, A. *Sens. Actuators, B* **82**, 6761-6768 (2002).

Bowman, C. N., and Kloxin, C. J., Toward an enhanced understanding and implementation of photopolymerization reactions, *AlChE J.* **54** (2008) 2775-2795.
Bruus, H., *Theoretical Microfluidics*, Oxford University Press, 1st ed., (2007).

Burggraf, O., Analytical and numerical studies on the structure of steady separated flows, *J. Fluid Mech*. **24**, 113–151 (1966).

Chien, S., Tvetenstrand, C.D., Farrel Epstien, M. S. and Schmid-Schnbien, G. W., Model studies on distributions of blood cells at microvascular bifurcations *Amer. J. Physiol.* **248**, H568-H576 (1985).

Chmela, E., Tijssen, R., Blom, M., Gardeniers, J. and Van den Berg, A., A chip system for size separation of macromolecules and particles by hydrodynamic chromatography, *Anal. Chem* **74**, 3470-3475 (2002).

Chován T. and Guttman, A., Microfabricated devices in biotechnology and biochemical processing, *Trends in Biotechnology* **20**,116-122 (2002).

Cook, S., *CUDA Programming: A developer's guide to Parallel computing with GPUs (Applications of GPU Computing series)*, Morgan Kaufmann, 1st ed., 2012.

Couillette C. and Pozrikids, C., Flow due to a periodic array of point forces, and the motion of small particles within a cylindrical tube of arbitrary cross section *Phys. Fluids* **8**, 2019-2031 (1996).

Cramer, N. B., and Bowman, C. N., Kinetics of thiol-ene and thiol-acrylate photopolymerizations with real-time fourier transform infrared, *J. Polym. Sci., Part A: Polym. Chem*. **40**, 3311-3319 (2001).

Cristini, V., Blawzdziewicz, J. and Loewenberg, M., An adaptive mesh algorithm for evolving surfaces: simulations of drop breakup and coalescence *J. Comput. Phys.* **168**, 445-463 (2001).

Dean W. R. and Montagnon, P. E., On the steady motion of viscous liquid in a corner *Proc. Camb. Phil. Soc.* **45**, 389-394 (1949).

Dean W. R. and O'Neill, M., A slow motion of viscous liquid caused by the rotation of a solid sphere, *Mathematika* **10**, 13-24 (1963).

Ditchfield, R. and Olbricht, W., Effects of particle concentration on partitioning of suspensions at small divergent bifurcations, *J. Biomech. Eng.* **118**, 287-294 (1996).

Duffy, D., McDonald, J., Schueller, J. and Whitesides, G. R., Rapid prototyping of microfluidic systems in poly(dimethylsiloxane), *Anal. Chem.* **70,** 4974-4984 (1998).

Edwards, T., Gale, B. and Frazier, A., A Microfabricated thermal field-flow fractionation system, *Anal. Chem*. **74**,1211-1216 (2002).
Fadlun, E. A., Verzicco, R., Orlandi, P. and Mohd-Yusof, J., Combined immersed-boundary finite-difference methods for three-dimensional complex flow simulations *J. Comput. Physics* **161**, 35-60 (2000).

Fuh, C., Peer reviewed: Split-flow thin fractionation, *Anal. Chem.* **72**, 266A-271A (2000).

Fung, Y. C., Stochastic flow in capillary blood vessels *Microvas. Res.* **5**, 34-48 (1973).

Ganatos, P., Pfeffer, R. and Weinbaum, S., A strong interaction theory for the creeping motion of a sphere between plane parallel boundaries. 2. Parallel motion, *J. Fluid Mech.* **99**, 755-783 (1980).

Ganatos, P., Weinbaum. S. and Pfeffer, R., A strong interaction theory for the creeping motion of a sphere between plane parallel boundaries. 1. Perpendicular motion, *J. Fluid Mech.* **99**, 739-753 (1980).

Ganatos, P., Weinbaum, S. and Pfeffer, R., Gravitational and zero-drag motion of a sphere of arbitrary size in an inclined channel at low reynolds-number, *J. Fluid Mech.* **124**, 27-43 (1982).

Gawad, S., Schild, L. and Renaud, P., Micromachined impedance spectroscopy flow cytometer for cell analysis and particle sizing, *Lab Chip* **1**, 76-92 (2001).

Giddings, J., A system based on split-flow lateral-transport thin (SPLITT) separation cells for rapid and continuous particle fractionation, *Sep. Sci. Technol* **20**, 749-768 (1985).

Glaser, D. M., Stabilization of thiolene compositions, *European Patent EP19920300934* filed 02/04/1992 and published 04/26/1995.

Glowinski, R., Pan, T. W., Hesla, T. I. and Joseph, D. D., A distributed Lagrange multiplier/ fictitious domain method for particulate flows *Int. J. Multiphase Flow* **25**, 755-794 (1999).

Goldman, A. J., Cos, R. G. and Brenner, H., Slow viscous motion of a sphere parallel to a plane wall. I. Motion through a quiescent fluid *Chem. Eng. Sci.* **22**, 637-651 (1967). *ensch. Amsterdam* **5**, 168-175 (1896) [also in *Abhandlungenuber Theoretische Physik* (Leipzig, Berlin, 1907), **1**, 23-42; and Collected Papers (Martinus Nijhoff, The Hague, 1937) **4**, 7].

Guber, H., Heckele, M., Herrmann, D., Muslija, A., Saile, V., Eichhorn, L., Gietzelt, T., Hoffmann, W., Hauser, P., and Tanyanyiwa, J., Microfluidic lab-on-a-chip systems based on polymers—fabrication and application, *J. Chem. Eng*. **101**, 447-453 (2004).

Gupta R. P. and Manohar, M. M., Boundary approximations and accuracy in viscous flow computations *J. Comput. Phys.* **31**, 265-288 (1979).

Gupta, R. P., Manohar, M. M. and Noble, B., Nature of viscous flows near sharp corners *Computers and Fluids* **9**, 379-388 (1981).

Happel, J. and Brenner, H., *Low Reynolds Number Hydrodynamics*, 4th ed., Martinus Nijhoff, Dordecht (1986).

Haraldsson, K. T., Hutchison, J. B., Anseth, K. S. and Bowman, C. N., 3D polymeric microfluidic device fabrication via contact liquid photolithographic polymerization (CLiPP), *Sens. Actuators B, Chemical* **113**, 454-460 (2006).

Higdon, J. J. L., Stokes flow in arbitrary two-dimensional domains: Shear flow over ridges and cavities *J. Fluid Mech.* **159**, 195-226 (1985).

Ho, B. P. and Leal, L. G., Inertial migration of rigid spheres in 2-dimensional unidirectional flows *J. Fluid Mech.* **65**, 365-400 (1974).

Hopf, E., Ũber die Anfangswertaufgabe für die hydrodynamischen Grundgleichungen, *Mach. Nachrichten* **4**, 213-231 (1950-1951).

Hoyle, C. E., Lee, T. Y. and Roper, T., Thiol-Enes: Chemistry of the past with promise for the future, *Part A: Polym. Chem.* **42**, 5301-5338 (2004).

Hoyle, C. E., Lowe, A. B., and Bowman, C. N., Thiol-click chemistry: a multifaceted toolbox for small molecule and polymer synthesis, *Chem. Soc. Rev.* **39**, 1355-1387 (2010).

Hoyle, C. E., Lowe, A. B. and Bowman, C. N., Thiol-Ene click chemistry, *Angewandte Chemie* **49** , 1540-1573 (2010).

Hutchison, J. B., Haraldsson, K. T., Good, B., Sebra, R., Luo, N., Anseth, K. S., and Bowman, C. N., Robust polymer microfluidic device fabrication via contact liquid photolithographic polymerization (CLIPP), *Lab Chip* **4**, 658-662 (2004).

Hwu, W., *GPU computing gems emerald edition (Applications of GPU computing series)*, Morgan Kaufmann, 1st ed., 2011.

Inglis, D., Davis, J., Zieziulewicz, T., Lawrence, D., Austin and R., Sturm, J., Determining blood cell size using microfluidic hydrodynamics *J. of Immunological Methods* **329**, 151-156 (2008).

Jain, A. and Posner, J. D., Particle dispersion and separation resolution of pinched flow fractionation *Anal. Chem.* **80**, 1641-1648 (2008).

Janca, J., Berneron, J. and Boutin, R., Micro-thermal field-flow fractionation: new high-performance method for particle size distribution analysis, *J. Colloid Interface Sci.* **260**, 317-323 (2003).

Jiang, Y., Kummerow, A., and Hansen, M., Preparative particle separation by continuous SPLITT fractionation, *Microcolumn* **9**, 261-273 (1997).

Kelmanson, M. A., Modified integral equation solution of viscous flows near sharp corners *Computers & Fluids* **11**, 307-324 (1983).

Kelmanson, M. A., An integral equation method for the solution of singular slow flow problems *J. Comp. Phys.* **51**, 139-158 (1983).

Kersaudy-Kerhoas, M., Dhariwal, R., and Desmulliez, M., Recent advances in microparticle continuous separation, *IET Nanobiology* **2**, 1-13 (2008).

Khan, S., Gunther, A., Schmidt, M., and Jensen, K., Microfluidic synthesis of colloidal silica, *Langmuir* **20**, 8604-8611 (2004).

Kim, S. and Karilla, S., *Microhydrodynamics – Principles and Selected Applications*, Dover, Mineola, NY 2005.

Kim, W., Park, Y., Shin, J., and Lee, D., Size determination of diesel soot particles using flow and sedimentation field-flow fractionation, *Anal. Chem.* **71**, 3265-3272 (**1999)**.

Kirk, D. , and Hwu, W. *Programming massively parallel processors: A hands-on Approach (applications of GPU Computing series)*, Morgan Kaufmann, 1st ed., 2010.

Kloosterboer, J. G., Network formation by chain crosslinking photopolymerization and its applications in electronics, *Adv. Polym. Sci.* **84**. 1-61 (2001).

Ladyzhenskaya, O. A., *The Mathematical Theory of Viscous Incompressible Flow,* 2nd edn., Gordon and Breach, New York, NY (1969).

Larsen, V., Poulsen, L., Birgens, H., Dufva, M., and Kristensen, A., Pinched flow fractionation devices for detection of single nucleotide polymorphisms *Lab Chip* **8**, 818-821 (2008).

Liron, N. and Mochon, N., Stokes flow for a Stokes-let between 2 parallel flat plates *J. Eng. Math.* **10**, 287-303 (1976).

Loewenberg M. and Hinch, E. J., Numerical simulation of a concentrated emulsion in shear flow *J. Fluid Mech.* **321**,395-419 (1996).

Lorentz, H. A., A general theorem concerning the motion of a viscous fluid and a few consequences derived from it, *Zittingsverslag* Koninkl. Akad. van Wetensch. Amsterdam **5**, 168-175 (1896).

Lorentz, H. A., A general theorem concerning the motion of a viscous fluid and a few consequences derived from it *Zittingsverlag Konikl. Akad. Wet*[56] J.R. Blake, A note on the

image system for a Stokeslet in a no-slip boundary *Proc. Cambridge Philos. Soc.* **70**, 303-310 (1971).

Maenaka, H., Yamada, M., Yasuda, M., and Seki, M., Continuous and size-dependent sorting of emulsion droplets using microfluidic hydrodynamics in pinched microchannels, *Langmuir* **24**, 4405-4410 (2008).

Matsuda,M., Yamada, M. and Seki, M., Blood cell classification utilizing hydrodynamic filtration, , *Electron. Commun. Jpn.* **94**, 1-6 (2011).

Moffatt, H. K., Viscous and resistive eddies near a sharp corner, *J. Fluid Mech.* **18**, 1–18 (1964).

Moon, M., Kim, H., . Kwon, S., Lee, S., Chang, Y., and Lim, H., Pinched inlet split flow thin fractionation for continuous particle fractionation: Application to marine sediments for size-dependent analysis of PCDD/Fs and Metals, *Anal. Chem.* **76**, 3236-3243 (2004).

Nakashima, M., Yamada, M. and Seki, M., Pinched flow fractionation (PFF) for continuous particle separation in a microfluidic device 17th IEEE International Conference on Micro Electro Mechanical Systems, Maastricht, The Netherlands, 33-36 (2004).

Nilsson, A., Petersson, F., Jonsson, H., and Laurell, T., Acoustic control of suspended particles in micro fluidic chips, *Lab Chip* **4**, 131-135 (2004).

Nisisako, T., Torii, and Higuchi, T., Novel microreactors for functional polymer beads, *Chem. Eng. J.* **101**, 23-29 (2004).

O'Neill, M. E., A slow motion of viscous liquid caused by a slowly moving solid sphere: An addendum, *Mathematika* **14**, 170-172 (1967).

Ode, T., A new technique for optical 3D measurements with a confocal scanning laser microscope, *IEEE Instrumentation and Measurement Technology* **2**, 672-676 (1994).

Odqvist, F. K. G., Uber die randwertaufgaben der hydrodynamic zaher Flussigkeiten *Math. Z.* **32**, 329-375 (1930).
Paddock, S., Principles and practices of laser scanning confocal microscopy, *Mol. Biotech.* **16(2)**, 215-225 (2000).

Pan F. and Acrivos, A., Steady flows in rectangular cavities *J. Fluid Mech.* **28**, 643-655 (1967).

Patankar, N. A., Singh, P., Joseph, D. D., Glowinski, R. and Pan, T. W, A new formulation of the distributed Lagrange multiplier/fictitious domain method for particulate flows *Int. J. Multiphase Flow* **26**, 1509-1524 (2000).

Peskin, C. S., Numerical analysis of blood flow in the heart *J. Comput. Physics* **25**, 220-252 (1977).

Pinelli, A., Naqavi, I. Z., Piomelli, U. and Favier, J., Immersed-boundary methods for general finite-difference and finite-volume Navier-Stokes solvers *J. Comput. Physics* **229**, 9073-9091 (2010).

Power, H. and Miranda, G., Second kind integral equation formulation of Stokes flow past a particle of arbitrary shape *SIAM J. Appl. Maths* **47**, 689-698 (1987).

Power, H. and Wrobel, L. C., *Boundary Integral Methods in Fluid Mechanics.* Computational Mechanics Publications, Southampton-Boston (1995).

Pozrikidis, C., *Boundary Integral and Singularity Methods for Linearized Viscous Flow*, Cambridge University Press, Cambridge, MA (1992).

Rallison, J. M., A numerical study of the deformation and burst of a viscous drop in general shear flows *J. Fluid Mech.* **109**, 465-482 (1981).

Reddy, S. K., Cramer, N. B. and Bowman, C. N., Thiol-vinyl mechanisms II: kinetic modeling of ternary Thiol-Vinyl Photopolymerizations, *Macromolecules* **39**, 3681-3687 (2006).

Rigler, R., Fluorescence and single molecule analysis in cell biology, *Biochem. and Biophys. Res. Com.* **396**, 170-175 (2010).

Roberts, B. W. and Olbricht, W. L., Flow-induced particulate separations *AIChE J.* **49**, 2842-2849 (2003).

Roberts, B. W. and Olbricht, W. L., The distribution of freely suspended particles at microfluidic bifurcations *AIChE J.* **52**, 199-206 (2006).

Sai, Y., Yamada, M., Yasuda, M. and Seki, M., Continuous separations of particles using a microfluidic device equipped with flow rate control valves *J. Chromatography A* **1127**, 214-220 (2006).

Sanders, J. and Kandrot, E., *CUDA by example: An introduction to general-purpose GPU programming*, Addison-Wesley Professional, 1st ed., 2010.

Santiago, J., Werely, S., Meinhart, C. D., Beebe, D. and Adrian, R., A particle image velocimetry system for microfluidics, *Exp. In Fluids* **25**, 316-319 (1998).

Sharma, N., Chen, Y. and Patankar, N. A., A distributed Lagrange multiplier based computational method for the simulation of particulate-Stokes flow *Comput. Methods Appl. Mech. Engrg.* **194**, 4716-4730 (2005).

Staben, M. E., Zinchenko, A. Z. and Davis, R. H, Motion of a particle between two parallel walls in low-Reynolds-number Poiseuille flow *Phys. Fluids* **15**, 1711-1733 (2003).

Staben, M. E., Zinchenko, A. Z. and Davis, R. H., Erratum: Motion of particle between two parallel plane walls in low-Reynolds-number Poiseuille flow, *Phys. Fluids* **15**, 1711-1733 (2003). *Phys. Fluids* **16**, 4204-4206 (2004).

Staben, M. E., Zinchenko, A. Z. and Davis, R. H., Dynamic simulation of spheroid motion between two parallel plane walls in low-Reynolds-number Poiseuille flow *J. Fluid Mech.* **553**, 187-226 (2006).

Sugiura, S., Nakajima, M., Ito, H., and Seki, M., Synthesis of polymeric microspheres with narrow size distributions employing microchannel emulsification, *Macromol. Rapid Commun* **22**, 773-777 (2001).

Svanes, K. and Zweifach, B., Variations in small blood vessel hematocrits produced in hypothermic rats by micro-occlusion *Microvas. Res.* **1**, 210-220 (1968).

Takagi, J., Yamada, M., Yasuda, M., and Seki, M., Continuous particle separation in a microchannel having asymmetrically arranged multiple branches, *Lab Chip* **5**, 778-784 (2005).

Tsutsui, H., and Ho, C., Cell separation by non-inertial force fields in microfluidic systems, *Mechanics Research Communications* **36**, 92-103 (2009).

Wagner, G. J., Ghosal, S. and Liu, W. K., Particulate flow simulations using lubrication theory solution enrichment *Int. J. Numer. Meth. Engng.* **56**, 1261-1289 (2003).

Wagner, G. J., Moes, N., Liu, W. K. and Belytschko, T., The extended finite element method for rigid particles in Stokes flow *Int. J. Numer. Meth. Engng.* **51**, 293-313 (2001).
Weidtkamp-Peters, S., Weisshart, K., Schmiedeberg, L. and Hemmerich, P., Fluorescence correlation spectroscopy to assess the mobility of nuclear proteins, *Meth. In Mol. Biology* **464**, 321-341 (2008).

Whiteside, R. J., Noncontact optical profilometer, *App. Optics* **14**, 2480-2485 (1975).

Whitesides, G. R., Martyn, M. T., Coates, P. D., Micromoulding: process characteristics and product properties, *Plastics, Rubber and Composites* **32**, 231–239 (2003).

Whitesides, G. R. and Stroock, A., Flexible methods for microfluidics, *Physics Today* **54**, 42-48 (2001).

Xi, Y. and Whitesides, G. R., Soft lithography, *Ann. Rev. Mater. Sci.* **28,** 153 (1998).

Yamada, M., Kasim, V., Nakashima, M., Edahiro, J. and Seki, M., Continuous cell partitioning using an aqueous two-phase flow system in microfluidic devices, *Biotechnol. Bioeng.* **88**, 484-489 (2004).

Yamada, M., Nakashima, M. and Seki, M., Pinched flow fractionation: Continuous size separation of particles utilizing a laminar flow profile in a pinched microchannel *Anal. Chem.* **76**, 5465-5471 (2004).

Yamada, M., and Seki, M., Microfluidic particle sorter employing flow splitting and recombining, *Anal. Chem.* **78**, 1357-1362 (2006).

Zhang, X., Cooper, J., Monaghan, P. and Haswell, S., Continuous flow separation of particles within an asymmetric microfluidic device, *Lab Chip* **6,** 561–566 (2006).

Zinchenko, A. Z., Ashley, J. F. and Davis, R. H., A moving-frame, boundary-integral method for particle transport in microchannels of complex shape, *Phys Fluids* **24**, 043302 (2012).

Zinchenko, A. Z. and Davis, R. H., An efficient algorithm for hydrodynamical interaction of many deformable drops *J. Comp. Physics* **157**, 539-587 (2000).

Zinchenko, A. Z. and Davis, R. H., Shear flow of highly concentrated emulsions of deformable drops by numerical simulations *J. Fluid Mech.* **455**, 21-62 (2002).

Zinchenko, A. Z. and Davis, R. H., A boundary-integral study of a drop squeezing through interparticle constrictions *J. Fluid Mech.* **564**, 227-266 (2006).

Zinchenko, A. Z and Davis, R. H., Algorithm for direct numerical simulation of emulsion flow through a granular material *J. Comp. Physics* **227**, 7841-7888 (2008).

Zinchenko, A. Z., Rother, M. A. and Davis, R. H.., A novel boundary-integral algorithm for viscous interaction of deformable drops *Phys. Fluids* **9**, 1493-1511 (1997).